SYSTEM IDENTIFICATION AND CONTROL OF A FLEXIBLE MANIPULATOR

Xiaodong Sun ©

February 20, 2000

A THESIS SUBMITTED IN PARTIAL FULFILLMENT OF THE
REQUIREMENTS OF THE MScEng DEGREE
IN
CONTROL ENGINEERING
FACULTY OF ENGINEERING
LAKEHEAD UNIVERSITY
THUNDER BAY, ONTARIO

Abstract

The Observability Range Space Extraction (ORSE) algorithm is successfully applied to identify an initially overparameterized discrete-time state-space model for a single-link flexible manipulator. Several critical issues related to the experiments and the implementation of the ORSE algorithm are addressed.

A new model reduction and updating technique is proposed and applied to reduce the identified models. To quantify the contribution of individual modes to the responses, a new measure referred to as modal response magnitude (MRM) is developed and successfully applied to obtain a lower-order model by retaining the most significant modes. To correct errors caused by the model reduction, either the reduced input or output matrix is recalculated by a least squares solution.

Based on the updated reduced-order models, a controller named as PDPC is designed to ensure a good tracking accuracy and robustness to payload changes. The experimental results show that the PDPC control structure is effective in controlling rigid body motion to have a zero tracking error and the minimum vibration as well.

Acknowledgements

I gratefully dedicate this work to my supervisor Dr. K. Liu for his support and responsible supervision. This work would not have been possible without his erudite knowledge and extensive help. I would like to thank my Co-supervisor Dr. K. Natarajan for his valuable guidance and suggestions.

I also dedicate this work to my wife and parents for their love, patience, and support.

This work owes a lot to the efforts of many former researchers. Thanks are also due to my classmate, Miss B. McDonald and Mr. S. Feng for their discussion.

Table of Contents

List of Figures

List of Table

List of Acronyms

- BSG Base Strain Gauge
- DMV Data Matching Validation
- ITAE Integral of Time-multiplied Absolute-Error
- ILQR Integral plus Linear Quadratic Regulator
- MRM Modal Response Magnitude
- MRMC Modal Response Magnitude Combination
- MSG Middle Strain Gauge
- MSV Mode Singular Value
- ORSE Observability Range Space Extraction
- SFV Set-point Following Validation
- SVD Singular Value Decomposition

Chapter 1

Introduction

Traditionally, robotic manipulators have been designed and built in a manner that maximizes stiffness to minimize vibration and allow for good positional accuracy with relatively simple controllers. High stiffness is achieved by using rigid-links that limit the rapid motion of manipulators, increase the size of actuators, and boost energy consumption. Compared with traditional rigid-link manipulators, flexible-link manipulators have advantages such as faster response, lower energy consumption, smaller actuators, and lower transportation costs. But the price paid on those advantages is complication of the control problems, which focus primarily on controller design to compensate for flexure effects and to be robust in the presence of uncertainties such as payload change. The control difficulty is caused by the fact that since a flexible-link is a distributed system, a large number of flexible modes are required to accurately model its behavior. Further complications arise because of the nonlinear nature of the system.

The rest of this chapter is organized as follows: Section 1 presents an overview of the previous studies on flexible manipulators, section 2 discusses the identification methods, section 3 lists the objectives of the thesis research, and section 4 gives the outline of the thesis.

1.1 Overview of the Previous Studies on Flexible Manipulators

The studies on flexible manipulators can be classified into two areas: modeling and control. Efforts in the modeling area have been made primarily in two different directions. Analytical modeling tries to develop a mathematical model for a flexible manipulator using physical laws.

The studies in this direction are abound and too numerous to cite here. The report by Tarn, Bejczy, and Ding [1] serves as an excellent summary of existing works in modeling of flexible manipulators and contains probably the most comprehensive mathematical modeling formulation to date. To accurately model a flexible manipulator is difficult as there are many unknown factors such as damping and nonlinear effects. Another approach is to model a flexible manipulator by identification techniques. By treating the system under study as a black box, identification tries to fit input/output data to a chosen model. One of the main advantages in doing this way is that physical properties of the system components need not to know exactly. The work done by Tzes and Yurkovich [2] shows effective examples of applying those system identification methods.

Like modeling, extensive works on controller design for the flexible manipulators have been done by many researchers [3-10]. Controllers investigated in their works include the Proportional & Derivative (PD) Control, Linear Quadratic Regulator (LQR) control, Model Reference Adaptive Control (MRAC), Variable Structure Sliding Mode Control (VSSMC), and Linear Quadratic Gaussian (LQG) control. The results reveal that simpler controllers, like PD and LQR, have more promise than complicated controllers like VSSMC in the case of flexible-structure control.

Despite these numerous activities, it has been noted that little effort has been done to identify flexible-link manipulators using a discrete-time state-space model. Also, few reports have appeared on using a simple controller such as PID to achieve both a good tracking accuracy and robustness to changing payloads. These two topics have been identified to be the main motives for this study.

1.2 Review of Identification Methods

In order to design a high performance active control system, an accurate system model is a prerequisite. For the case of flexible manipulators, it is difficult to develop an accurate mathematical model for controller design; therefore, identification of flexible manipulators has been studied by many researchers. In [11], an AutoRegressive Moving Average (ARMA) model was used to model a single-link flexible manipulator. The recursive least squares (RLS)

algorithm was chosen as the identification method. On-line frequency domain information was used for the control of a flexible-link robot with varying payloads in [12]. The study reported in [13] identified an ARMA model for a two-link flexible manipulator for the purpose of on-line control. Time domain and frequency domain methods for modeling a single-link flexible manipulator were compared in [2]. A modal analysis was conducted for a two-link flexible manipulator in [14]. A state-space model of a flexible arm was first derived by the RLS estimation of an ARMA model and then a model reduction was conducted using the balanced realization in [15]. The study conducted in [16] first obtained the transfer functions of a single-link flexible manipulator using band-pass filters and then identified the parameters of the transfer functions by nonlinear curve fitting.

Due to the development of the computer industry and the high dimensional nature of the flexible manipulators, the discrete-time state-space models are more suitable for controller design and implementation. In past decade, several time domain identification methods for structural systems have been developed. These methods include the Eigensystem Realization Algorithm (ERA) [17], the Observer/Kalman Filter Identification (OKID) [18], Q-Markov Cover Algorithm [19], and the Observability Range Space Extraction (ORSE) [20]. If a pulse response is available, ERA can be directly applied to obtain the system parameter matrices. For general response data, OKID can be used and it consists of three main steps, i.e., computation of the observer Markov parameters, recovery of the system and observer gain Markov parameters, and realization of a state-space model. In [20], the concept of system identification by ORSE was developed by generalizing Q-Markov Cover and ERA. The ORSE algorithm can obtain a state-space model directly from general input/output data. The OKID and ORSE methods have been successfully applied in model identification for large flexible space structures [20-23].

A common feature of identification algorithms such as OKID or ORSE is that the model must be properly overparameterized in order to capture the dynamics of systems. This need arises due to the effects of irregularities such as measurement noise and nonlinearities of actual systems. An overparameterized model contains both system modes and computational modes. The order of the estimated model must be reduced to eliminate the computational modes and insignificant system modes. The reduced model must be updated to correct for errors caused

by truncation of some modes. A procedure for model reduction and updating proposed in [20] employs the balanced realization technique to produce a lower order model. A disadvantage of the model reduction through the balanced realization is that the model must be asymptotically stable or the eigenvalues of the transition matrix lie inside the unit circle. As the system under study involves rigid body motion and lightly damping modes, the identified model is likely to be unstable. Therefore, the balanced realization technique cannot be directly used. For model updating, the Least Squares (LS) model updating algorithm modifies iteratively the reduced model using the gradient information. The LS model updating technique assumes that the model to be updated is sufficiently accurate. In practice, this assumption is not always valid especially with a truncated model.

1.3 Objectives of the Thesis Research

1. The first objective of this study is to apply the ORSE algorithm to an electro-mechanical system that contains rigid modes and flexible modes. Specifically a single-link flexible manipulator is used as a test-bed for such systems.

2. The second objective of the study is to develop a new model reduction technique.

3. The third objective of the study is to develop a new model updating scheme that is more efficient than the LS model updating algorithm.

4. The fourth objective of the study is to design a simple controller that has both a good tracking accuracy and robustness with respect to payload change.

1.4 Outline of Thesis

The following chapters of this thesis are organized as follows. Chapter 2 presents system identification for a single-link flexible manipulator. This chapter includes the state-space model for the structural system, the ORSE algorithm, the experimental setup, and the system identification results for several types of experiments. Chapter 3 develops a new procedure for model reduction and updating. Several examples are presented. Chapter 4 gives the design

and tuning of the controller as well as real-time implementation of the controller. Chapter 5 concludes this thesis with a summary of the research and recommendations for future work.

Chapter 2

System Identification

The first objective of this thesis research is to model and identify a single-link flexible manipulator. A discrete-time state-space model is used to represent the system. The ORSE identification algorithm is chosen as a method to identify the discrete-time state-space model.

The rest of this chapter is organized as follows: Section 2 discusses the state-space model for structural systems. Section 3 presents the ORSE identification algorithm briefly. Section 4 describes the experimental hardware setup. Section 5 presents the identification results for three types of experiments. Section 6 contains a brief conclusion.

2.1 The State-Space Model of Structural Systems

For a linear time-invariant structural system, its dynamics can be described by the following continuous state-space equation

$$\begin{cases} \dot{x}(t) = A_c x(t) + B_c u(t) \\ y(t) = C_c x(t) + D_c u(t) \end{cases} \tag{2-1}$$

where $x \in R^{n\times 1}$ is a vector of the state variables, $u \in R^{r\times 1}$ is an input vector, $y \in R^{m\times 1}$ is a vector of the system outputs, $A_c \in R^{n\times n}, B_c \in R^{n\times r}, C_c \in R^{m\times n}$, and $D_c \in R^{m\times r}$ are the parameter matrices, r is the number of inputs, n is the number of the state variables or the model order, m is the number of outputs. The notation $R^{i\times j}$ denotes $i \times j$ real matrix spaces.

For systems controlled by digital computers, the measurement data is collected at discrete

times. Assume that the interval between two sampling points is Δt and that the excitation signal $u(t)$ is generated from a discrete signal by zero-order hold between the two sampling points. Define :

$$A \triangleq e^{A_c \Delta t}, \quad B \triangleq \int_0^{\Delta t} e^{A_c \tau} B_c d\tau, \quad C \triangleq C_c, \quad D \triangleq D_c,$$
$$x(k) \triangleq x(k\Delta t), \quad u(k) \triangleq u(k\Delta t), \quad y(k) \triangleq y(k\Delta t). \tag{2-2}$$

Then the following is a discrete-time state-space model for structural systems,

$$\begin{cases} x(k+1) = Ax(k) + Bu(k) \\ y(k) = Cx(k) + Du(k) \end{cases} \tag{2-3}$$

The above equation is a centralized model for a structural system and describes all the input and output relationships of the system. The frequency responses of the structural system can be computed by

$$G(J\omega) = C(e^{-J\omega\Delta t} I - A)^{-1} B + D \tag{2-4}$$

where $J = \sqrt{-1}$ and the ω parameter is the frequency variable.

It is assumed that the state-space model of equation (2-3) is controllable and observable. This is a valid assumption because any uncontrollable or unobservable part of the state-space model is irrelevant to input-output modeling and to active control of the system. Hence, any uncontrollable or unobservable part of the system can be ignored in its input-output modeling. The controllable and observable state-space model of a system is not unique, and any coordinate transformation with a nonsingular matrix T will result in another state-space realization $\left[\bar{A} = TAT^{-1}, \quad \bar{B} = TB, \quad \bar{C} = CT^{-1}, \quad \bar{D} = D \right]$ of the same system.

Assume that the output $y(k)$ is contaminated by unknown measurement noise $n(k)$ giving the actual measurement $\tilde{y}(k)$

$$\tilde{y}(k) = y(k) + n(k). \tag{2-5}$$

Suppose that the following data samples are available from experiments

$$\tilde{y}(k) \text{ and } u(k) \text{ for } k = 1, 2, ..., K, \tag{2-6}$$

where $u(k)$ is an arbitrary input excitation signal, $\tilde{y}(k)$ is output measurement defined in equation (2-5), and K is the length of experimental data records. The technique of the system identification is to identify the matrices $\left[\bar{A}, \ \bar{B}, \ \bar{C}, \ \bar{D} \right]$ of a state-space model and its dimension n from above input and output data samples $u(k)$ and $\tilde{y}(k)$.

2.2 System Identification by the ORSE Algorithm

In this section, the ORSE identification algorithm developed in [20] is briefly presented to provide a background for the following experimental study and the development of a model reduction and updating technique in chapter 3. First, the principle for the estimation of the system matrices of a state-space model from the base vectors of its Observability Range Space is discussed. Then, the extraction of the base vectors from experimental data and the procedure of the identification algorithm are presented.

2.2.1 Observability Range Space and System Matrices Estimation

Let $\mathbf{O}_q$ denote the observability matrix of block dimension q of the state-space model in equation (2-3), i.e.,

$$\mathbf{O}_q = \begin{bmatrix} C \\ CA \\ \vdots \\ CA^{q-1} \end{bmatrix} \in R^{qm \times n}. \tag{2-7}$$

One property of the observability matrix important to the identification technique is its block shift structure. Let $\mathbf{O}_1$ be the first subblock of $\mathbf{O}_q$, $\mathbf{O}_{q-1}$ to be the first $q-1$ subblocks of $\mathbf{O}_q$, and $\bar{\mathbf{O}}_{q-1}$ to be the last $q-1$ subblocks. Thus,

$$\mathbf{O}_{q-1} = \begin{bmatrix} C \\ CA \\ \vdots \\ CA^{q-2} \end{bmatrix}, \qquad \bar{\mathbf{O}}_{q-1} = \begin{bmatrix} CA \\ CA^2 \\ \vdots \\ CA^{q-1} \end{bmatrix}, \tag{2-8}$$

and,

$$\mathbf{O}_1 = C, \qquad \bar{\mathbf{O}}_{q-1} = \mathbf{O}_{q-1}A\ . \tag{2-9}$$

When $q > n$, $\mathbf{O}_{q-1}$ will be full column rank and

$$A = \mathbf{O}_{q-1}^{+}\bar{\mathbf{O}}_{q-1}, \qquad C = \mathbf{O}_1, \tag{2-10}$$

where the superscript + denotes the Moore-Penrose pseudo inverse.

Let Range($\cdot$) denote the range space of a matrix. The *Observability Range Space* of order q of a state-space model in equation (2-3) is defined as the range space of matrix $\mathbf{O}_q$, i.e. Range($\mathbf{O}_q$). Equation (2-10) becomes very useful if a matrix Ψ_q which has the same range space as Range($\mathbf{O}_q$) can be obtained from experimental data. Such a matrix Ψ_q can then be written as $\Psi_q = \mathbf{O}_q T^{-1}$ for some nonsingular matrix T and can be considered as an observability matrix of model (2-3) in a particular realization coordinate. Applying equation (2-10) to the matrix Ψ_q gives an estimation of the A and C matrices since the realization coordinate is irrelevant to input-output modeling of the system. This is the key for the ORSE identification algorithm.

If the A and C matrices are known or are correctly estimated by applying equation (2-10), $y(k)$ becomes a linear function of the elements of matrices B and D. The following presents this linear function and a linear least squares solution of these elements when $y(k)$, $u(k)$, A, and C are given.

Assume that the input vector $u(k)$ can be written as

$$u(k) = \begin{bmatrix} u_1(k), & u_2(k), & , & u_r(k) \end{bmatrix}^T, \tag{2-11}$$

where $u_j(k)$ for $j = 1, 2, ..., r$ is a scalar signal at the $j-$th input channel. Let b_{ij} and d_{ij} be the $ij-$th elements of the matrices B and D, respectively. Thus,

$$\begin{aligned} B &= [b_{ij}] = \left[\begin{array}{cccc} B_1, & B_2, & & B_r \end{array} \right], \\ D &= [d_{ij}] = \left[\begin{array}{cccc} D_1, & D_2, & , & D_r \end{array} \right], \end{aligned} \tag{2-12}$$

where B_j and D_j for $j = 1, 2, ..., r$ are the $j-$th column vectors of matrices B and D, respectively. Then, the state-space model of equation (2-3) can be rewritten as

$$\begin{aligned} x(k+1) &= Ax(k) + \sum_{j=1}^{r} I_n u_j(k) B_j \\ &= Ax(k) + \sum_{i=1}^{m} \sum_{j=1}^{r} I_{ni} u_j(k) b_{ij} \\ y(k) &= Cx(k) + \sum_{j=1}^{r} I_m u_j(k) D_j \\ &= Cx(k) + \sum_{i=1}^{m} \sum_{j=1}^{r} I_{mi} u_j(k) d_{ij} \end{aligned} \tag{2-13}$$

where I_n and I_m are identity matrices of dimensions $n \times n$ and $m \times m$, and I_{ni} and I_{mi} are the $i-$th column vectors of I_n and I_m, respectively. Define $y_{d_{ij}}(k)$ and $y_{b_{ij}}(k)$ as

$$\left\{ \begin{array}{l} x_{ij}(k+1) = Ax_{ij}(k) + I_{ni} u_j(k) \\ y_{b_{ij}}(k) = Cx_{ij}(k) \\ y_{d_{ij}}(k) = I_{mi} u_j(k). \end{array} \right. \tag{2-14}$$

Then, $y_{d_{ij}}(k)$ and $y_{b_{ij}}(k)$ can be computed from A, C, and $u_j(k)$ from equation (2-14), the following linear relationship between $y(k)$ and the elements of B and D exists,

$$y(k) = \sum_{i=1}^{m} \sum_{j=1}^{r} y_{d_{ij}}(k) d_{ij} + \sum_{i=1}^{n} \sum_{j=1}^{r} y_{b_{ij}}(k) b_{ij} = \Phi(k)\Theta \tag{2-15}$$

where matrices $\Phi(k) \in R^{m\times(m\times r+n\times r)}$ and $\Theta \in R^{(m\times r+n\times r)\times 1}$ are defined as

$$\begin{aligned}\Phi(k) = [\ & y_{d_{11}}(k),\cdots,y_{d_{m1}}(k)\ ; && y_{d_{1r}}(k),\cdots,y_{d_{mr}}(k);\\ & y_{b_{11}}(k),\cdots,y_{b_{m1}}(k)\ ; && ;\ y_{b_{1r}}(k),\cdots,y_{b_{mr}}(k)\ ],\end{aligned} \tag{2-16}$$

$$\Theta = \left[\ D_1^T,\quad ,\ D_r^T,\ B_1^T,\quad ,\ B_r^T\ \right]^T$$

The linear least squares solution for the elements of the B and D matrices is

$$\bar{\Theta} = \left[\sum_{k=1}^{K}\Phi(k)^T\Phi(k)\right]^+\left[\sum_{k=1}^{K}\Phi(k)^T y(k)\right]. \tag{2-17}$$

2.2.2 Observability Range Space Extraction

The following section decribes the method to extract the observability range space and its base vector matrix from experimental data.

Define the following extended measurement vector $\tilde{y}_q(k) \in R^{qm\times 1}$, and extended input vector $u_q(k) \in R^{qr\times 1}$

$$\tilde{y}_q(k) = \begin{bmatrix}\tilde{y}(k)\\ \tilde{y}(k+1)\\ \vdots\\ \tilde{y}(k+q-1)\end{bmatrix},\quad u_q(k) = \begin{bmatrix}u(k)\\ u(k+1)\\ \vdots\\ u(k+q-1)\end{bmatrix} \tag{2-18}$$

where the q parameter is the block dimension of these extended vectors.

Construct two Hankel matrices $\mathbf{Y} \in R^{qm\times d}$ and $\mathbf{U} \in R^{qr\times d}$ using the experimental data $\tilde{y}(k)$ and $u(k)$

$$\mathbf{Y} = \left[\tilde{y}_q(1), \quad \tilde{y}_q(2), \quad , \quad \tilde{y}_q(d) \right]$$

$$= \begin{bmatrix} \tilde{y}(1) & \tilde{y}(2) & & \tilde{y}(d) \\ \tilde{y}(2) & \tilde{y}(3) & & \tilde{y}(d+1) \\ \vdots & \cdot & & \cdot \\ \tilde{y}(q) & \tilde{y}(q+1) & & \tilde{y}(K) \end{bmatrix}$$

$$\mathbf{U} = \left[u_q(1), \quad u_q(2), \quad , \quad u_q(d) \right] \tag{2-19}$$

$$= \begin{bmatrix} u(1) & u(2) & & u(d) \\ u(2) & u(3) & & u(d+1) \\ \vdots & \cdot & & \cdot \\ u(q) & u(q+1) & & u(K) \end{bmatrix}$$

where $d = K - q + 1$ is the column dimension of the Hankel matrices and q is the block row dimension.

For the case when output measurements are free of noise, it can be proved that

$$\text{Range}\left[\mathbf{Y}\mathbf{Y}^T - \mathbf{Y}\mathbf{U}^T(\mathbf{U}\mathbf{U}^T)^+(\mathbf{Y}\mathbf{U}^T)^T\right] = \text{Range}(\mathbf{O}_q) \ . \tag{2-20}$$

The above equality shows that the system observability range space can be obtained from the Hankel matrices $\mathbf{Y}$ and $\mathbf{U}$ constructed from experimental data.

In practice, however, output measurements will always be contaminated by the measurement noise. As a result, the $\text{Range}\left[\mathbf{Y}\mathbf{Y}^T - \mathbf{Y}\mathbf{U}^T(\mathbf{U}\mathbf{U}^T)^+(\mathbf{Y}\mathbf{U}^T)^T\right]$ does not exactly equal to the $\text{Range}(\mathbf{O}_q)$. To estimate base vectors of the $\text{Range}(\mathbf{O}_q)$, apply the Singular Value Decomposition (SVD) to $\mathbf{Y}\mathbf{Y}^T - \mathbf{Y}\mathbf{U}^T(\mathbf{U}\mathbf{U}^T)^+(\mathbf{Y}\mathbf{U}^T)^T$, i.e.,

$$\mathbf{Y}\mathbf{Y}^T - \mathbf{Y}\mathbf{U}^T(\mathbf{U}\mathbf{U}^T)^+(\mathbf{Y}\mathbf{U}^T)^T$$
$$= \left[\bar{U}_{\psi 1} \quad \bar{U}_{\psi 2} \right] \begin{bmatrix} \bar{\Sigma}_{\psi 1} & 0 \\ 0 & \bar{\Sigma}_{\psi 2} \end{bmatrix} \left[\bar{U}_{\psi 1} \quad \bar{U}_{\psi 2} \right]^T \tag{2-21}$$

where $\bar{U}_{\psi 1} \in R^{qm \times n}$ and $\bar{U}_{\psi 2} \in R^{qm \times (qm-n)}$ are column unitary matrices, $\bar{\Sigma}_{\psi 1}$ =diag$[\bar{\sigma}_i] \in R^{n \times n}$ is a diagonal matrix of singular values $\bar{\sigma}_i$, for $i = 1, 2, ..., n$, $\bar{\Sigma}_{\psi 2}$ =diag$[\bar{\sigma}_{n+i}] \in R^{(qm-n) \times (qm-n)}$ is a diagonal matrix of singular values $\bar{\sigma}_{n+i}$, for $i = 1, 2, ..., qm - n$. The n parameter is the estimate of the system order determined by the following criterion,

$$\begin{aligned} &\bar{\sigma}_i > \bar{\sigma}, \quad i = 1, 2, ..., n \\ &\bar{\sigma}_{n+i} < \bar{\sigma} \quad i = 1, 2, ..., qm - n \end{aligned} \tag{2-22}$$

where $\bar{\sigma}$ is a prespecified threshold for zero. Hence, the base vector matrix Ψ_q can be estimated as

$$\Psi_q = \mathbf{O}_q T^{-1} = \bar{U}_{\psi 1} = \begin{bmatrix} \bar{C} \\ \bar{C}\bar{A} \\ \vdots \\ \bar{C}\bar{A}^{q-1} \end{bmatrix} \in R^{qm \times n}. \tag{2-23}$$

2.2.3 The Computation Procedure of the ORSE Identification Algorithm

Step 1. Form the Hankel matrices from the experimental data as shown in the equation (2-19).

Step 2. Apply the SVD to the matrix $\mathbf{Y}\mathbf{Y}^T - \mathbf{Y}\mathbf{U}^T(\mathbf{U}\mathbf{U}^T)^+(\mathbf{Y}\mathbf{U}^T)^T$, obtain an estimate of the system order n by comparing the singular values to a prespecified threshold $\bar{\sigma}$. Construct the base vector matrix Ψ_q as shown in the equation (2-21) and (2-23).

Step 3. Partition Ψ_q and define Ψ_{q-1} and $\overline{\Psi}_{q-1}$ matrices as follow:

$$\Psi_q = \begin{bmatrix} \psi_0 \\ \psi_1 \\ . \\ \psi_{q-1} \end{bmatrix}, \quad \Psi_{q-1} = \begin{bmatrix} \psi_0 \\ \psi_1 \\ . \\ \psi_{q-2} \end{bmatrix}, \quad \overline{\Psi}_{q-1} = \begin{bmatrix} \psi_1 \\ \psi_2 \\ . \\ \psi_{q-1} \end{bmatrix},$$

$\psi_i \in R^{m \times n}$, $i = 0, ..., q - 1$.

Step 4. Compute the $\bar{A}$ and $\bar{C}$ matrices as

$$\bar{A} = \Psi_{q-1}^{+}\,\overline{\Psi}_{q-1}, \qquad \bar{C} = \psi_0.$$

Step 5. Compute the $\bar{B}$ and $\bar{D}$ matrices using the equations (2-14) to (2-17).

2.3 The Experimental Setup

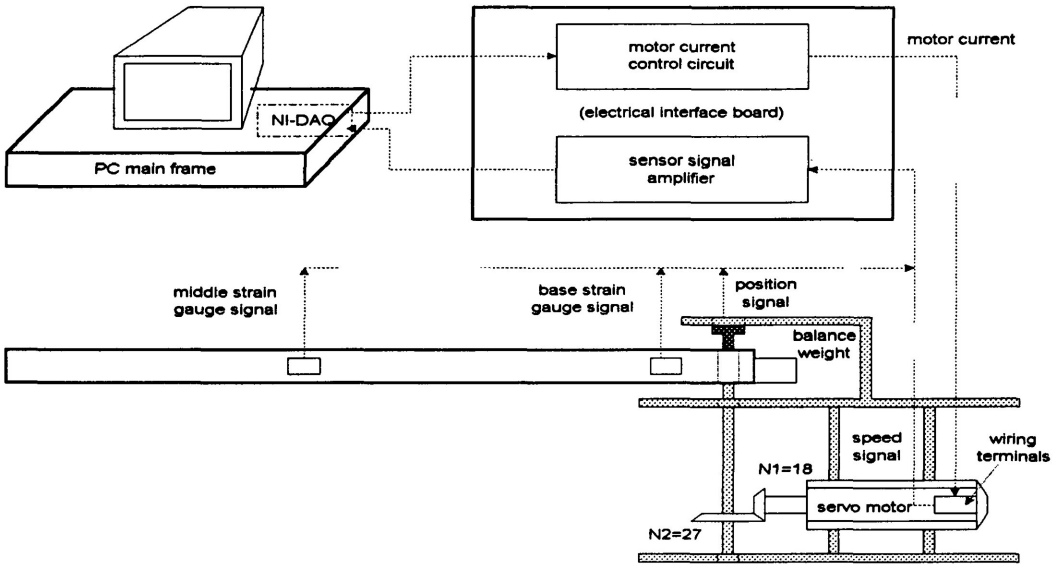

Figure 2-1. The experimental apparatus setup.

The experimental apparatus setup for a single-link flexible manipulator is shown in Figure 2-1. The detailed electrical schematic diagrams can be found in [24]. The single-link flexible manipulator is modeled as a cantilever beam clamped at the rotational axis of the shaft driven by a DC motor. The link moves in a horizontal plane in order to reduce the effect of gravity.

The beam is constructed from 6061-T6 aluminum-magnesium-silicon alloy. The dimension of the beam is 1 m (length) $\times$ 51 mm (width) $\times$ 3 mm (thickness). The flexibility of this manipulator is greater than that of current industrial robots.

The DC motor, manufactured by Small Electric Motor Ltd., used in this experimental setup is a permanent magnet motor with a rated stall torque of 2.938 N-m. The motor current served as a system input controlled by the computer through the NI-DAQ(National Instruments-Data Acquisition) board and the related electrical circuits. The magnitude and direction of

the motor current are separately implemented through the electrical circuits with two voltage commands from the two analog output channels (DAC0 and DAC1) of the NI-DAQ board. The voltage signal from the channel DAC1 of the NI-DAQ board is used for the direction control (0v for clockwise rotation, 5v for counter clockwise rotation viewed from the top of the arm). Channel DAC0 is used for magnitude control that has a range of 0v to 10v and a proportional gain of approximate 0.5 A/V to motor current as shown in Figure 2-2 below.

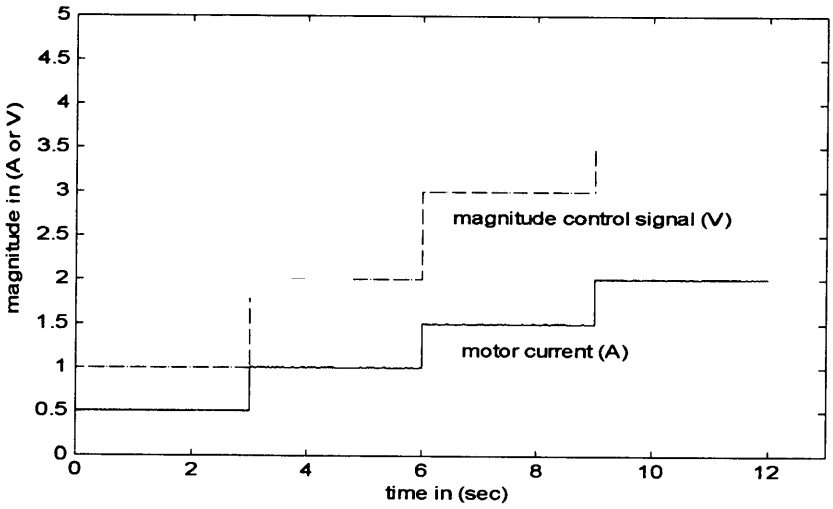

Figure 2-2. The characteristics of motor current vs magnitude control signal.

Clearly, the characteristic between the output of the magnitude control from computer and the actual motor current magnitude is linear.

Four sensors are used to measure the system responses. They are an angular position potentiometer, a tachometer and two strain gauges separately located in the middle and base of the arm. The locations of the strain gauges are chosen to ensure that the deflection of the arm can be sensed. The signals from these four sensors are acquired and processed by a personal computer through the NI-DAQ board. Two sampling rates (300 Hz and 500 Hz) were used to compare the effect of sampling rate on the accuracy of the identified models.

The personal computer used for control is a Pentium Pro(r) with 32MB RAM. The NI-DAQ board is a National Instruments PCI Series model PCI-MIO-16E-4, which has a resolution of 12 bit, 16 single-end analog input channels with maximum sampling rate of 500 kS/s, and 2

D/A output channels with maximum update rate of 1 MS/s. The application software used for data acquisition and system control is LabWindows/CVI.

The apparatus is, therefore, a system of single input and four outputs, i.e., $r = 1$ and $m = 4$. The direct transmission matrix is zero, i.e., $\bar{D} = \begin{bmatrix} 0 & 0 & 0 & 0 \end{bmatrix}^T$ because the outputs are not directly related to the input. The system identification intends to identify $\bar{A}, \bar{B}$, and $\bar{C}$ using experimental data of $u(k)$ and $\tilde{y}(k)$, for $k = 1, 2, ..., K$.

2.4 Experimental Results

Three types of experiments for system identification have been carried out. They are open-loop experiments, bounded position experiments (to be defined in section 2.4.2), and closed-loop experiments.

The accuracy of an identified model is evaluated using the root-mean-square of the prediction error, i.e.,

$$RMS_i = \sqrt{\frac{\sum_{k=1}^{K} [\tilde{y}_i(k) - \hat{y}_i(k)]^2}{K}} \tag{2-24}$$

where $\hat{y}_i(k)$ for $k = 1, 2, ..., K$ denotes the simulation output. A nondimensionalized measurement of the model accuracy then is defined as

$$\delta_i = \frac{RMS_i}{\sqrt{\sum_{k=1}^{K} \tilde{y}_i^2(k)/K}}$$

$$\bar{\delta} = \frac{\sum_{i=1}^{m} \delta_i}{m} \tag{2-25}$$

where $\delta_1, \delta_2, \delta_3$ and δ_4 denote the errors for the angular position, base strain gauge (BSG), middle strain gauge(MSG), and angular speed, respectively. The $\bar{\delta}$ parameter is an indicator of the overall model accuracy .

For the purpose of the comparison, the eigenvalues of the state matrix $\bar{A}$ are evaluated,

$$\bar{A} = \Psi \Lambda \Psi^{-1} \tag{2-26}$$

where

$$\Lambda = \begin{bmatrix} \lambda_1 & 0 & 0 & 0 & 0 & 0 & 0 & 0 \\ 0 & \lambda_2 & 0 & 0 & 0 & 0 & 0 & 0 \\ 0 & 0 & & 0 & 0 & 0 & 0 & 0 \\ 0 & 0 & 0 & \lambda_{n_1-1} & 0 & 0 & 0 & 0 \\ 0 & 0 & 0 & 0 & \lambda_{n_1} & 0 & 0 & 0 \\ 0 & 0 & 0 & 0 & 0 & \lambda_{n_1+1} & 0 & 0 \\ 0 & 0 & 0 & 0 & 0 & 0 & & 0 \\ 0 & 0 & 0 & 0 & 0 & 0 & 0 & \lambda_n \end{bmatrix} \tag{2-27}$$

$$T = \begin{bmatrix} \Psi_1 & \Psi_2 & & \Psi_{n_1-1} & \Psi_{n_1} & \Psi_{n_1+1} & & \Psi_n \end{bmatrix}$$

where $\lambda_{i+1} = \lambda_i^*$ and $\Psi_{i+1} = \Psi_i^*$ for $i = 1, 3, ..., n_1 - 1$ are the pairs of complex eigenvalues and eigenvectors, respectively, λ_i and Ψ_i for $i = n_1 + 1, \cdots, n$ are real eigenvalues and eigenvectors, respectively. As shown in equation (2-27), the eigenvalues and eigenvectors are arranged in such a way that the complex pairs are grouped together.

The natural frequency and damping ratio corresponding to a pair of complex conjugate modes are related to the eigenvalues by

$$\lambda_i = e^{(-\omega_i \varsigma_i + J\omega_i \sqrt{1-\varsigma^2})\Delta t} \tag{2-28}$$

where the ω_i parameter is the $i-$th natural frequency, and the ς_i parameter is the $i-$th damping ratio.

The validation of an identified model is done in two ways. They are Data Matching Validation (DMV) and Set-point Following Validation (SFV) defined as following:

1. DMV: Comparison of the simulation outputs and measurements outputs. The input data used for the simulation is the same as those used for the model identification but

twice longer, i.e., only half of the data is used in the identification.

2. SFV: Comparison of the simulation outputs and measurements outputs under the same Proportional + Derivative (PD) controller setting ($k_p = 0.5$, and $k_d = 1.4$) and position reference. The schematic diagram of the simulation is shown in Figure 2-3.

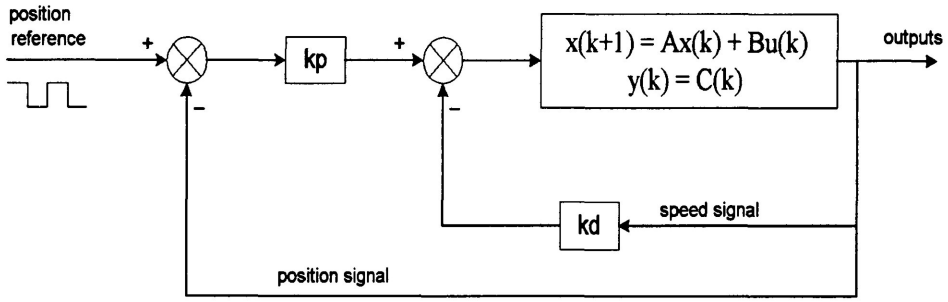

Figure 2-3. The schematic diagram for simulation of identified models (SFV).

The conventions used in the simulation plots are:

1. For the DMV and SFV plots, the dotted line denotes the simulation output and solid line denotes the measured output. The subplot (a), (b), (c), and (d) are the position signal, base strain gauge signal, middle strain gauge signal, and speed signal, respectively.

2. For the plots of the frequency responses, the dash-dotted line, the solid line, the dashed line, and the dotted line represent the position signal, base strain gauge signal, middle strain gauge signal, and speed signal, respectively.

2.4.1 Open-loop Experiments

The system setup for open-loop experiments is shown in Figure 2-4. The preset system exciting input signal, which is proportional to the motor current, was generated by a computer and sent out through two analog output channels (channels DAC 1 and DAC 0) of the NI-DAQ board to the system. The equivalent data acquisition point for input $u(k)$ in Figure 2-4 (same as in Figures 2-9 and 2-13) means the input signal (motor current) used in the identification is generated from computer's analog output signals based on the linear characteristics shown

in Figure 2-2 to avoid the noise. The response signals from four sensors were simultaneously collected through the analog input channels (channels ACH 0, ACH 1, ACH 2, ACH 3).

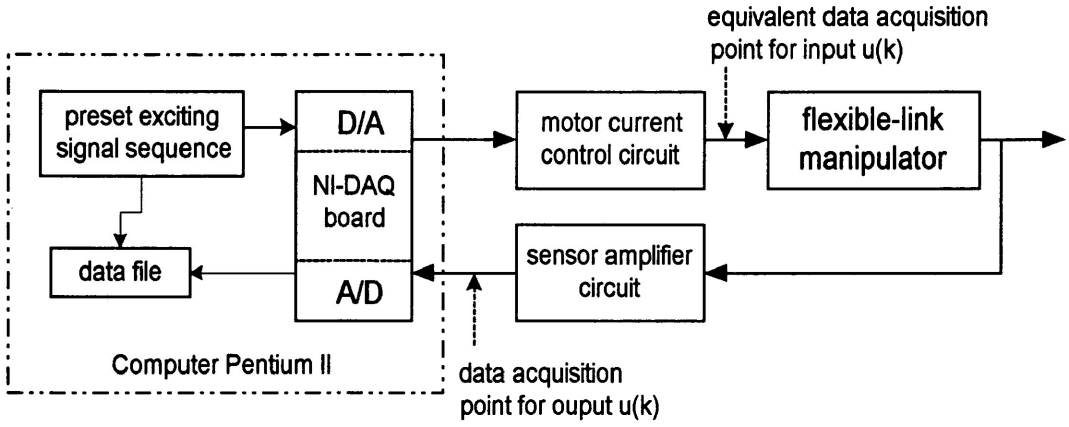

Figure 2-4. The open-loop experimental setup.

During the open-loop experiments, four types of excitation signals were used. They are :

1. Square waveform : The magnitude of the motor current is constant, and the direction of the motor current is alternated periodically at a frequency of 0.5 Hz. A sample waveform is shown in Figure 2-5a.

2. Periodic random waveform : The magnitude of the motor current is random, and the direction of the motor current is alternated periodically at a frequency of 0.5 Hz. A sample periodic random waveform is shown in Figure 2-5b.

3. Varying square waveform : The magnitude of the motor current is constant, and the direction of motor current is alternated at a frequencies from 0.6 Hz to 3 Hz. A sample varying square waveform is shown in Figure 2-5c.

4. Random waveform : Both the magnitude and direction of the motor current are random. A sample random waveform is shown in Figure 2-5d.

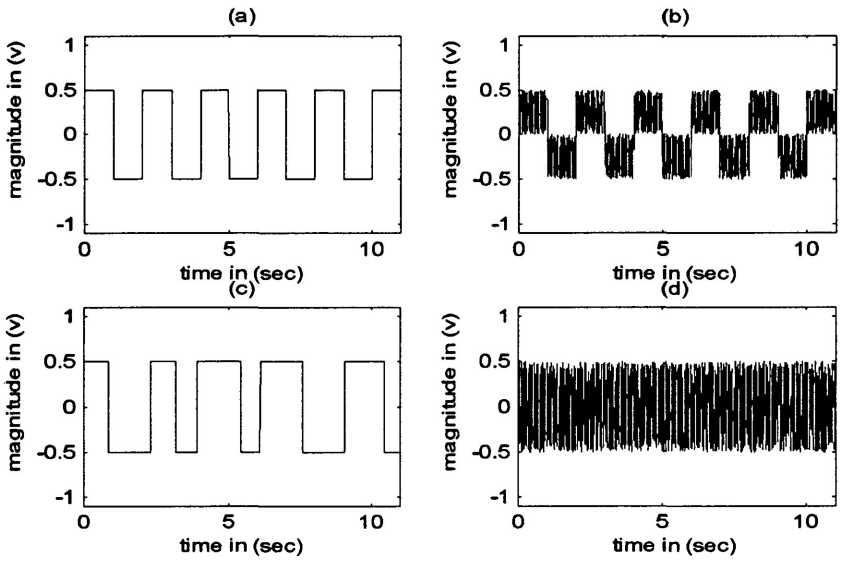

Figure 2-5. The exciting signals for the open-loop experiments.

Numerous data for each type of the exciting signals were collected and applied for identifying the system. Based on the identification results, the following observations can be obtained.

1. As shown in Table 2-1, the data from the square waveform exciting signal gave the best identification results, and the data from the random exciting signal gave the worst.

2. The order of the identified model is estimated from the plot of the singular values of the matrix $\mathbf{Y}\mathbf{Y}^T - \mathbf{Y}\mathbf{U}^T(\mathbf{U}\mathbf{U}^T)^+(\mathbf{Y}\mathbf{U}^T)^T$. Figure 2-6 is an example plot of the singular values. The order of the identified model can be chosen as $n = 15$ because all the rest of the singular values are sufficiently small. There is a problem that the order of the identified model estimated by this way may result in an unstable model. If a stable order is required, the order has to be re-estimated until a stable model can be obtained. Table 2-1 lists model orders that correspond to the stable models.

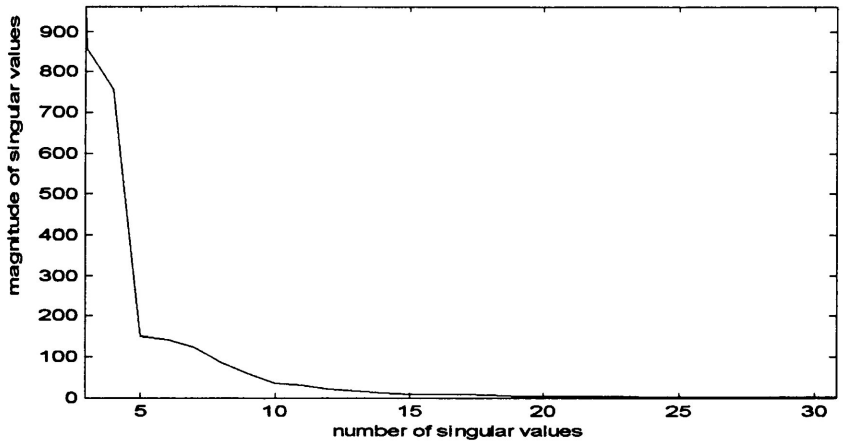

Figure 2-6. A sample plot of the Singular Values

Table 2-1. The identification results for the open-loop experiments							
data code	stable system orders	minimum DMV error					
		n_x	δ_1	δ_2	δ_3	δ_4	$\bar{\delta}$
O_dat1	8,11,14,30,33~36	36	0.1598	0.1578	0.3091	0.2397	0.2166
O_dat2	19,21	19	0.0484	0.1476	0.3125	0.1449	0.1634
O_dat3	8,14,18,20,21	18	0.3652	0.1670	0.3214	0.1772	0.2577
O_dat4	8,10,12,14	8	0.0773	0.2947	0.4943	0.3257	0.2980
O_dat5	12	12	0.1566	0.3128	0.4417	0.7996	0.4254
O_dat6	7,8,10,12,24,27,28,31~35	28	0.3370	0.2608	0.5030	0.3381	0.3597
O_dat7	no stable model	31	0.2505	0.2584	0.3723	0.6522	0.3834
O_dat8	8,10,12~14,16,18~20,26~30	27	0.1683	0.2397	0.5163	0.3431	0.3169
O_dat9	8,12,14,18,20,22,24~29	24	0.3590	0.2139	0.3797	0.3207	0.3183
O_dat10	12	12	0.1155	0.2676	0.5897	0.2554	0.3070
O_dat11	8,11,12,15~21,24~26,28,29	26	0.7778	0.2864	0.4596	0.4127	0.4841
O_dat12	8,10~12,16	11	0.5566	0.2021	0.4465	0.3075	0.3782
O_dat13	no stable model	33	0.9137	0.6792	0.5809	0.5006	0.6686
O_dat14	no stable model	31	0.7304	0.7129	0.8099	0.4872	0.6851
Notes: The detail information about the data code refer to Table A-1 in Appendix A. The critical stable model included							

3. For a stable identified model, the result of the DMV is acceptable as shown in Figure 2-7. It is seen that the simulated outputs agree well with both the data used in the identification ($k = 1$ to 3000 or $t \leq 10$ seconds) and the data not used in the identification ($k = 3001$ to 6000 or $t > 10$ seconds). On the other hand, in the case of the SFV as shown in Figure

2-8, the simulated responses do not agree well with the measured ones, especially for the angular position signal.

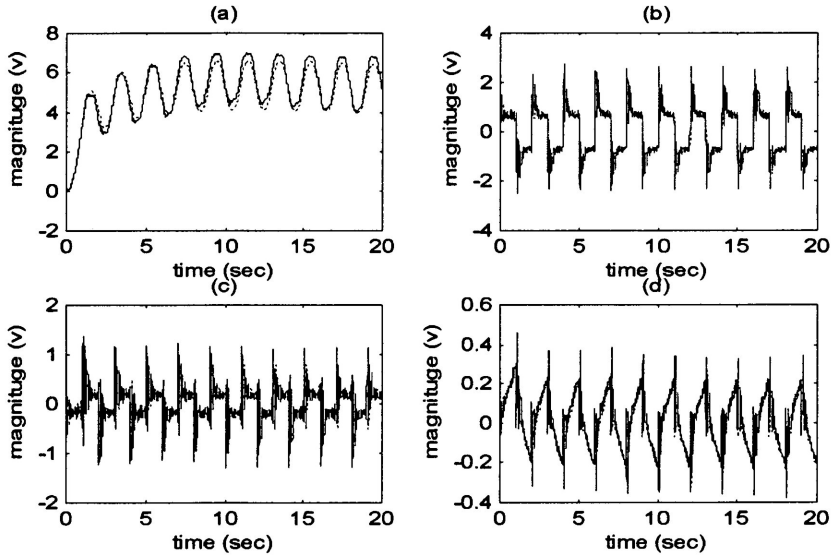

Figure 2-7. The DMV results for an identified model (Ao2_19) derived from the open-loop experiments.

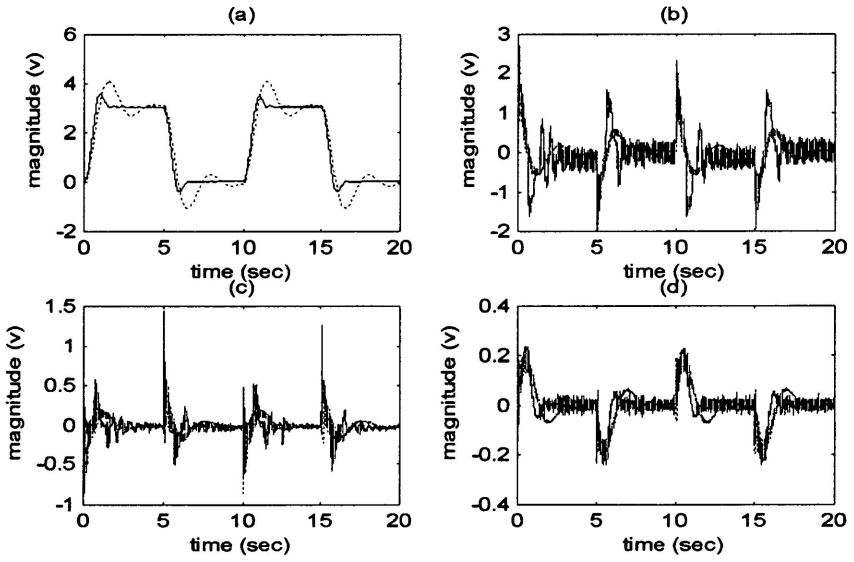

Figure 2-8. The SFV results for an identified model (Ao2_19) derived from the open-loop experimental data.

4. The first three structural modes of the system were analytically found to be 9 Hz, 25 Hz, and 48 Hz. For this specific system, experimental results show that the first three structural modes of the system can be successfully excited by each type of the exciting signals. Table 2-2 records the sample results of the natural frequencies calculated from identified models for four types of exciting signals with the same estimated system order. Clearly, each identified model can capture the first three structural modes, but there exist some computational modes.

Table 2-2. Sample results of the natural frequency calculations

model notes	the type of exciting signal waveform			
	square	periodic random	varying square	random
The order of selected models for each type of exciting signal waveform is 27. The unit for natural frequencies is in Hz.	46.3594	46.2436	47.2968	57.9282
	25.8423	36.4244	24.8077	52.0578
	23.4900	29.7634	22.7656	44.4208
	20.8455	23.6888	21.1291	31.5864
	19.8929	23.3733	17.7503	26.4798
	16.9240	20.3450	16.0718	21.7281
	15.4588	17.4293	10.1449	18.1470
	10.2807	14.8306	8.9644	16.9150
	8.6456	10.1949	8.6183	12.2895
	7.7545	8.6636	8.4795	11.6205
	5.0598	6.7934	6.8815	9.9277
	2.1794	0.1338	1.6436	4.2165
				0.8210

One of the problems with the open-loop experiments is that it is difficult to maintain the range of the arm rotation. Physically the arm is restricted to rotate within $\pm 80°$. When the angular position reaches this limit, the experiment has to be stopped. To cope with this problem, the bounded position experiment was devised.

2.4.2 Bounded Position Experiments

The system setup for the bounded position experiments is shown in Figure 2-9. The current direction is controlled by comparing the measured angular position signal with the preset position bounds. When the angular position reaches the preset position bounds, the current direction is changed. The position bounds were chosen as ± 3 v (measured from the angular position pot), which correspond to $\pm 35°$ angular positions. The initial motion of the arm starts from the 0 v position, and moves towards the +3 v bound.

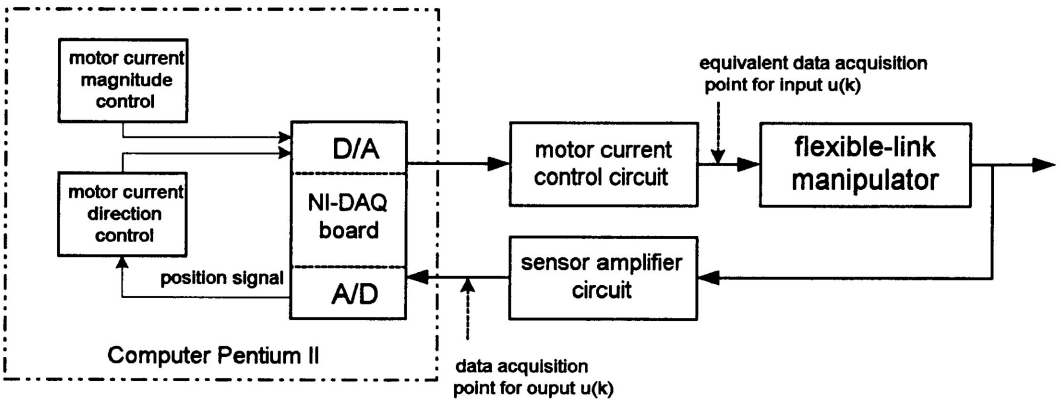

Figure 2-9. The schematic diagram for the bounded position experimental setup.

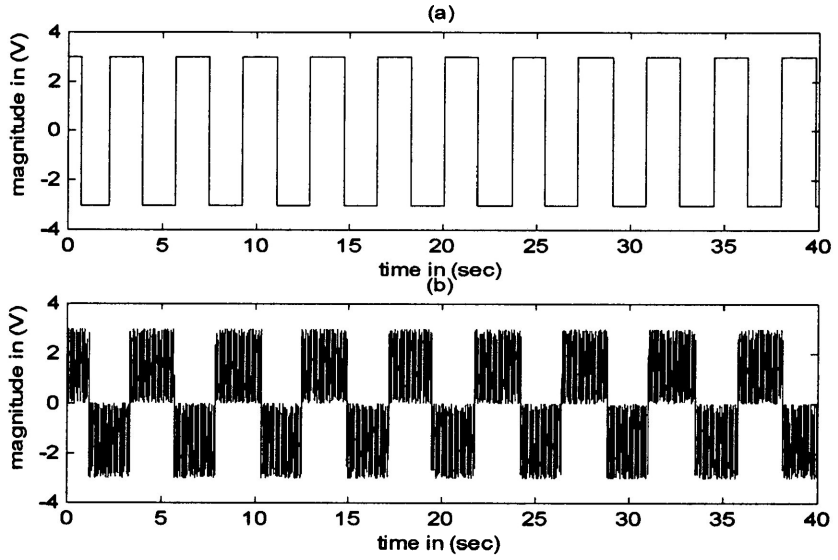

Figure 2-10. The typical exciting signals used for the bounded position experiments. (a) constant current magnitude. (b) random current magnitude.

Two types of the current magnitudes were used, namely random and constant. Figure 2-10a gives a typical resultant exciting signal when the current magnitude is a constant of 1.5 A. It behaves similarly as the square waveform in the open-loop experiment. Figure 2-10b shows a typical resultant exciting signal when the current magnitude varies randomly between 0 A and

1.5 A. It has a similar effect as the periodic random waveform in the open-loop experiment.

The identification results for the bounded position experiment are presented in Table 2-3. Figures 2-11 and 2-12 show the validation results for a model identified using the data with a constant magnitude of the motor current. The following observations can be drawn:

1. For the bounded position experiment, a stable model is easier to obtain than the open-loop experiment.

2. The bounded position experiments with a constant magnitude result in a more accurate model than those with a random current magnitude.

Table 2-3. The identification results for the bounded open-loop experiments

data code	stable system orders	minimum DMV error					
		n_x	δ_1	δ_2	δ_3	δ_4	$\bar{\delta}$
B_dat1	9,10,11,17	17	0.3363	0.4001	0.7528	0.3192	0.4521
B_dat2	10,12,34	34	0.1603	0.3304	0.5614	0.2277	0.3200
B_dat3	7,8,12,18	18	0.1008	0.3505	0.5534	0.2498	0.3136
B_dat4	10,12,26,27,29	12	0.1402	0.3455	0.6020	0.2585	0.3365
B_dat5	8,10,12,14,15,24,26,27	24	0.1015	0.3288	0.5316	0.2088	0.2924
B_dat6	10,12,14,17,18,20,34,35	34	0.0613	0.3207	0.5342	0.2170	0.2833
B_dat7	10,16	10	0.2664	0.4141	0.7268	0.2571	0.4161
B_dat8	12,29	12	0.1642	0.2118	0.4038	0.1302	0.2275
B_dat9	12,16~19,23,25,27,29,31,33	23	0.0443	0.1488	0.2833	0.0998	0.1440
B_dat10	8,10,12,14,20,24,28	12	0.5359	0.3297	0.6102	0.2677	0.4359
B_dat11	8,10,12,16,23~28,32	24	0.0762	0.2132	0.3467	0.1198	0.1890
B_dat12	8,10,12,16,20~23,28~35	32	0.0506	0.1920	0.3349	0.1234	0.1752

Notes: The detail information about the data code refer to Table A-2 in Appendix A. The critical stable model order included.

3. The DMV results shown in Figure 2-11 show a good agreement between the simulated outputs and measured outputs. But the SFV results in Figure 2-12 give an unstable closed-loop system for the identified model, which is not true in the real system. So, the validation results indicate that the identified model does not correctly reflect the real system.

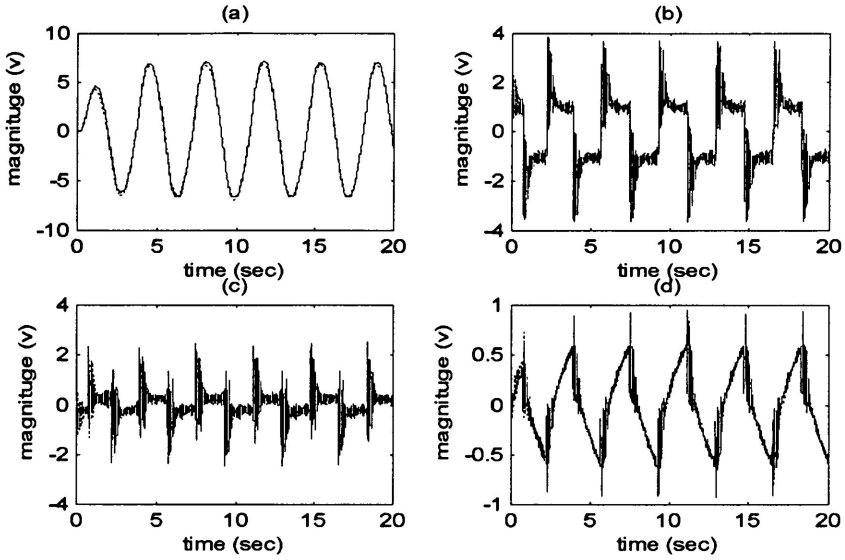

Figure 2-11. The DMV results for an identified model (Ab9_23) derived from the bounded position experiments.

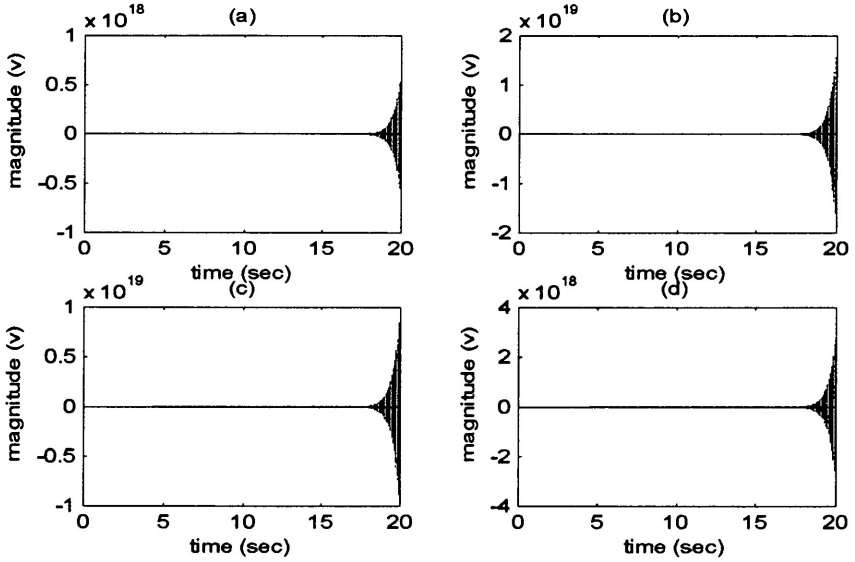

Figure 2-12. The SFV results for an identified model (Ab9_23) derived from the bounded position experiments.

By a careful study of the system, it was noted that the system exhibits some nonlinearity, such as Coulomb friction. In order to reduce the influence of the system nonlinearity, the closed-loop experiment was devised.

2.4.3 Closed-loop Experiments

The system setup for the closed-loop experiments is shown in Figure 2-13. Two types of reference signals for the angular position were chosen. They are square waveform and varying square waveform. For the closed-loop experiments, the magnitude of the reference signals is chosen to be the maximum position desired. The width of the pulse is selected such that the angular position has settled at the reference position before the next bump is applied.

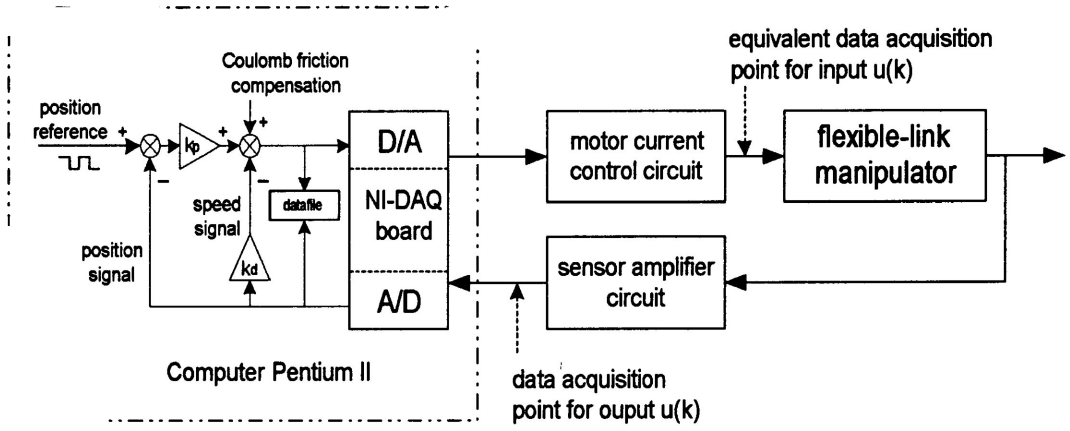

Figure 2-13. The schematic diagram for the closed-loop experimental setup.

It was noted that the Coulomb friction has a significant effect on the rigid body motion. In order to incorporate the Coulomb friction, the approach suggested in [25] is employed in the closed-loop experiments. Based on the measurements, it was found that to overcome the Coulomb friction, an extra effort of about 0.4A motor current is needed; therefore, the 0.8 v Coulomb friction compensation effort was added to the magnitude of current control signal during the data acquisition. Since the ORSE algorithm is based on the assumption of linear

time-invariant systems, this 0.8 v compensation signal must be subtracted from the control signal to have the system input. Consequently, the model identified in this way will not include the system dynamics of the Coulomb friction part.

The proportional gain and derivative gain are $k_p = 1.0$ and $k_d = 2.8$, respectively. Numerous data with different payloads are collected for system identification. Some identification results from the closed-loop experiments are recorded in Table 2-4. Figures 2-14 and 2-15 show the validation results of DMV and SFV for a typical identified model.

1. As shown in Table 2-4. It is easier to obtain a stable model using the closed-loop experiment than using the open-loop experiment.

Table 2-4. The identification results for the closed-loop experiments

data code	stable system order	minimum DMV error					
		n_x	δ_1	δ_2	δ_3	δ_4	$\bar{\delta}$
C_dat1	7~14,17,18,20,22~36	28	0.1431	0.5099	0.7492	0.2981	0.4251
C_dat2	7~11,21~35	35	0.1061	0.4774	0.6506	0.2957	0.3745
C_dat3	7,16,18~20,22~35	18	0.0735	0.4242	0.6675	0.2136	0.3447
C_dat4	7~9,11,16~18,20~35	24	0.1199	0.4600	0.6441	0.2967	0.3802
C_dat5	7,12~35	22	0.0678	0.4949	0.6489	0.2957	0.3768
C_dat6	7~10,14~18,20,21~26,28~35	29	0.0656	0.5164	0.6237	0.2540	0.3649
C_dat7	10,11,14~16,20~28,32~35	34	0.0862	0.2506	0.3230	0.1858	0.2114
C_dat8	10,14,16,27,29,34,35	29	0.1243	0.2192	0.3244	0.1830	0.2128
C_dat9	7~9,14~18,20,22,28,29,35	22	0.1434	0.4993	0.5770	0.2484	0.3670
C_dat10	7,14~22,24~30,32,34,35	15	0.1455	0.4246	0.5419	0.2453	0.3393
C_dat11	7,14~20,24,26~28,30~35	26	0.0584	0.4287	0.5507	0.2533	0.3228
C_dat12	7~10,19~24,27,28,30,32~35	32	0.1064	0.5197	0.6191	0.3303	0.3939
C_dat13	7,8,15~18,22~~28,30~35	28	0.0943	0.5236	0.5796	0.3365	0.3834
C_dat14	7,9,15~18,20,22,24~30,32,34	32	0.0663	0.5049	0.6137	0.2545	0.3599

Notes: The detail information about the data code refer to Table A-3 in Appendix A

2. Compared with the results in the open-loop experiment, the model accuracy for the angular position is much improved.

3. For the overall model accuracy, the models identified by the closed-loop experiment are better in terms of the SFV and slightly worse in terms of the DMV than those from the open-loop experiment.

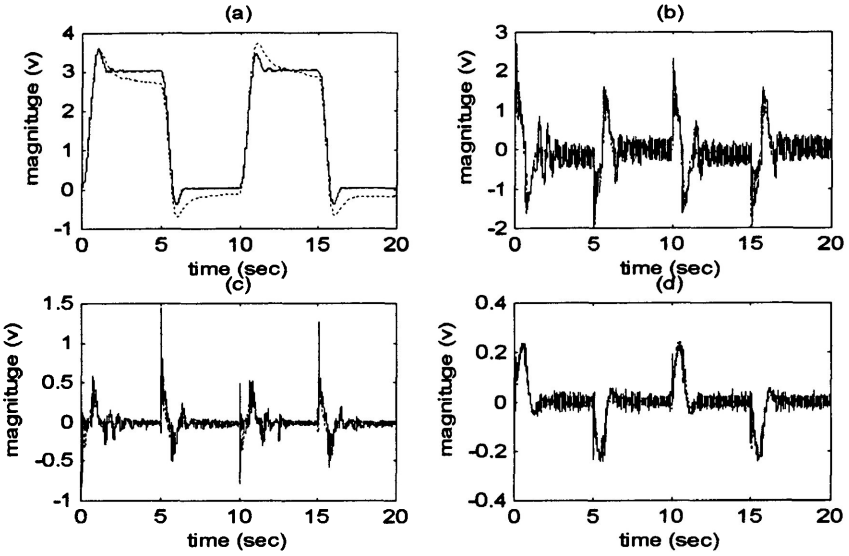

Figure 2-14. The DMV results for an identified model (Ac2_35) derived from the closed-loop experiments.

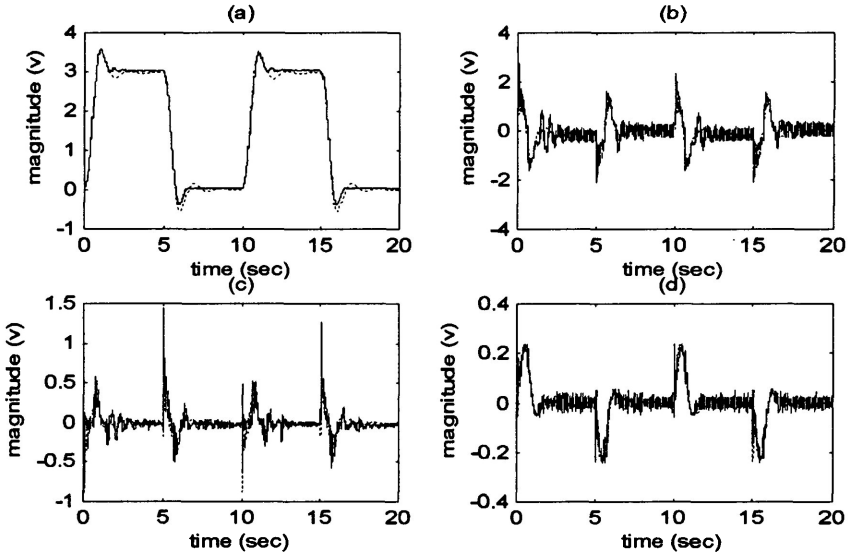

Figure 2-15. The SFV results for an identified model (Ac2_35) derived from the closed-loop experiments.

A disadvantage of the closed-loop experiment is that the exciting signal type can not be directly controlled. A question arises naturally whether the system structural modes can be fully excited in the closed-loop experiment. To address this concern, the frequency responses of the identified model by the closed-loop experiment were analyzed and a sample results are shown in Figure 2-16.

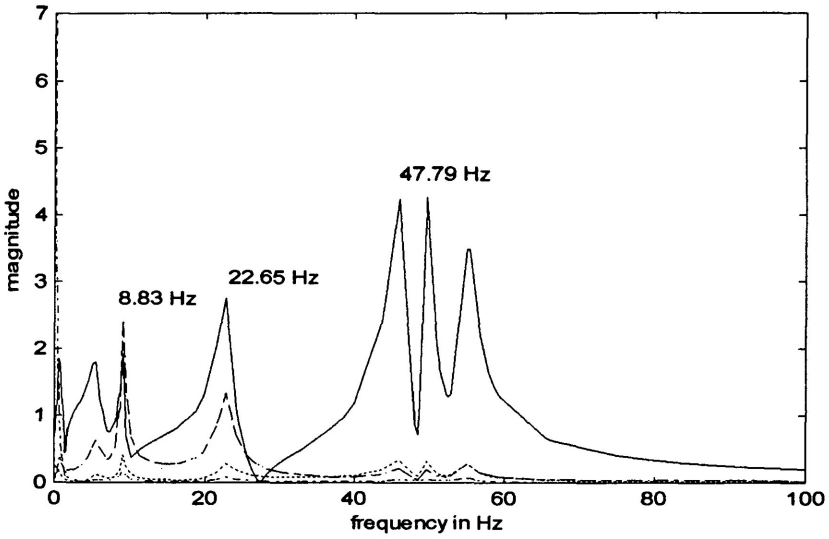

Figure 2-16. The frequency response of an identified model (Ac3_18) derived from the closed-loop experiments.

From the frequency responses, two conclusions can be drawn. First, there are only three significant structural modes present in the responses, and the peaks representing the structural modes coincide with the analytical prediction. Second, the structural modes have stronger presence in the responses of the strain gauges than in the angular position and speed.

2.5 Conclusions

Base on the experimental results, the following conclusions can be drawn:

1. Although the ORSE algorithm is very effective in identifying linear systems, noises and nonlinearity could significantly reduce the accuracy of the identified model.

2. The system under study contains nonlinearity that cannot be neglected. As the ORSE algorithm identifies a linear model, the identified model is a linear approximation of the real system.

3. To obtain the best identification result, the data need to be preprocessed as following:

   (1) The biases presented in the output signals must be removed. In addition, the strain gauge signals have to be forced to zero mean.

   (2) The initial outputs should be set to zero, i.e. $y(1) = \begin{bmatrix} 0 & 0 & 0 & 0 \end{bmatrix}^T$

   (3) The output signals were passed through a low-pass filter to reduce the noise level. A second-order Butterworth low-pass filter with a cutoff frequency of 50 Hz was used. The selection of 50 Hz as the cutoff frequency was based on the fact that the highest structural mode excited by the motor rotation is the third vibratory mode whose natural frequency is about 48 Hz.

   (4) All the output signals were scaled to ensure that their maximum magnitudes equal the maximum magnitude of the input. After the matrix $\bar{C}$ was obtained, an unscale operation was used to have a properly scaled matrix $\bar{C}$.

4. The identified models obtained from the data with 300 Hz sampling rate give better accuracy than those from 500 Hz sampling rate.

Tables 2-5 and 2-6 record some additional information of the special and typical identified models that would be used in the following chapters.

Table 2-5. The special models for evaluations

model code	Data used for identification	order	stability
Ac3_22c	C_dat3 without removal of Coulomb friction compensation	22	stable
Ac11_18c	C_dat11 without removal of Coulomb friction compensation	18	stable
Ac3_21u	C_dat3 with removal of Coulomb friction compensation	21	unstable

Table 2-6. The list of the typical identified stable models			
model code	data used for identification	order	experiment
Ao1_36	first 1500 samples of O_dat1	36	Open-loop
Ao2_19	first 3000 samples of O_dat2	19	Open-loop
Ao5_12	first 1500 samples of O_dat3	12	Open-loop
Ao6_28	first 3000 samples of O_dat4	28	Open-loop
Ao9_24	first 1500 samples of O_dat5	24	Open-loop
Ao10_12	first 1500 samples of O_dat6	12	Open-loop
Ao14_31	first 1500 samples of O_dat7	31	Open-loop
Ac1_28	first 4800 samples of C_dat1	28	Closed-loop
Ac2_35	first 6000 samples of C_dat2	35	Closed-loop
Ac3_18	first 6000 samples of C_dat3	18	Closed-loop
Ac4_24	first 6000 samples of C_dat4	24	Closed-loop
Ac5_22	first 4800 samples of C_dat5	22	Closed-loop
Ac6_29	first 6000 samples of C_dat6	29	Closed-loop
Ac7_34	first 6000 samples of C_dat7	34	Closed-loop
Ac8_29	first 6000 samples of C_dat8	29	Closed-loop
Ac9_22	first 6000 samples of C_dat9	22	Closed-loop
Ac10_15	first 4800 samples of C_dat10	15	Closed-loop
Ac11_26	first 6000 samples of C_dat11	26	Closed-loop
Ac12_32	first 4800 samples of C_dat12	32	Closed-loop
Ac13_28	first 6000 samples of C_dat13	28	Closed-loop
Ac14_32	first 6000 samples of C_dat14	32	Closed-loop

Chapter 3

Model Reduction and Updating

A feature of the ORSE algorithm is that the model must be properly overparameterized in order to capture the dynamics of systems. This need arises due to the effects of irregularities such as measurement noise and system nonlinearity. An overparameterized model contains both structural or system modes and computational modes. The order of the estimated model must be reduced to eliminate the computational modes and insignificant system modes to ease the controller implementation. The reduced model must be updated to correct errors caused by truncation of some modes.

The procedure proposed in [20] employs the balanced realization (BR) technique to reduce a model. The BR technique transfer the model into an internally balanced form such that the controllability and observability of each mode is indicated by its corresponding diagonal element of the joint Gramain matrix or Hankel singular value [26]. The modes with smaller Hankel singular values are considered less important and eliminated to produce a reduced-order model. There are two major problems with the model reduction through the BR technique. First, the BR technique requires that the model must be asymptotically stable or the eigenvalues of the transition matrix lie inside the unit circle. Second, determining a threshold for insignificant Hankel singular values is more or less a subjective judgement. For model updating, the Least Squares (LS) model updating algorithm employed in [20] modifies iteratively the reduced model using the gradient information. The LS model updating technique assumes that the model to be updated is sufficiently accurate. In practice, this assumption is not always valid especially with a truncated model. Moreover, the LS model updating algorithm needs to find the pseudo-

inverse of a large size matrix which is very ill-conditioned.

As the system under study involves rigid body motion and lightly damping modes, the identified model is likely to be unstable. Thus, the procedure for model reduction and updating proposed in [20] cannot be applied. As a result, this study proposes to conduct the model reduction in the modal coordinates. After an eigendecomposition is conducted on the oversized transition matrix, the importance of individual modes is determined and less significant modes are eliminated. In the presence of the unstable modes , the suggested approaches in [27] can be employed to correct or force the unstable modes into stable modes. To quantify the contribution of individual modes, a new index, referred to as the Modal Response Magnitude (MRM), is proposed. For the system under study, the experimental results show that MRM index is more reliable than the previously proposed indices such as the Mode Singular Value (MSV) in [18].

The low efficiency of the updating algorithm proposed in [20] is due to simultaneously modifying all the elements of the system matrices using the gradient information. For such a large dimension optimization problem, the solution is likely to converge to a local minimum. Expressing the transition, input, and output matrices in the modal coordinates, the new method developed in this study recalculates either the input matrix or output matrix while keeping the other two unchanged. The calculation is done by solving a non-iterative LS problem.

This chapter is organized as follow: Section 1 introduces a new procedure of model reduction and updating. Section 2 presents the sample results by using this new procedure. Section 3 summarizes the main conclusions.

3.1 A New Procedure for Model Reduction and Updating

This section presents the development of a new procedure to reduce the order of an overparameterized identified model and correct errors caused by model truncation. The key feature of this proposed procedure is that the model reduction and updating are conducted in the modal coordinates. An eigendecomposition is conducted on the identified transition matrix

$$\bar{A} = \Psi \Lambda \Psi^{-1} \tag{3-1}$$

where

$$\Psi = \left[\begin{array}{ccccccc} \psi_1 & \psi_2 & \cdots & \psi_{n_1-1} & \psi_{n_1} & \psi_{n_1+1} & \cdots & \psi_n \end{array} \right] \in C^{n \times n}$$

is the eigenvector matrix and

$$\Lambda = \mathrm{diag} \left[\begin{array}{ccccccc} \lambda_1 & \lambda_2 & \cdots & \lambda_{n_1-1} & \lambda_{n_1} & \lambda_{n_1+1} & \cdots & \lambda_n \end{array} \right] \in C^{n \times n}$$

is the eigenvalue matrix. In this study, $\mathrm{C}^{i \times j}$ represents the $i \times j$ complex matrix space. It is assumed that there are $n_1/2$ pairs of complex eigenvalues and eigenvectors, i.e., $\lambda_{i+1} = \lambda_i^*$, $\psi_{i+1} = \psi_i^*$ for $i = 1, 3, \cdots, n_1 - 1$ where the superscript * denotes complex conjugate. The remaining $n - n_1$ eigenvalues and eigenvectors are real. Defining a set of new states in the modal coordinates as

$$\eta(k) = \Psi^{-1} z(k) \tag{3-2}$$

then the state-space model becomes

$$\begin{aligned} \eta(k+1) &= \Lambda \eta(k) + \hat{B} u(k) \\ \hat{y}(k) &= \hat{C} \eta(k), \end{aligned} \tag{3-3}$$

where

$$\begin{aligned} \hat{B} &= \Psi^{-1} \bar{B} = \left[\begin{array}{ccccccc} \hat{b}_1 & \hat{b}_2 & \cdots & \hat{b}_{n_1-1} & \hat{b}_{n1} & \hat{b}_{n_1+1} & \cdots & \hat{b}_n \end{array} \right]^T \in C^{n \times 1} \\ \hat{C} &= \bar{C} \Psi = \left[\begin{array}{ccccccc} \hat{c}_1 & \hat{c}_2 & \cdots & \hat{c}_{n_1-1} & \hat{c}_{n1} & \hat{c}_{n_1+1} & \cdots & \hat{c}_n \end{array} \right] \in C^{m \times n}. \end{aligned}$$

It is noted that complex quantities appear as pairs, i.e., $\hat{b}_{i+1} = \hat{b}_i^*$ and $\hat{c}_{i+1} = \hat{c}_i^*$ for $i = 1, 3, \cdots, n_1 - 1$. As the state variables in the modal coordinates are decoupled, elimination of those computational and insignificant modes has least impact to the remaining state variables.

An important question is how to distinguish the system modes from the computational modes. It is reasonable to assert that the computational modes contribute little to the system responses. To characterize the contribution of individual modes to the output responses, a quantitative measure is needed. Two indices are introduced in [18] to quantify the contribution of individual modes to a pulse response. Specifically the Mode Singular Value (MSV) is defined

as

$$\text{MSV}_i = \sqrt{|\hat{c}_i|(1+|\lambda_i|+|\lambda_i^2|+\cdots+|\lambda_i^{K-2}|)|\hat{b}_i|}. \tag{3-4}$$

A mode with a large magnitude of the MSV is considered to have a significant contribution to the pulse response. The computational modes and insignificant structural modes are expected to have small MSVs. The MSV may be misleading, because it only considers the contributions of individual modes to a pulse input. For example, the pulse response of a mode with heavy damping dies quickly even if the mode is one of the significant system modes. When the system is persistently excited, the contribution of the heavily damped system mode may not be neglected. To overcome this shortcoming of the MSV, an alternative measure is proposed in this study. The system responses are a sum of the modal responses, i.e.,

$$\hat{y}(k) = \sum_{i=1,3}^{n_1-1} \hat{y}_{\eta_i}(k) + \sum_{i=n_1+1}^{n} \hat{y}_{\eta_i}(k) \tag{3-5}$$

where $\hat{y}_{\eta_i}(k) \in R^{m\times 1}$ is the modal response of the i-th mode. For the i-th complex mode, $\hat{y}_{\eta_i}(k)$ is evaluated by

$$\begin{aligned} \begin{bmatrix} \eta_i(k+1) \\ \eta_i^*(k+1) \end{bmatrix} &= \begin{bmatrix} \lambda_i & 0 \\ 0 & \lambda_i^* \end{bmatrix} \begin{bmatrix} \eta_i(k) \\ \eta_i^*(k) \end{bmatrix} + \begin{bmatrix} \hat{b}_i \\ \hat{b}_i^* \end{bmatrix} u(k) \\ \hat{y}_{\eta_i}(k) &= \begin{bmatrix} \hat{c}_i & \hat{c}_i^* \end{bmatrix} \begin{bmatrix} \eta_i(k) \\ \eta_i^*(k) \end{bmatrix}, \quad i = 1,3,\cdots,n_1-1. \end{aligned} \tag{3-6}$$

For the i-th real mode, $\hat{y}_{\eta_i}(k)$ is evaluated by

$$\begin{aligned} \eta_i(k+1) &= \lambda_i \eta_i(k) + \hat{b}_i u(k) \\ \hat{y}_{\eta_i}(k) &= \hat{c}_i \eta_i(k), \quad i = n_1+1,\cdots,r \end{aligned} \tag{3-7}$$

The maximum contribution of the i-th mode to the total response can be evaluated by a Modal Response Magnitude (MRM) defined as

$$\text{MRM}_i = \max\left(\sum_{k=1}^{K} |\hat{y}_{\eta_i}(k)|/K\right), \quad i = 1,3,\cdots,n_1-1,n_1+1,\cdots,r \tag{3-8}$$

The MRM computes the maximum means of the absolute modal responses to the actual input. As the modes with small MRMs can be considered to be insignificant for a given input, they are eliminated to produce a lower-order model that still preserves the basic properties of the system. The MRMs are more meaningful than the Hankel singular values produced by the BR technique as each MRM is related to its modal response. With the MRMs, knowledge of the system dynamics from an analytical model or modal testing can be easily incorporated in decision making.

The reduced-order model has a triplet

$$\begin{aligned}
\Lambda_r &= \text{diag}\left[\begin{array}{cccccccc} \lambda_1 & \lambda_2 & & \lambda_{n_1'-1} & \lambda_{n_1} & \lambda_{n_1'+1} & & \lambda_{n'} \end{array}\right] \in C^{n'\times n'} \\
\hat{\mathrm{B}}_r &= \left[\begin{array}{cccccccc} \hat{b}_1 & \hat{b}_2 & & \hat{b}_{n'-1} & \hat{b}_{n_1'} & \hat{b}_{n_1'+1} & & \hat{b}_{n'} \end{array}\right]^T \in C^{n'\times 1} \\
\hat{\mathrm{C}}_r &= \left[\begin{array}{cccccccc} \hat{c}_1 & \hat{c}_2 & & \hat{c}_{n_1'-1} & \hat{c}_{n_1'} & \hat{c}_{n_1'+1} & & \hat{c}_{n'} \end{array}\right] \in C^{m\times n'}
\end{aligned} \tag{3-9}$$

where n' denotes the order of the reduced model and n_1' denotes the number of complex modes that have been retained. The reduced model is expected to be less accurate than the original model. This problem can be corrected by recalculating the reduced matrices $\hat{\mathrm{B}}$ or $\hat{\mathrm{C}}$. Since the elements in the triplet of the reduced model are complex, this will complicate the computation work. In order to avoid this problem, the triplet is obtained in real values by the following way. First, a simulated output $\hat{y}(k)$ is generated using the actual input $u(k)$ and the reduced-order model, Λ_r, $\hat{\mathrm{B}}_r$, and $\hat{\mathrm{C}}_r$. It should be noted that the generated $\hat{y}(k)$ is in real values. Applying the ORSE algorithm to the actual input $u(k)$ and the simulated output $\hat{y}(k)$ results in a new set of triplet $\bar{\mathrm{A}}_r$, $\bar{\mathrm{B}}_r$, and $\bar{\mathrm{C}}_r$ in real values. Now the reduced-order model is given as

$$\begin{aligned}
z_r(k+1) &= \bar{\mathrm{A}}_r z_r(k) + \bar{\mathrm{B}}_r u(k) \\
\hat{y}(k) &= \bar{\mathrm{C}}_r z_r(k)
\end{aligned} \tag{3-10}$$

where $z_r \in R^{n'\times 1}$.

The $\bar{\mathrm{B}}_r$ matrix can be recalculated by solving the following LS problem.

$$\begin{cases} \min\limits_{\bar{\mathrm{B}}_r} \sum\limits_{k=1}^{K} \|\tilde{y}(k) - \hat{y}(k)\|_2 \\ \text{subject to: } \bar{\mathrm{A}}_r \text{ and } \bar{\mathrm{C}}_r \text{ given in (3-10).} \end{cases} \tag{3-11}$$

The matrix $\bar{\mathrm{B}}_r$ is of the form

$$\bar{\mathrm{B}}_r = \begin{bmatrix} \bar{b}_{r_1} \\ \bar{b}_{r_2} \\ \cdot \\ \\ \bar{b}_{r_{n'}} \end{bmatrix} \in R^{n' \times 1} \tag{3-12}$$

where $\bar{b}_{r_i}$ is the $i-$th elements of updated matrix $\bar{\mathrm{B}}_r$ for $i = 1, 2, \cdots, n'$. For the single input case, i.e., $u(k)$ is a scalar, the response is computed by

$$\begin{aligned} z_r(k+1) &= \bar{\mathrm{A}}_r z_r(k) + \sum_{i=1}^{n'} I_{n'i} \bar{b}_{r_i} u(k) \\ \tilde{y}(k) &= \bar{\mathrm{C}}_r z_r(k) \end{aligned} \tag{3-13}$$

where $I_{n'i}$ is the column vector of unity matrix $I_{n'} \in R^{n' \times n'}$ for $i = 1, 2, \cdots n'$. Denoting the response to $I_{n'i} u(k)$ as $\tilde{y}_{b_{r_i}}(k)$, then

$$\begin{aligned} z_{b_{r_i}}(k+1) &= \bar{\mathrm{A}}_r z_{b_{r_i}}(k) + I_{n'i} u(k) \\ \hat{y}_{b_{r_i}}(k) &= \bar{\mathrm{C}} z_{b_{r_i}}(k). \end{aligned} \tag{3-14}$$

By the superposition

$$\tilde{y}(k) = \sum_{i=1}^{n'} \hat{y}_{b_{r_i}}(k) \bar{b}_{r_i} = \phi(k) \bar{\mathrm{B}}_r, \tag{3-15}$$

where

$$\phi(k) = \begin{bmatrix} \hat{y}_{b_{r_1}} & \hat{y}_{b_{r_2}} & & \hat{y}_{b_{r_{n'}}} \end{bmatrix}. \tag{3-16}$$

The Least Squares solution for the updated $\bar{\mathrm{B}}_r$ is

$$\bar{\mathrm{B}}_r = \Phi^{+} \tilde{Y}, \tag{3-17}$$

where $\Phi \in R^{K \times n'}$ and $\tilde{Y} \in R^{K \times 1}$ are of the forms

$$\Phi = \begin{bmatrix} \phi(1) \\ \phi(2) \\ \cdot \\ \\ \phi(k) \end{bmatrix} \quad \text{and} \quad \tilde{Y} = \begin{bmatrix} \tilde{y}(1) \\ \tilde{y}(2) \\ \cdot \\ \\ \tilde{y}(k) \end{bmatrix}, \tag{3-18}$$

respectively.

Similarly, the updated $\bar{C}_r$ can be computed by solving the following LS problem.

$$\begin{cases} \min\limits_{\bar{C}_r} \sum\limits_{k=1}^{K} \|\tilde{y}(k) - \hat{y}(k)\|_2 \\ \text{subject to: } \bar{A}_r \text{ and } \bar{B}_r \text{ given by (3-10)} \end{cases} \tag{3-19}$$

The $\bar{C}_r$ matrix is given by

$$\bar{C}_r = \tilde{Y} Z^{+} \tag{3-20}$$

where

$$Z = \begin{bmatrix} Z_r(1) & Z_r(2) & & Z_r(K) \end{bmatrix}. \tag{3-21}$$

In this study, the entire model reduction and updating scheme is implemented in Matlab Program.

3.2 Results of Model Reduction and Updating

Prior knowledge from the analysis of the system dynamics and previous study is a good guide to determine a minimum order of the reduced model. The previous study [16] has shown that the excitation generated by the motor rotation can induce up to the third vibratory mode of the arm. The first three vibratory modes (about 8Hz, 24Hz, and 48Hz for 0g payload) can be represented by 3 pair complex modes, i.e., 6 modes in the state-space model. The rigid motion of the arm may be represented by two or three modes depending on the extent of modelling. Finally the analog filter used in measuring the tachometer signal can be represented by two modes; therefore the system has a minimum order of 10 or 11 approximately.

Three methods are used to obtain a reduced-order model. The first method is referred to as the MRM method by which a reduced-order model is obtained according to the MRM ranking. The second method is referred to as the MRMC method by which the rigid modes are determined by the MRM ranking, and the flexible modes are considered to be the complex modes whose natural frequencies are close to the three known vibratory modes with strong MRM ranking. The third method is named as the MSV method by which the significant modes are selected by the MSV ranking.

The first example of model reduction and updating is an identified model derived from the closed-loop experiment using the varying square waveform as the position reference signal and carrying 0g payload. Its original order is 18. Figures 3-1 and 3-2 show the results of the DMV and SFV of the initial identified model. According to the MSV ranking shown in Table 3-1a, the reduced 11-th order model should retain modes of [1/2, 3/4, 5/6, 7/8, 9/10, 17].

Table 3-1a. The MRM and MSV ranking for the 1st example

Model Ac3_18 (0g payload)

mode number	frequency (Hz)	damping ratio	MRM ranking	MSV ranking
1/2	54.9260	0.0188	10	5
3/4	49.6205	0.0105	9	4
5/6	46.0456	0.0270	7	3
7/8	22.8148	0.0420	5	6
9/10	9.0228	0.0290	6	2
11/12	5.5770	0.1440	4	8
13/14	1.5207	0.2712	8	10
15/16	0.7677	0.3547	3	9
17	----	real	2	1
18	----	real	1	7

Table 3-1b. The model (Ac3_18) reduction and updating results for the 1st example

modes information	procedure stage	validation method	prediction error				
			δ_1	δ_2	δ_3	δ_4	$\bar{\delta}$
keep all modes as is.	Initial	DMV	0.0470	0.4328	0.6800	0.2307	0.3476
		SFV	0.0596	0.5636	0.6538	0.3048	0.3955
7/8,9/10,11/12,15/16,17,18	MRM	DMV	0.0470	0.4625	0.7178	0.2570	0.3711
1/2,3/4,5/6,7/8,9/10,17	MSV	DMV	0.3367	0.6875	0.9436	0.9960	0.7409
5/6,7/8, 9/10,15/16,17,18	MRMC	DMV	0.0470	0.5000	0.7322	0.2738	0.3882
updated from MRMC (Ac3r_10)	Update1	DMV	0.0458	0.4456	0.6892	0.2298	0.3526
		SFV	0.0537	0.5542	0.6747	0.2910	0.3934
further reduced from MRMC (Ac3r_8)	Update2	DMV	0.0458	0.4551	0.6904	0.2307	0.3555
		SFV	0.0537	0.5520	0.6767	0.2906	0.3933

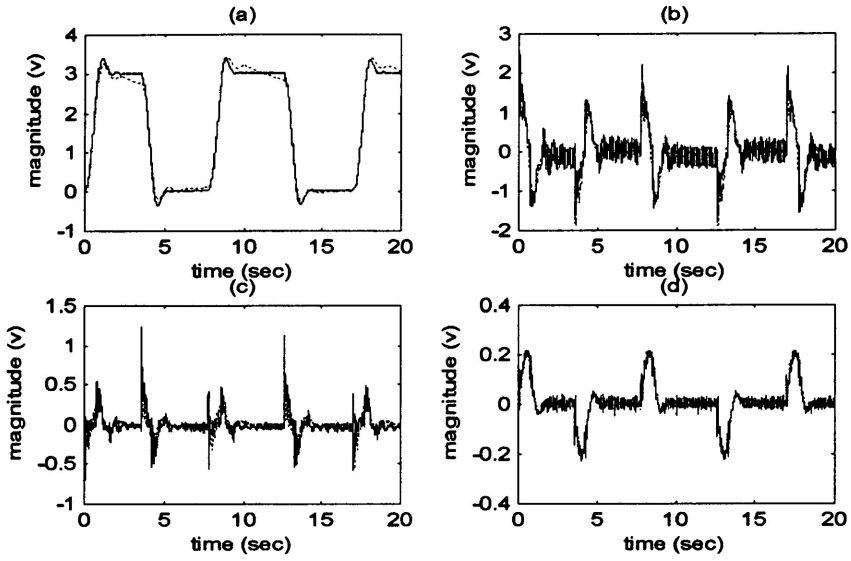

Figure 3-1. The DMV results of the initial identified model (Ac3_18) used for the first example.

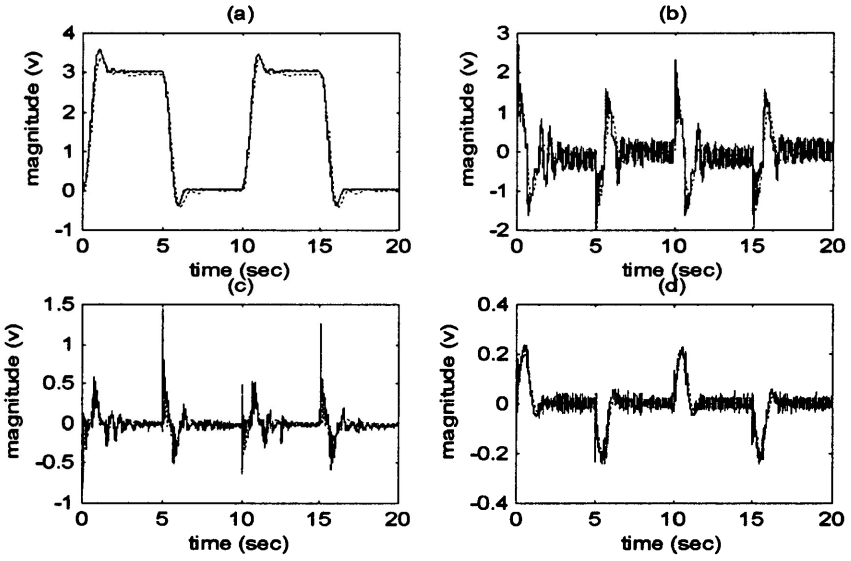

Figure 3-2. The SFV results of the initial identified model (Ac3_18) used for the first example.

Comparing with the errors of the initial identified model in Table 3-1b, the errors of the reduced-order model are increased. The DMV results of this reduced-order model in Figure 3-3 appear a significant deviation from the actual signals, especially the position signal and speed signal. This is because the modes 15/16, and 18 were considered as less important by the MSVs. It was noted that these three modes are related to the rigid motion with heavy damping, in a pulse response, these modes die quickly and thus they have small MSVs.

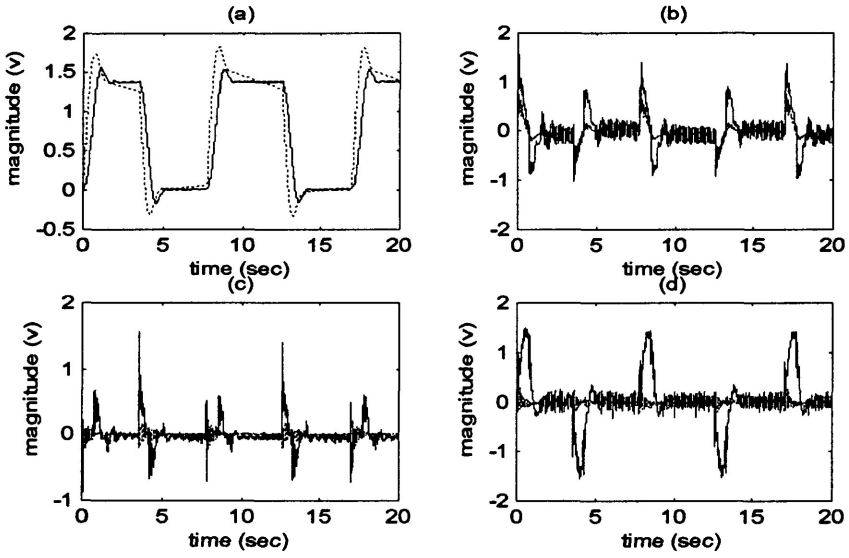

Figure 3-3. The DMV results of the reduced-model obtained from the model (Ac3_18) by retaining modes [1/2,3/4,5/6,7/8,9/10,17] according to the MSV ranking.

On the other hand, according to the MRM ranking in Table 3-1a, the reduced 10-th order model can be obtained by keeping the modes of [7/8, 9/10, 11/12, 15/16, 17, 18]. Table 3-1b shows a slight increase in the prediction errors for this reduced-order model, and its DMV results are shown in Figure 3-4. Clearly, the result of the MRM method is better than that of the MSV method. Figure 3-5 shows the DMV results of the reduced-order model determined by keeping the modes of [5/6, 7/8, 9/10, 15/16, 17, 18], which were selected according to the MRMC method. Like the reduced-order model determined by the MRM ranking, the errors of this reduced model are also slightly increased compared with the errors of the initial model.

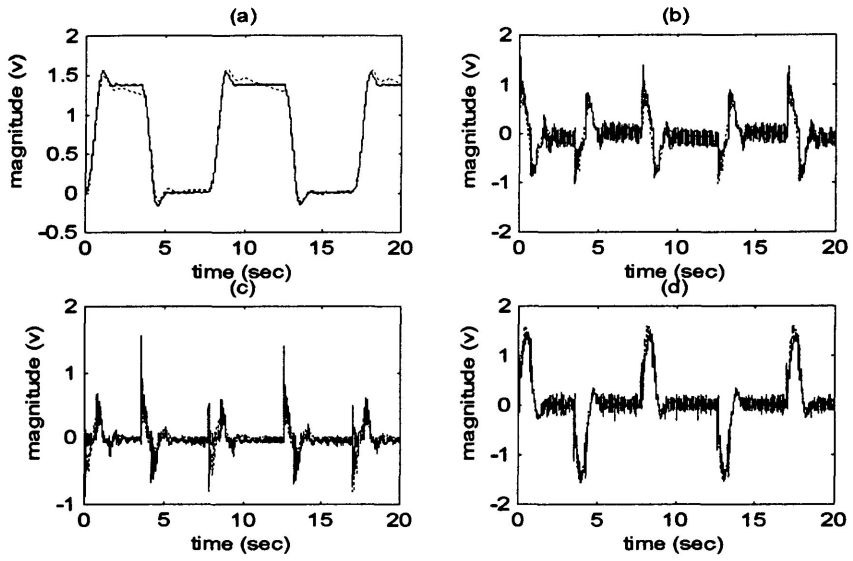

Figure 3-4. The DMV results of the reduced-model obtained from the model (Ac3_18) by retaining modes [7/8,9/10,11/12,15/16,17,18] according to the MRM ranking.

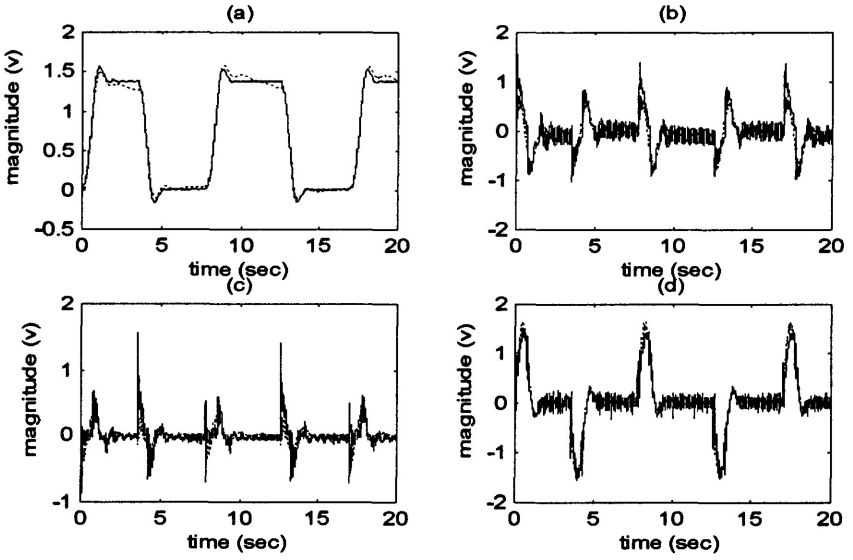

Figure 3-5. The DMV result of the reduced-model obtained from the model (Ac3_18) by retaining modes [5/6,7/8,9/10,15/16,17,18] according to the MRMC method.

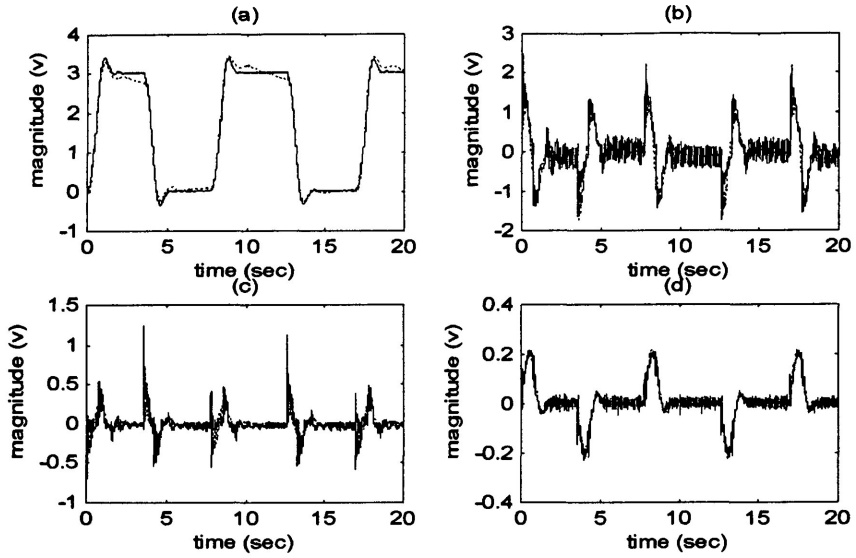

Figure 3-6. The DMV results of the updated reduced-model (Ac3r_10) by retaining modes [5/6,7/8,9/10,15/16,17,18] according to the MRMC method.

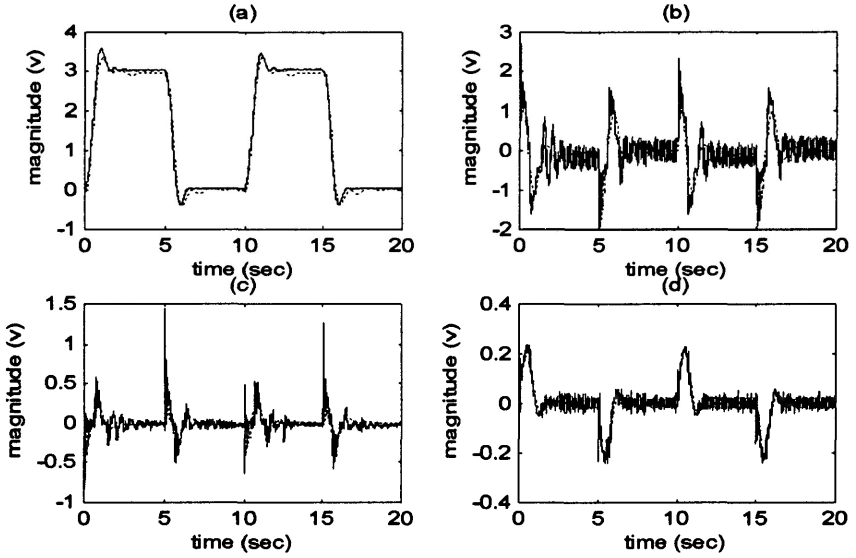

Figure 3-7. The SFV results of the updated reduced-model (Ac3r_10) by retaining the modes [5/6,7/8,9/10,15/16,17,18] according to the MRMC method.

Figures 3-6 and 3-7 show the DMV and SFV results of the updated model conducted from the reduced-order model determined by the MRMC method according to the proposed updating algorithm in the previous section. As shown in Table 3-1, the errors of the updated model are almost the same as those of the initial identified model. The frequency response plot of the updated model in Figure 3-8 shows clearly the first three flexible modes.

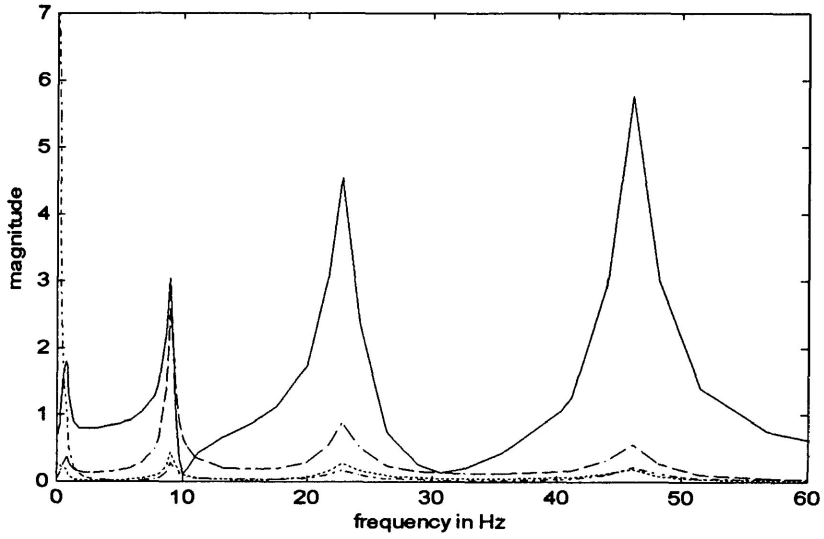

Figure 3-8. The frequency responses of the updated reduced-model (Ac3r_10) by retaining modes [5/6,7/8,9/10,15/16,17,18] according to the MRMC method.

According to the MRMs, the third flexible mode, about 48Hz, is not important. The reduced-order model is further reduced to order 8 by eliminating the third flexible mode. The errors of this further reduced-order model are given in Table 3-1b, and its DMV and SFV results are shown in Figures 3-9 and 3-10. From the results, it can be seen that the third flexible mode indeed is less important.

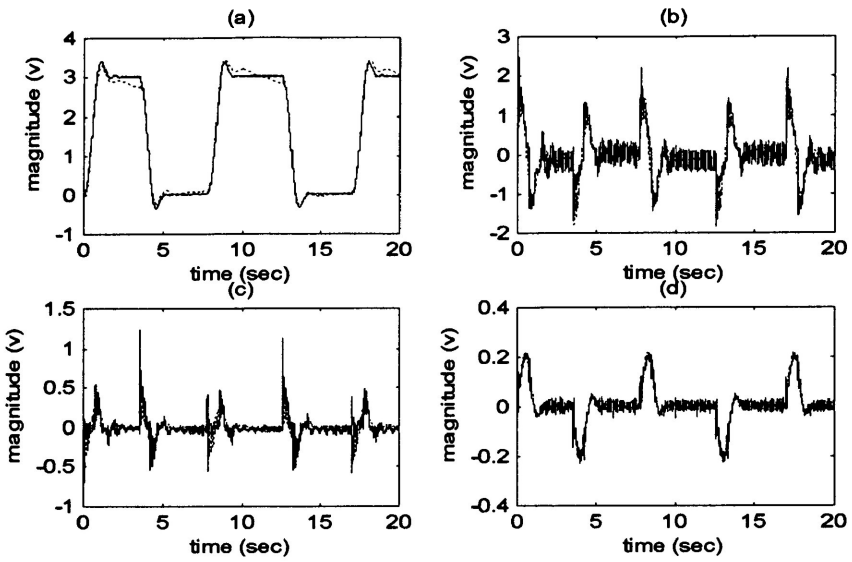

Figure 3-9. The DMV results of the updated reduced-model (Ac3r1_8) by retaining the modes [7/8,9/10,15/16,17,18] according to the MRMC method.

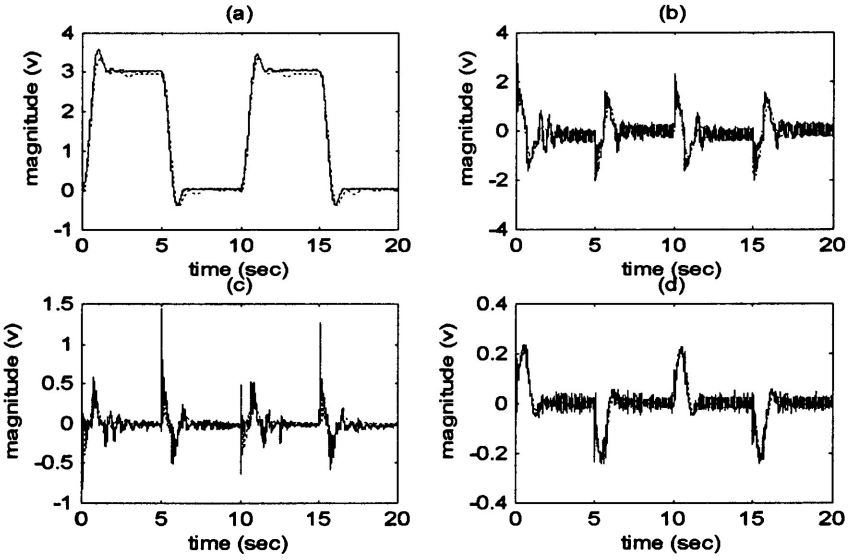

Figure 3-10. The SFV results of the updated reduced-model (Ac3r1_8) by retaining the modes [7/8, 9/10,15/16,17, 18] according to the MRMC method.

As the second example, an identified model derived from the closed-loop experiments on the system with a payload of 300g was used. The DMV and SFV results for each stage are shown in Figures 3-11 to 3-17, and the quantitative errors and ranking of the MSV and MRM are recorded in Tables 3-2a and 3-2b, respectively. The results are similar to the first example.

Table 3-2a. The MRM and MSV ranking for the 2nd example

Model Ac11_26 (300g payload)

mode number	frequency (Hz)	damping ratio	MRM Ranking	MSV ranking
1/2	58.09	0.01	10	10
3/4	52.31	0.01	9	9
5/6	47.53	0.01	8	6
7/8	41.32	0.01	11	7
9/10	35.45	0.02	13	11
11/12	22.15	0.08	4	2
13/14	18.69	0.03	14	14
15/16	10.92	0.08	7	5
17/18	7.64	0.04	12	13
19/20	4.01	0.2	6	12
21/22	1.17	0.45	2	4
23/24	0.60	0.49	1	3
25	----	real	3	1
26	----	real	5	8

Table 3-2b. The model (Ac11_26) reduction and updating results for the 2nd example

modes information	procedure stage	validation method	prediction error				
			δ_1	δ_2	δ_3	δ_4	$\bar{\delta}$
keep all modes as is	Initial	DMV	0.0467	0.4268	0.5487	0.2674	0.3224
		SFV	0.0721	0.4707	0.5321	0.2513	0.3316
11/12,19/20,21/22,23/24,25,26	MRM	DMV	0.0467	0.4312	0.5678	0.2788	0.3311
5/6,11/12,15/16,21/22,23/24,25	MSV	DMV	0.3046	0.4820	0.5703	0.4250	0.4455
5/6,11/12,15/16, 23/24, 25, 26	MRMC	DMV	0.0546	1.5642	1.2014	0.3464	0.7917
from MRM (Ac11r_10)	Update1	DMV	0.0414	0.4209	0.5291	0.2551	0.3116
		SFV	0.0749	0.4619	0.5222	0.2330	0.3230
from MRMC (Ac11r1_10)	Update2	DMV	0.0430	0.4899	0.6115	0.2710	0.3539
		SFV	0.0745	0.5069	0.5959	0.2590	0.3591

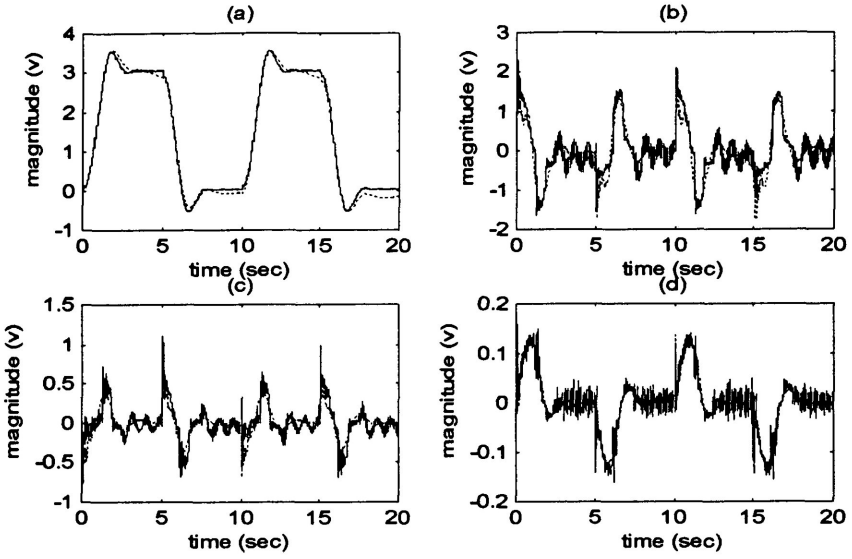

Figure 3-11. The DMV results of the initial identified model (Ac11_26) used for the second example.

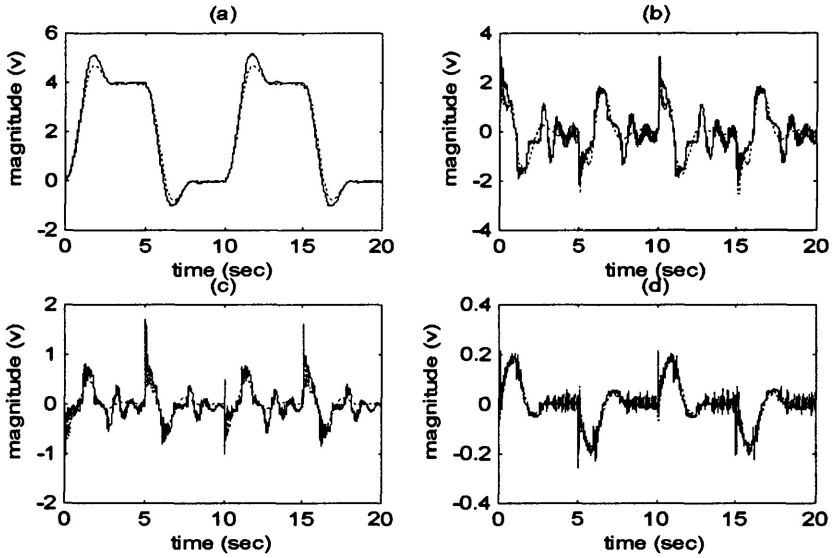

Figure 3-12. The SFV results of the initial identified model (Ac11_26) used for the second example.

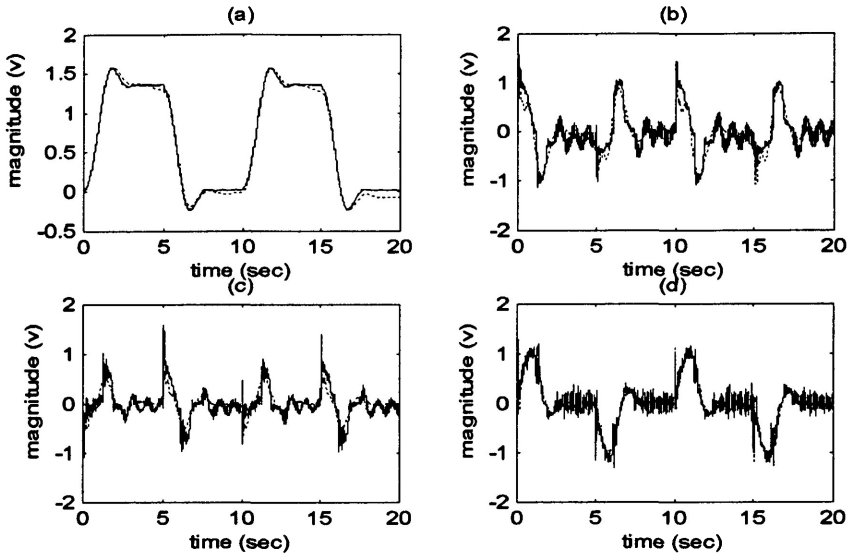

Figure 3-13. The DMV results of the reduced-model obtained from the model (Ac11_26) by retaining modes [11/12,19/20,21/22,23/24,25,26] according to the MRM ranking.

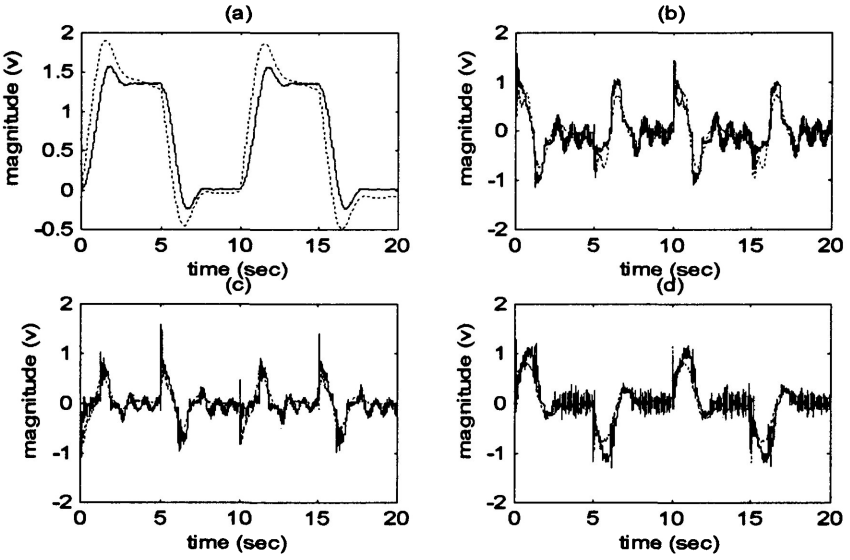

Figure 3-14. The DMV results of the reduced-model obtained from the model (Ac11_26) by retaining modes [5/6,11/12,15/16,21/22,23/24,25] according to the MSV ranking.

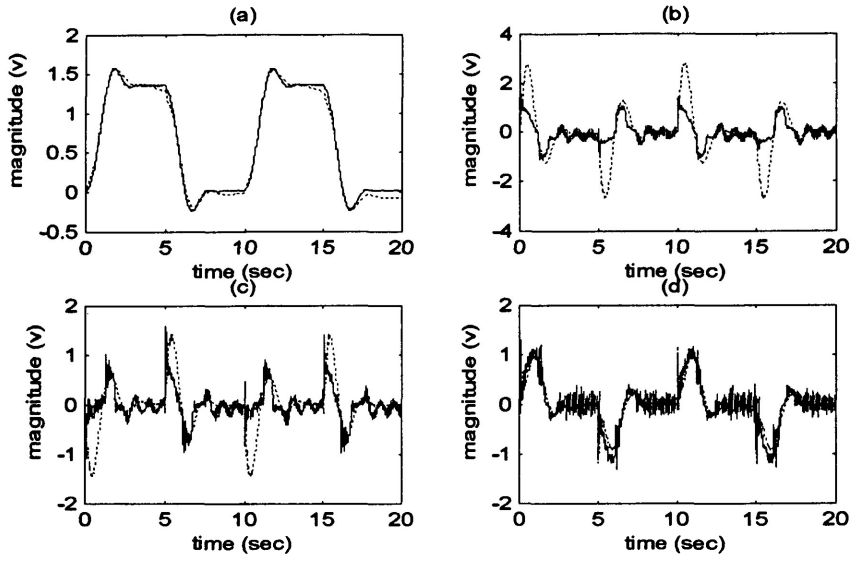

Figure 3-15. The DMV results of the reduced-model of the model (Ac11_26) by retaining modes [5/6,11/12,15/16,23/24,25,26] according to the MRMC method.

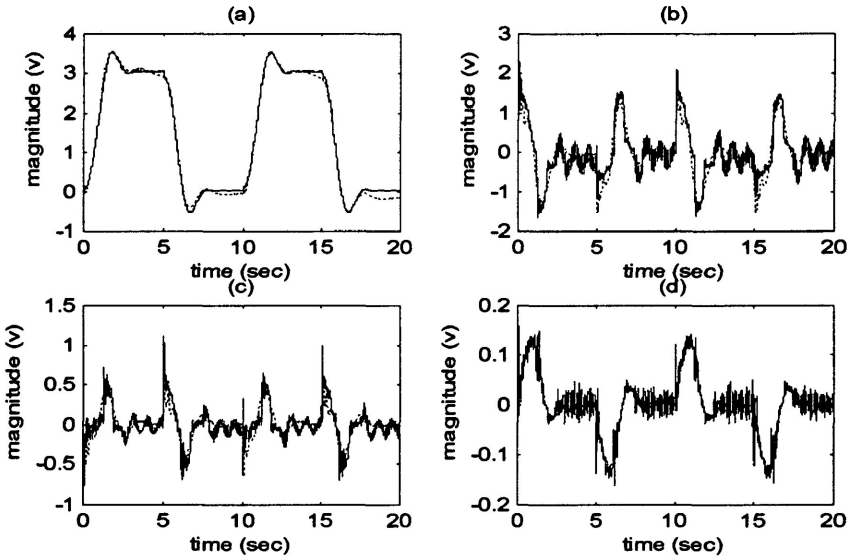

Figure 3-16. The DMV results of the updated reduced-model (Ac11r_10) by retaining modes [11/12,19/20,21/22,23/24,25,26] according to the MRM ranking.

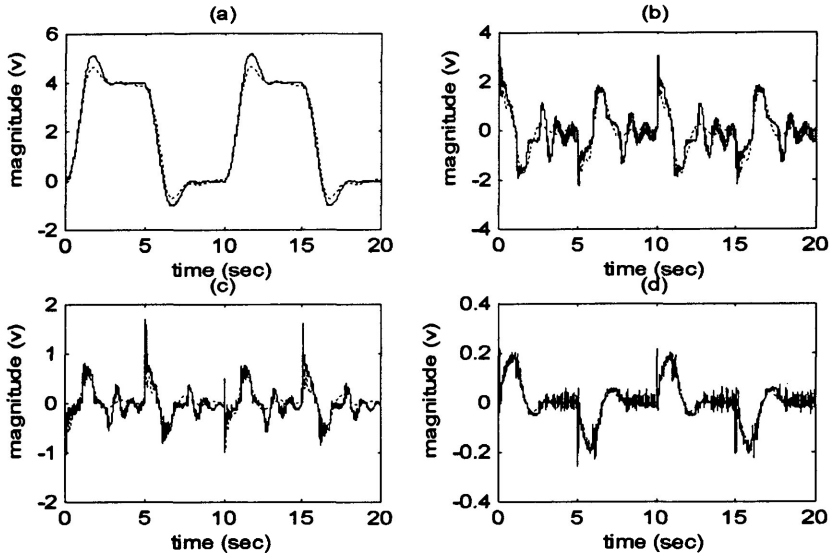

Figure 3-17. The SFV results of the updated reduced-model (Ac11r_10) by retaining modes [11/12,19/20,21/22,23/24,25,26] according to the MRM ranking.

The new procedure of model reduction and updating proposed in this study gives users a freedom to force an unstable identified model to be stable. This is done by moving the eigenvalue of an unstable mode into the unit circle. Afterward, the same procedure is applied to this forced stable model.

In the third example, the initial identified model has an unstable mode $\lambda_{17} = 1.0000235$. Before model reduction and updating for this unstable model, the unstable mode was forced to be $\lambda_{17} = 0.9999$. Then, the proposed procedure was applied. Figures 18 to 27 show the DMV and SFV results for each stage. The errors and ranking of the MRM and MSV are recorded in the Tables 3-3a and 3-3b, respectively.

Table 3-3a. The MRM and MSV ranking for the 3rd example				
Model Ac11_21u (300g payload unstable)				
mode number	frequency (Hz)	damping ratio	MRM ranking	MSV ranking
1/2	58.71	0.001	7	2
3/4	51.12	0.001	8	3
5/6	47.54	0.001	11	4
7/8	40.77	0.01	10	9
9/10	22.97	0.04	4	5
11/12	11.84	0.11	3	8
13/14	8.39	0.02	6	6
15/16	3.19	0.18	5	11
17/18	0.63	0.58	1	7
19/20	0.92	0.10	9	11
21	----	real	2	1

Table 3-3b: The model (Ac3_21u) reduction and updating results for the 3rd example							
modes information	procedure stage	validation method	prediction error				
			δ_1	δ_2	δ_3	δ_4	$\bar{\delta}$
keep all modes as is.	Unstable	DMV	0.2536	0.4872	0.7043	0.2524	0.4244
force unstable mode $\lambda 17 = 1.0003$ to $\lambda 17 = 0.9999$	stablizing	DMV	0.2553	0.4857	0.7041	0.2519	0.4243
		SFV	0.1210	0.6666	0.6734	0.3778	0.4597
9/10,11/12,13/14,15/16,17/18,21	MRM	DMV	0.2555	0.5019	0.7301	0.2566	0.4360
1/2, 3/4, 5/6, 9/10, 13/14, 21	MSV	DMV	0.3501	0.8147	0.9933	0.9730	0.7827
5/6,9/10,11/12,15/16,17/18,21	MRMC	DMV	0.2554	0.5043	0.7767	0.2572	0.4484
from MRMC (Ac3ru_11)	Updated	DMV	0.0975	0.4623	0.7010	0.2527	0.3784
		SFV	0.0777	0.5987	0.6819	0.3439	0.4256

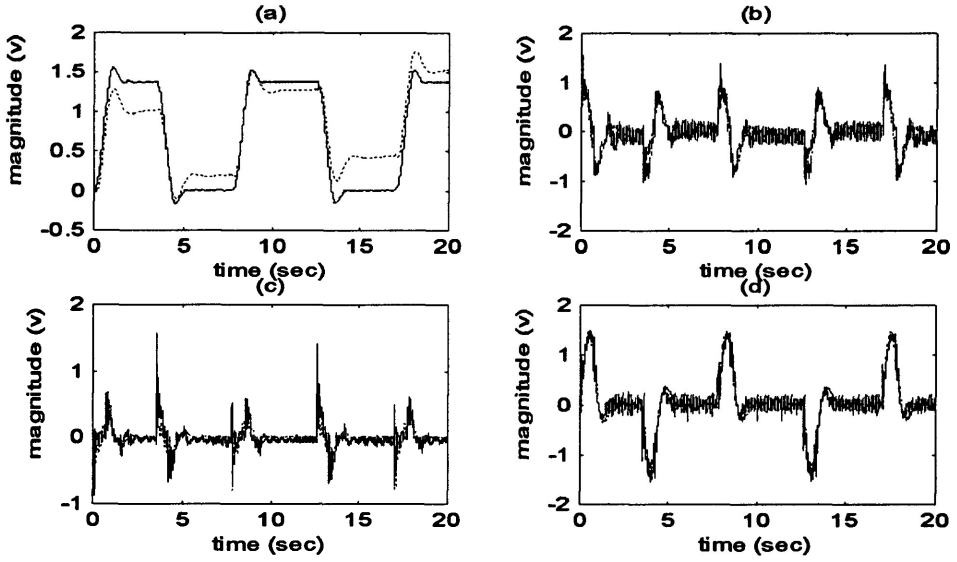

Figure 3-18. The DMV results of the initially unstable model (Ac3_21u) used for the third example.

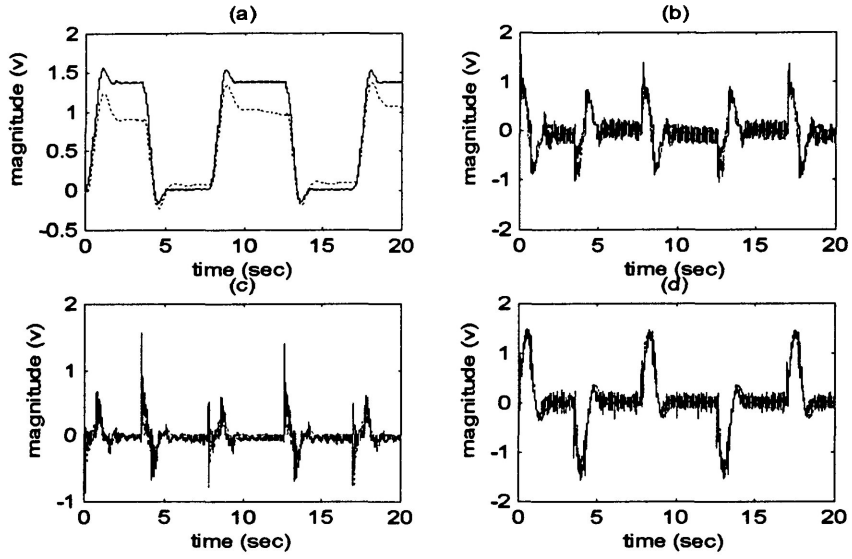

Figure 3-19. The DMV results of the forced stable model from the model (Ac3_21u).

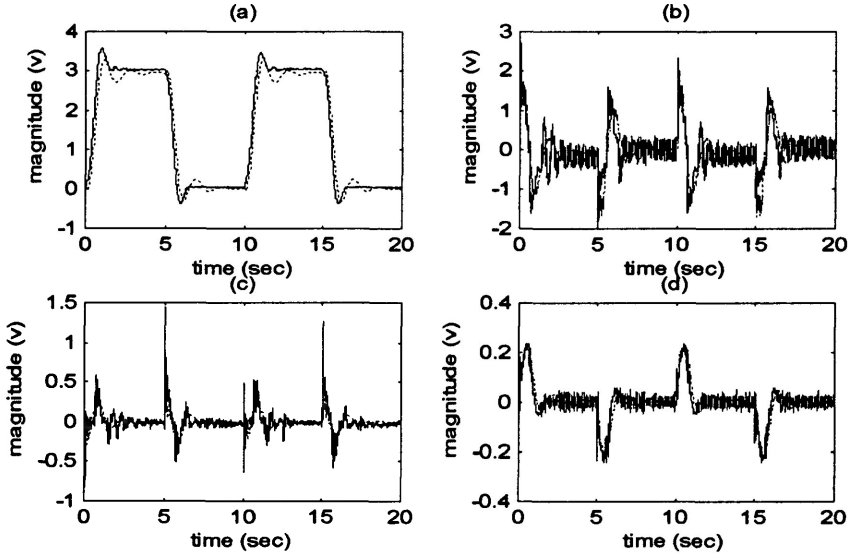

Figure 3-20. The SFV results of the forced stable model from the model (Ac3_21u).

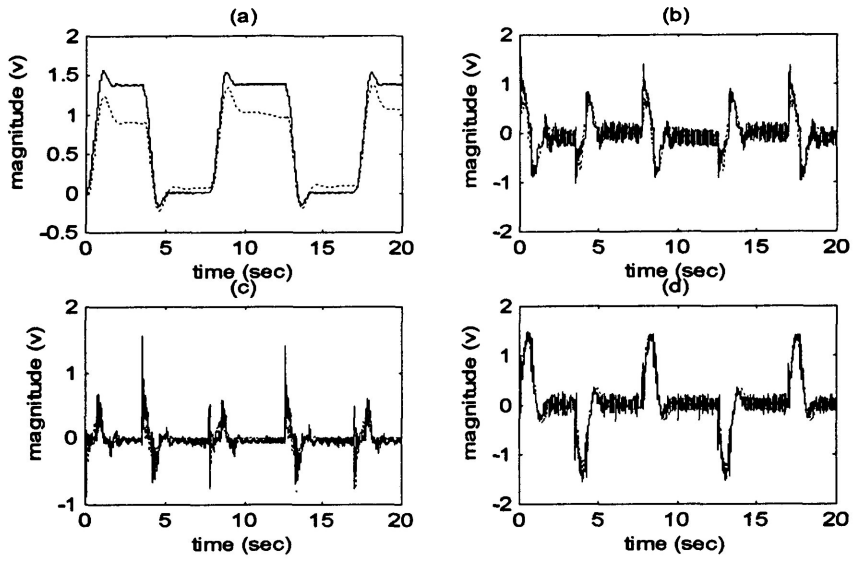

Figure 3-21. The DMV results of the reduced model obtained from the forced stable model by retaining modes [9/10,11/12,13/14,15/16,17/18,21] according the MRM ranking.

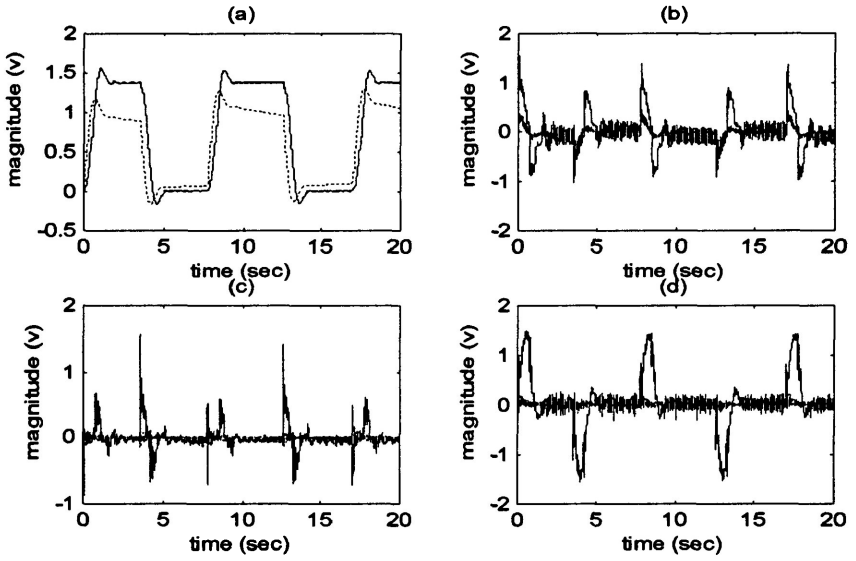

Figure 3-22. The DMV results of the reduced model obtained from the forced stable model by retaining modes [1/2,3/4,5/6,9/10,13/14,21] according to the MSV ranking.

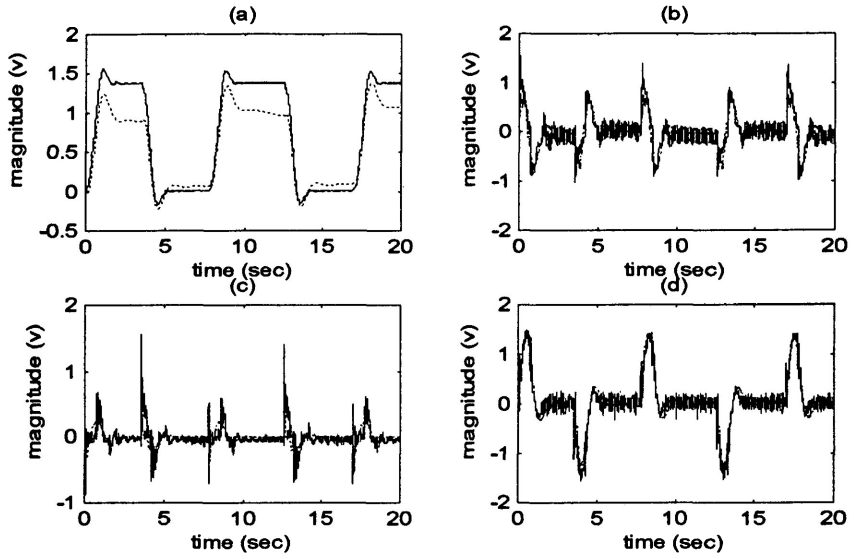

Figure 3-23. The DMV results of the reduced-model obtained from the forced stable model by retaining modes [5/6,9/10,11/12,15/16,17/18,21] according to the MRMC method.

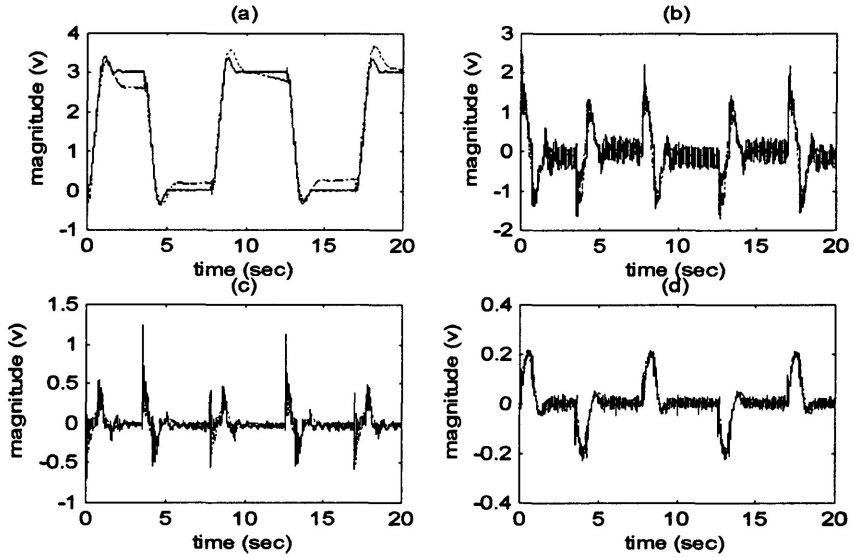

Figure 3-24. The DMV results of the updated reduced-model (Ac3ru_11) by retaining modes [5/6,9/10,11/12,15/16,17/18,21] according to the MRMC method.

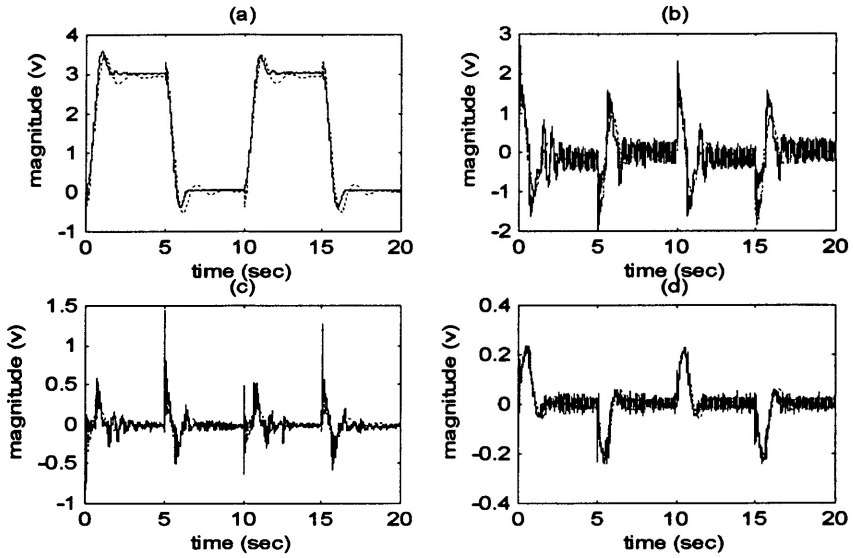

Figure 3-25. The SFV results of the updated reduced-model (Ac3ru_11) by retaining modes [5/6,9/10,11/12,15/16,17/18,21] according to the MRMC method.

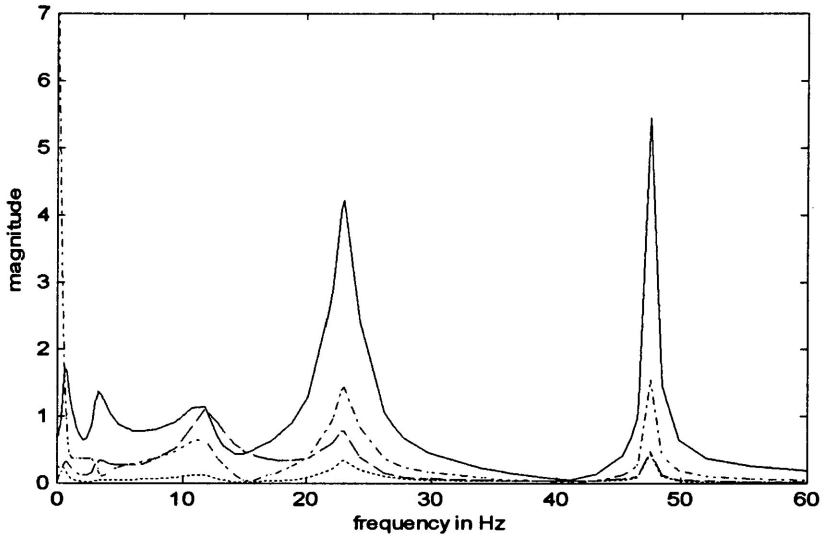

Figure 3-26. The frequency response of the updated reduced-model (Ac3ru_11) by retaining modes [5/6,9/10,11/12,15/16,17/18,21] according to the MRMC method.

The results for another two examples of model reduction and updating by applying the proposed procedure are recorded in the Tables 3-4a and 3-5a for their MRM and MSV rankings, and Tables 3-4b and 3-5b for the prediction errors.

Table 3-4a. The MRM and MSV ranking for an identified model derived from the open-loop experiments				
Model Ao2_19 (300g payload)				
mode number	frequency (Hz)	damping ratio	MRM ranking	MSV Ranking
1/2	46.14	0.01	11	7
3/4	23.19	0.04	8	4
5/6	18.54	0.07	5	5
7/8	14.99	0.08	7	9
9/10	9.84	0.05	6	3
11/12	8.06	0.18	2	6
13/14	7.48	0.01	10	10
15/16	1.98	0.22	9	11
17	---	Real	1	1
18	---	Real	3	2
19	---	Real	4	8

Table 3-5a. The MRM and MSV ranking for the identified model derived from the closed-loop experiments				
Model Ac11_18c (0g payload without removal of the Columb friction compensation)				
mode number	frequency (Hz)	damping ratio	MRM ranking	MSV ranking
1/2	41.76	0.02	10	9
3/4	23.17	0.04	5	3
5/6	19.87	0.03	4	2
7/8	10.46	0.04	7	7
9/10	8.00	0.03	8	5
11/12	5.32	0.08	3	4
13/14	0.96	0.08	9	10
15/16	0.67	0.22	6	8
17	---	Real	2	1
18	---	Real	1	6

Table 3-4b. The model (Ao2_19) reduction and updating results							
modes information	procedure stage	validation method	prediction error				
			δ_1	δ_2	δ_3	δ_4	$\bar{\delta}$
As is	Initial	DMV	0.0587	0.1833	0.3403	0.2503	0.1969
		SFV	0.2109	0.7690	0.9343	0.6319	0.6365
5/6,7/8,9/10,11/12,17,18,19	MRM	DMV	0.0605	0.2721	0.4949	0.2900	0.2794
1/2,3/4,5/6,9/10,11/12,17,18	MSV	DMV	0.4019	0.4409	0.4315	0.9071	0.5454
1/2,3/4,5/6,11/12,17,18,19	MRMC	DMV	0.0609	0.3602	0.5458	0.2805	0.3118
From MRMC method Final model---Ao2r_11	Updated	DMV	0.0279	0.1681	0.4120	0.1732	0.1953
		SFV	0.1768	0.7189	0.8163	0.6023	0.5786

Table 3-5b. The model (Ac11_18c) reduction and updating results							
modes information	procedure stage	validation method	prediction error				
			δ_1	δ_2	δ_3	δ_4	$\bar{\delta}$
As is	Initial	DMV	0.1711	0.4151	0.5814	0.3356	0.3758
		SFV	0.2111	0.6647	0.6959	0.5242	0.5240
3/4,5/6,7/8,11/12,15/16,17,18	MRM	DMV	0.1708	0.4184	0.6262	0.3331	0.3871
3/4,5/6,7/8,11/12,9/10,17,18	MSV	DMV	0.1755	0.5295	0.7275	0.3630	0.4488
1/2,3/4,7/8,11/12,15/16,17,8	MRMC	DMV	0.1707	0.4840	0.6227	0.3661	0.4109
From MRMC method Final model---Ac11r_12c.	Updatel	DMV	0.1547	0.4082	0.5324	0.2538	0.3373
		SFV	0.2365	0.6829	0.7403	0.5275	0.5468

3.3 Conclusions

1. The Modal Response Magnitude (MRM) is more reliable in quantifying the contribution of individual modes than the Mode Singular Value (MSV) for the system containing both rigid modes and flexible modes.

2. The proposed model updating scheme is very effective in improving the accuracy of a reduced-order model if this reduced-order model preserves the main modal information. In some cases, an updated model can even achieve a better accuracy than its initial model.

3. The proposed procedure of model reduction and updating can be applied to either stable model or unstable model. The experimental study has shown that the final updated model from a stable model usually has a better accuracy than that from an unstable model.

4. An advantage of the MRMC method is that the reduced-order model is guaranteed to preserve both the information of the rigid modes and flexible modes.

Table 3-6 lists the typical results of the model reduction and updating.

Table 3-6. The typical results of the updated reduced-order models

updated model code	Original model	Order & method	prediction error					
			validation	δ_1	δ_2	δ_3	δ_4	$\bar{\delta}$
Ao2r_11	Ao2_19 0g payload	11 MRMC	DMV	0.0279	0.1681	0.4120	0.1732	0.1953
			SFV	0.1768	0.7189	0.8163	0.6023	0.5786
Ao2r_7	Ao2_19 0g payload	7 MRMC	DMV	0.0283	0.1984	0.4518	0.2089	0.2218
			SFV	0.1773	0.7167	0.7994	0.6031	0.5741
Ao10r_9	Ao10r_12 0g payload	9 MRMC	DMV	0.1040	0.3710	0.6299	0.2907	0.3489
			SFV	0.2159	0.7845	0.9028	0.7332	0.6591
Ac3r_10	Ac3_18 0g payload	10 MRMC	DMV	0.0458	0.4456	0.6892	0.2298	0.3526
			SFV	0.0537	0.5542	0.6747	0.2910	0.3934
Ac3r_8	Ac3_18 0g payload	8 MRMC	DMV	0.0458	0.4551	0.6904	0.2307	0.3555
			SFV	0.0537	0.5520	0.6767	0.2906	0.3933
Ac5r_10	Ac5_22 200g payload	10 MRMC	DMV	0.0711	0.4918	0.5790	0.3344	0.3691
			SFV	0.0761	0.6452	0.6408	0.3237	0.4214
Ac6r_9	Ac6_29 200g payload	9 MRMC	DMV	0.0450	0.5242	0.5998	0.2712	0.3601
			SFV	0.0346	0.5391	0.5909	0.2594	0.3560
Ac11r_10	Ac11_26 300g payload	10 MRM	DMV	0.0414	0.4209	0.5291	0.2551	0.3116
			SFV	0.0749	0.4619	0.5222	0.2330	0.3230
Ac11r_8	Ac11_26	8 MRMC	DMV	0.0556	0.4952	0.6141	0.2731	0.3595
			SFV	0.0746	0.5073	0.5963	0.2578	0.3590
Ac14r_10	Ac14_32 400g payload	10 MRMC	DMV	0.0484	0.4933	0.5689	0.2513	0.3405
			SFV	0.0437	0.5114	0.5710	0.2474	0.3434
Ac3r_10c	Ac3_22c 0g payload	10 MRM	DMV	0.2477	0.3707	0.6495	0.2308	0.3747
			SFV	0.2297	0.7231	0.7557	0.5795	0.5720
Ac11r_8c	Ac11r_12c 300g payload	8 MRMC	DMV	0.0889	0.4380	0.5445	0.2584	0.3325
			SFV	0.2235	0.7002	0.7245	0.5039	0.5380

Chapter 4

Controller Design and Implementation

The last objective of this research is to design and implement an optimum controller that is robust when the manipulator carries different payloads. To this end, the first task is to select a proper model for the controller design. Section 1 reports how a nominal model is chosen from the models obtained in Chapter 2 and 3. Section 2 addresses controller design and considerations of controller robustness. Section 3 presents real-time implementation of the optimized controller and test results for the controller robustness. Finally section 4 gives the conclusions.

4.1 Selection of a Nominal Model for Controller Design

Three types of the updated reduced-order models were obtained in Chapter 2 and 3. They are:

Type I : the models derived from the data of the open-loop experiments.

Type II : the models derived from the data of the closed-loop experiments with the removal of the Coulomb friction compensation.

Type III : the models derived from the data of the closed-loop experiments without the removal of the Coulomb friction compensation.

To find a suitable model , the following model evaluation was conducted. Four models used in the evaluation are listed in Table 4-1. The first model is a type I model with an order of nine. The second and third models belong to type II and their orders are eight and ten, respectively. The fourth model is a type III model and its order is ten. Each model was used in a computer simulation of a closed-loop system with a Proportional (P) and Integral (I) controller shown in Figure 4-1.

Table 4-1: The optimization results of the model evaluation

model		search setting	optimization results				
notation	type		J	Err	Tr(sec)	Kp	Ki
Ao2r_9 Bo2r_9 Co2r_9	I	Kp0 = 3e-1; KI0 = 1e-2; Kplb = 5e-3; Kpub = 2e+0; KIlb = 5e-6; KIub = 2e-1;	1.8663	9.8870e-4	0.47	1.1915	5.00e-6
Ac3r_8 Bc3r_8 Cc3r_8	II		0.4034	3.5015e-6	0.82	0.3998	1.78e-2
Ac3r_10 Bc3r_10 Cc3r_10	II		0.4034	4.5764e-3	0.81	0.3995	1.78e-2
Ac3r_10c Bc3r_10c Cc3r_10c	III		1.3753	3.1172e-4	0.44	1.2536	5.29e-2

Notes: designation
Kp0 and KI0 -- search starting point.
Err – steady-state error. Tr -- rising time.

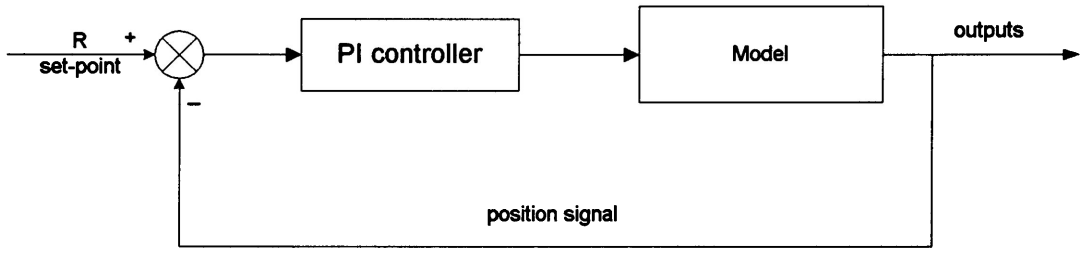

Figure 4-1. The closed-loop system used in the model evaluation

An optimum PI controller was designed for each model using the minimum integral of

time-multiplied absolute-error (ITAE) criterion in [28], i.e.,

$$\begin{aligned} \min_{K_P,\, K_I} J &= \Delta t \sum_{k=1}^{K_s} t(k)|R - \hat{y}_1(k)| \\ K_{Plb} &\leq K_P \leq K_{Pub} \\ K_{Ilb} &\leq K_I \leq K_{Iub} \end{aligned} \tag{4-1}$$

where K_P and K_I are the proportional gain and integral gain, respectively, R is the position reference, $\hat{y}_1(k)$ is the simulated angular position, $t(k)$ is the time at the kth sample moment, K_s is the number of the samples, Δt is the sampling time interval, and the sampling rate is 300 Hz. The lower and upper bounds for K_P are K_{Plb} and K_{Pub}, respectively. Similarly, the lower and upper bounds for K_l are K_{Ilb} and K_{Iub}, respectively. K_{Plb} and K_{Ilb} are given small values close to zero. K_{Pub} and K_{Iub} are determined by the controller saturation and closed-loop stability, respectively. The optimization results are listed in Table 4-1. It is seen that the type II models give the best results in terms of the minimum ITAE and steady state error.

The optimum PI controllers were implemented in real-time by a C code program. Figures 4-2 to 4-5 compare the simulated (dotted line) and implemented (solid line) results for arm commanded to 3v set-point.

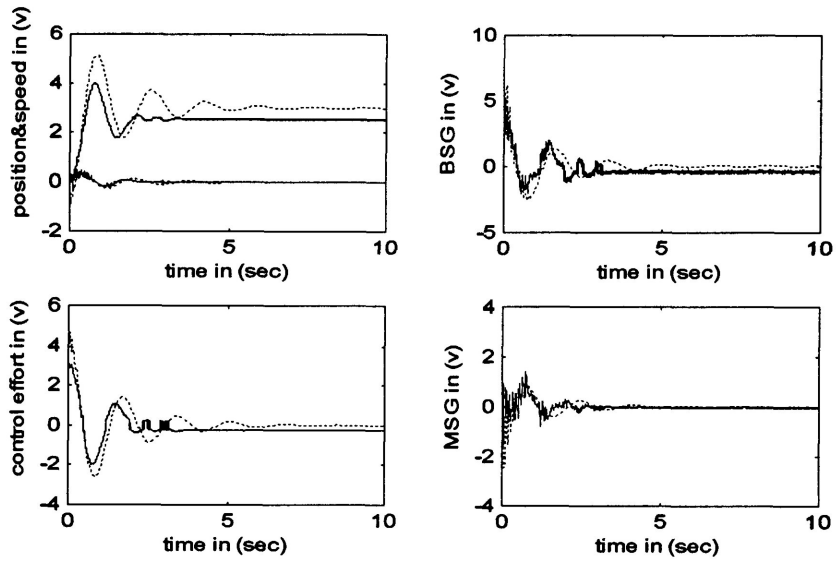

Figure 4-2: The comparison between the simulated and implemented results for the model Ao2r_9 with the optimal PI gain setting given in Table 4-1.

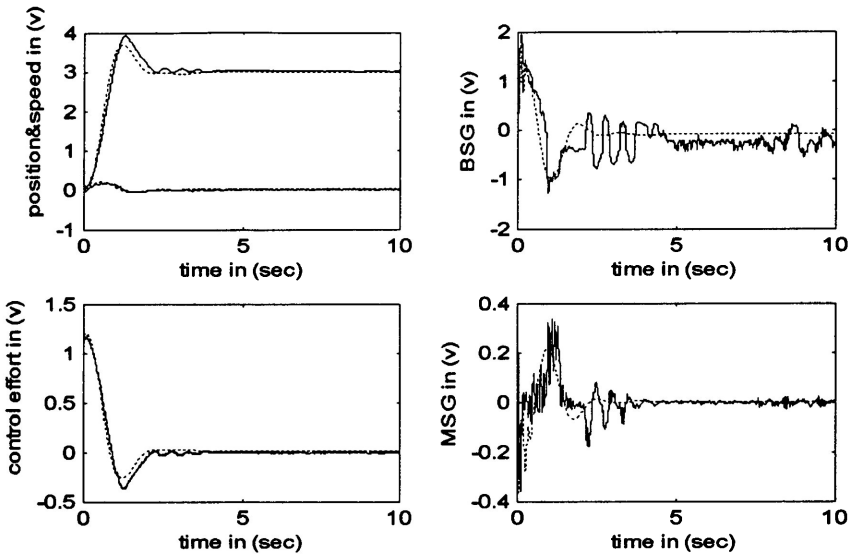

Figure 4-3: The comparison between the simulated and implemented results for the model Ac3r_8 with the optimal PI gain setting given in Table 4-1.

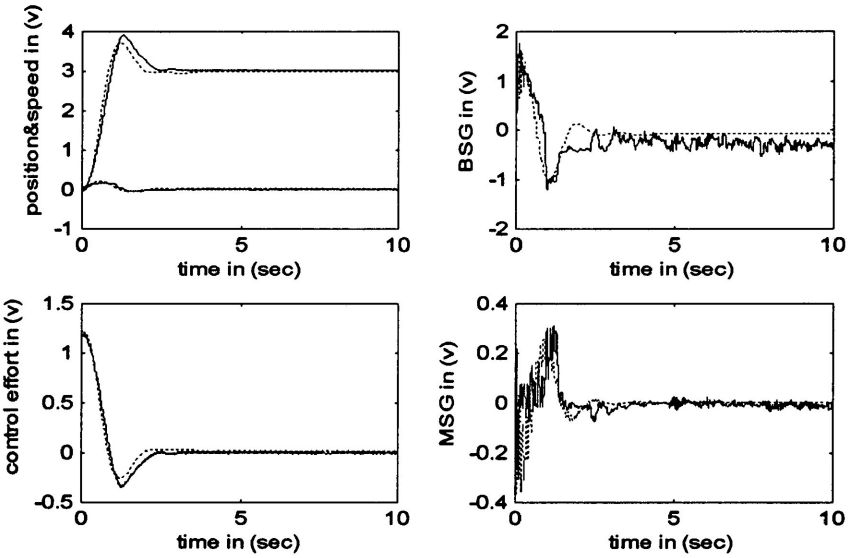

Figure 4-4: The comparison between the simulated and implemented results for the model Ac3r_10 with the optimal PI gain setting given in Table 4-1.

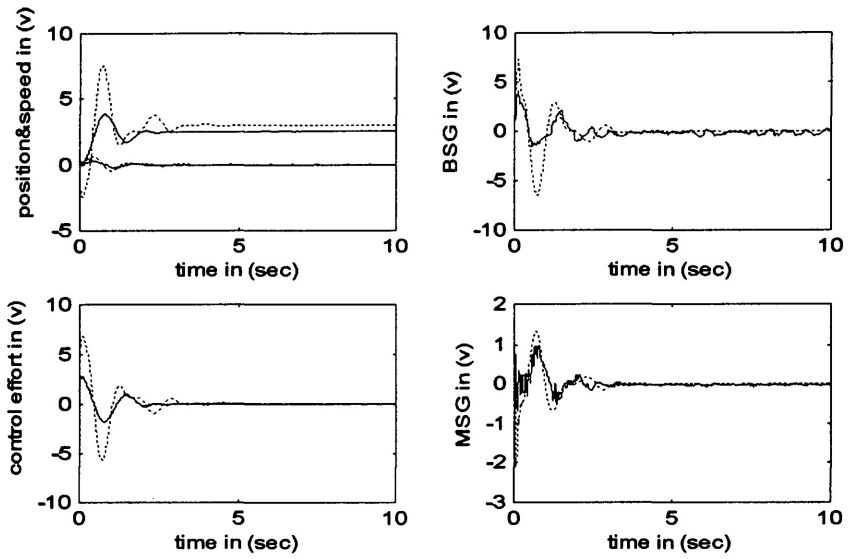

Figure 4-5: The comparison between the simulated and implemented results for the model Ac3r_10c with the optimal PI gain setting given in Table 4-1.

It can be seen that the controllers based on the type II models perform better than those based on the type I or III models; therefore, a set of type II model were selected as the nominal models in the following controller design. The realizations of the selected models are shown in Appendix B.

It is also noted that the optimum PI controller, i.e., K_P and K_I for both the second and third models are almost identical. Their simulated and implemented results are also similar. The third model has a higher order by including the third vibratory mode. The fact that the two models behave similarly indicates that the third vibratory mode has negligible presence in the responses and the model order can be reduced to eight.

4.2 PDPC Controller Design

The control goals are as follows:

1. Minimum tracking error in the angular position measured from the arm hub to a step reference input.

2. Minimum vibration of the arm.

3. Minimum performance deterioration when the payload changes or good robustness.

4. Sufficient stability margins.

The final controller structure chosen is shown in Figure 4-6.

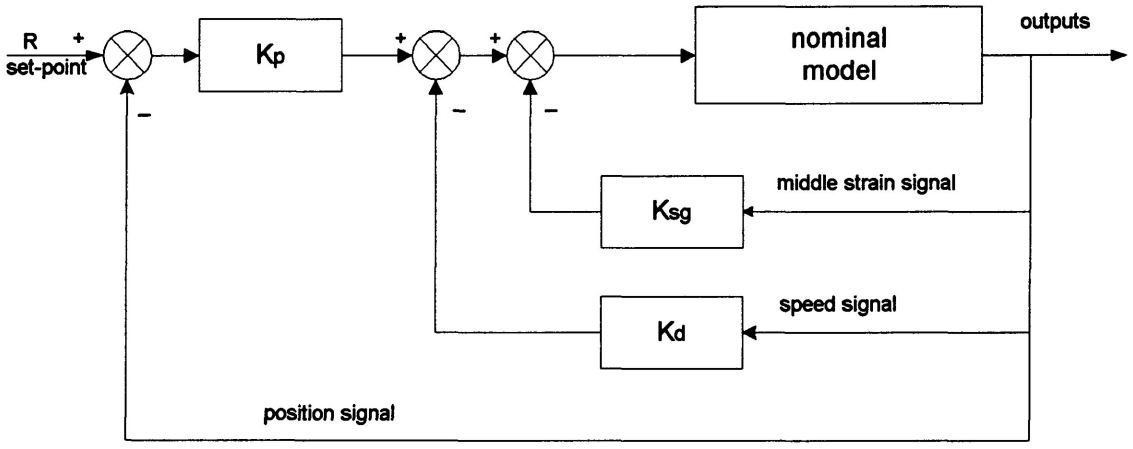

Figure 4-6. The PDP controller structure used in the controller optimization.

A proportional controller is used for the error signal of the angular position. The controller gain is denoted as K_P. A negative feedback of the angular speed serves as a derivative control of the angular position with a gain of K_d. In addition, a negative feedback of the middle strain gauge signal is used for suppressing the vibration of the flexible arm, and its controller gain is denoted as K_{sg}. The use of the middle strain gauge signal rather than the base strain gauge signal is based on the fact that the base strain gauge is more sensitive to the gear hitting (caused by backlash) than the middle strain gauge. The controller is named as PDP controller, and its block diagram is shown in Figure 4-7.

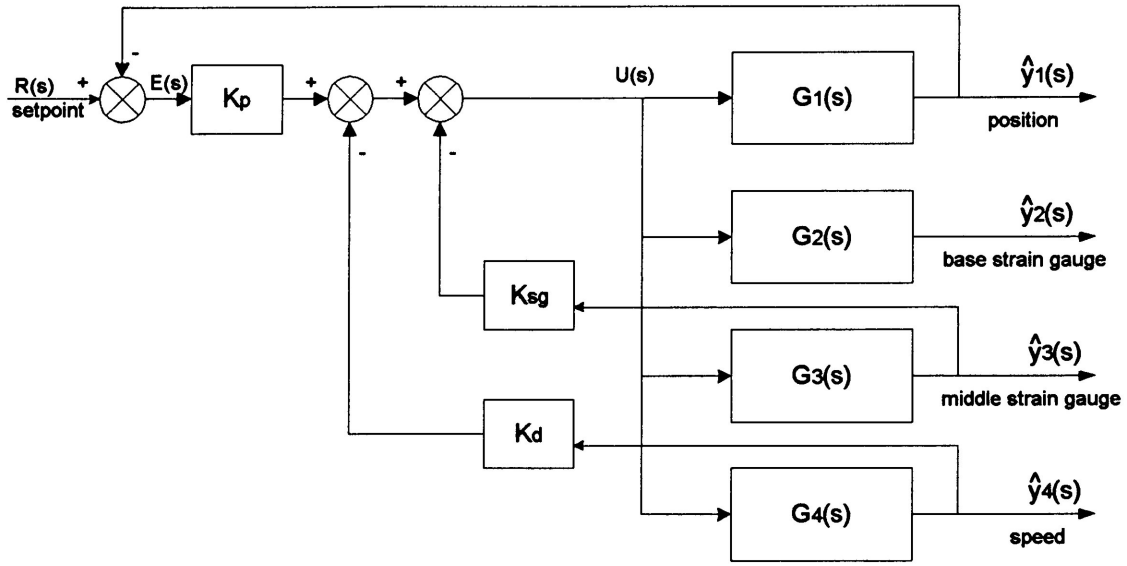

Figure 4-7. The schematic block diagram for the PDP controller.

For such a structure, the open-loop transfer function from the position error to the position signal can be found as follow:

$$G(s) = \frac{\hat{Y}_1(s)}{E(s)} = \frac{K_P G_1(s)}{1 + K_{sg} G_3(s) + K_d G_4(s)} \tag{4-2}$$

where $G_1(s)$, $G_3(s)$, and $G_4(s)$ are the transfer functions of the plant.

One of the main considerations is how to tune the controller such that its performance is insensitive to payload change. To understand the influence of the payload change on the system, a trial PDP controller with $K_P = 0.5$, $K_d = 3.3$, and $K_{sg} = 0.07$ is applied to the 0g payload model, 200g payload model, and 400g payload model, respectively. Figure 4-8 shows the comparison of the frequency responses computed from equation (4-2) for the three models with the same controller setting.

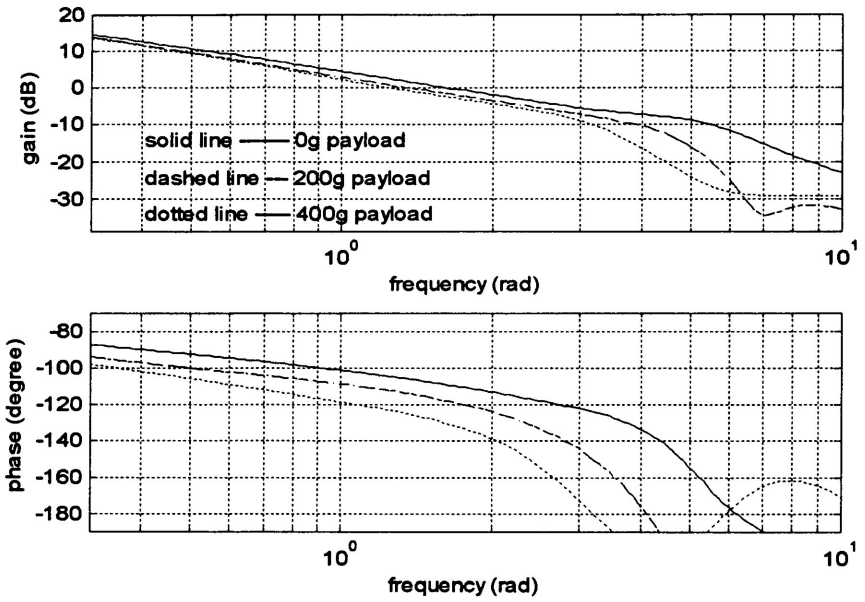

Figure 4-8. The frequency responses of the open-loop system defined by equation (4-2) for the models with the same PDP controller and different payloads.

It is seen that with an increase of the payload, the gain and phase margin are reduced; however, the phase margin is more sensitive to the payload change than the gain margin. It is also noted that the bandwidth of the system is reduced with an increase of the payload. Apparently, if the controller is tuned using a model with a particular payload, it may not perform well when it is applied to another model with a different payload. A technique that tunes a controller for different operating points was proposed in reference [29]. This technique was employed in this study. In addition, to have a sufficient stability, the gain margin and phase margin constraints are imposed [30]; therefore, the tuning optimization problem can be defined as following

$$\begin{aligned} \min_{K_p,\, K_d\,,\, K_{sg}} J &= W_E \sum_{i=1}^{3} E_i(K_p, K_d, K_{sg}) + W_{sg} \sum_{i=1}^{3} Y_i(K_p, K_d, K_{sg}), \\ GM_i &\geq 10\text{dB},\ PM_i \geq 55^\circ \text{ for } i = 1,2,3 \end{aligned} \tag{4-3}$$

where the subscripts $i = 1, 2, 3$ denote the 0g, 200g, and 400g payload models, respectively. W_E and W_{sg} are the weighting factors for user to choose according to the design emphasis. In the performance index of equation (4-3), E_i is the ITAE value of the normalized position error defined as

$$E_i(K_p, K_d, K_{sg}) = \Delta t \sum_{k=1}^{Ks} t(k)|R - \hat{y}_1(k)|/R \text{ , for } i = 1, 2, 3. \tag{4-4}$$

Y_i is the ITAE value of the normalized strain gauge signals defined as

$$Y_i(K_p, K_d, K_{sg}) = \Delta t \sum_{k=1}^{Ks} t(k)\left(\frac{|\hat{y}_2(k)|}{\max(|\hat{y}_2(k)|)} + \frac{|\hat{y}_3(k)|}{\max(|\hat{y}_3(k)|)}\right) \text{ , for } i = 1, 2, 3. \tag{4-5}$$

GM_i and PM_i are the gain margin and phase margin of the open-loop transfer function defined by equation (4-2).

The optimization used here must meet multiple objectives to guarantee the good tracking performance as well as the minimum vibration, and the imposed gain and phase margin constraints will provide the robustness of the system stability due to the uncertainties such as payload change. In this study, the minimization of the performance index in equation (4-3) was done using the Matlab function " CONSTR " in Optimization Toolbox [31 32].

Table 4-2. The optimization results of the gain settings for PDP controller

Initial point [Kp, Kd, Ksg]	weight		performance			Optimum gain settings		
	We	Wsg	J	ΣEi	ΣYi	Kp	Kd	Ksg
[0.3, 1.0, 0.1]	0.5	0.5	5.810	1.239	2.407	0.594	4.266	0.254
[0.594, 4.266, 0.254]	0.5	0.5	5.810	1.239	2.407	0.594	4.266	0.254
[0.8, 4.0, 0.5]	0.5	0.5	5.810	1.239	2.407	0.594	4.266	0.254

Search conditions: Lower bound = [0.005, 0.05, 0.005], Upper bound = [1.0, 15, 2];
Gain margin constraints, GMi ≥ 10dB, phase margin constraints, PMi ≥ 55°.

As shown in Table 4-2, with $W_E = W_{sg} = 0.5$, the optimization result of the gain setting converges to the same point ($K_p = 0.5935, K_d = 4.2664, K_{sg} = 0.2538$) for the different initial search points. This indicates that this set of the gain setting is the global optimization, and it will be applied to the real-time implementation in the next section.

4.3 PDPC Controller Implementation

As shown in chapter 2, the Coulomb friction compensation must be included in order to have a zero tracking error. The controller designed in the previous section is based on the linear model, and the Coulomb friction was not considered. The Coulomb friction must be compensated in the implementation of the controller. As observed in the closed-loop experiments, the Coulomb friction compensation added in the control effort is very effective for the rigid body to track the different set-points with the minimum error. But a disadvantage of doing this is to cause the small vibration by gear hitting after the angular position reaches its set-point. To overcome this problem, the Coulomb friction compensation is modified to be a conditional Coulomb friction compensation, i.e., after the set-point is reached, the compensation is removed. The final control structure implemented on the apparatus is named as PDPC controller as illustrated in Figure 4-9.

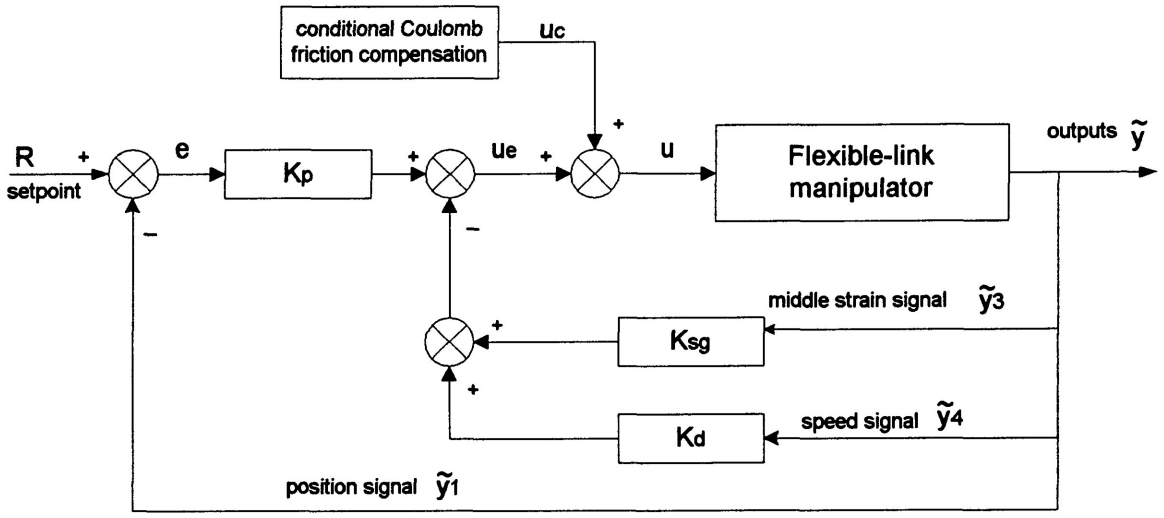

Figure 4-9: The PDPC controller structure.

The control law is given as follows:

$$u(k) = u_e(k) + u_c \tag{4-6}$$

where $u(k)$ is the system input, $u_e(k)$ is the control effort given by

$$u_e(k) = K_P[R - \tilde{y}_1(k)] - K_d \times \tilde{y}_4(k) - K_{sg} \times \tilde{y}_3(k), \tag{4-7}$$

and $u_c(k)$ is the conditional Coulomb friction compensation defined as

$$u_c = \begin{cases} 0.7 \text{ v for } u_e \geq 0, \text{ if } |R - \tilde{y}_1(k)| \geq 0.05 \text{ or } |\tilde{y}_4(k)| \geq 0.05 \\ -0.7 \text{ v for } u_e < 0, \text{ if } |R - \tilde{y}_1(k)| \geq 0.05 \text{ or } |\tilde{y}_4(k)| \geq 0.05 \\ 0.0 \text{ v otherwise.} \end{cases} \tag{4-8}$$

Figure 4-10 shows the base and middle strain gauges signals for the unconditional Coulomb friction compensation and the conditional Coulomb friction compensation.

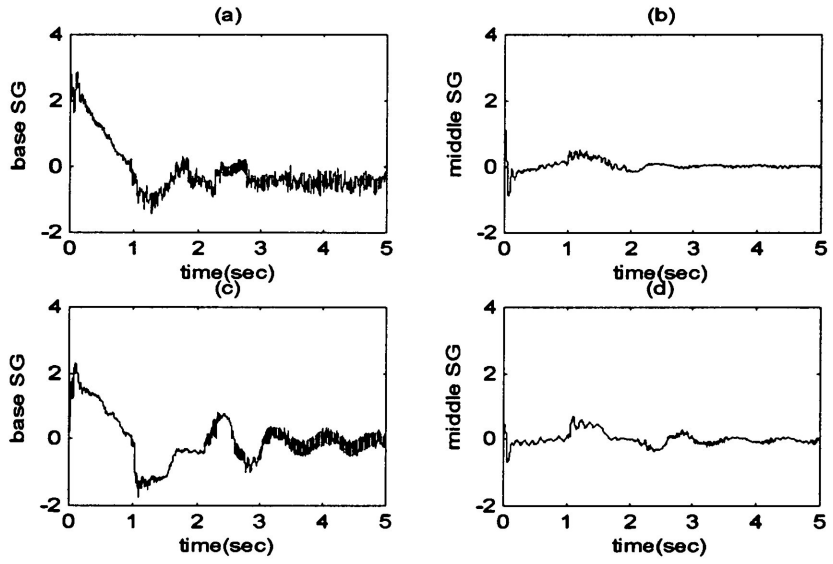

Figure 4-10: The comparison of the strain gauge signals between the conditional Coulomb friction compensation and unconditional Coulomb friction compensation. (a) and (b) conditional; (c) and (d) unconditional.

It can be seen that with the conditional Coulomb friction compensation, the vibration of the arm can be suppressed well.

It is worth emphasising that the conditional Coulomb friction compensation of the PDPC controller is the key point to achieve both the zero tracking error for the different set-points and minimum vibration after the set-point is reached.

The final PDPC controller is implemented in C language under the environment of Lab-Windows/CVI. The samples of the control results for the varying set-points as well as different payloads are illustrated in Figures 4-11.

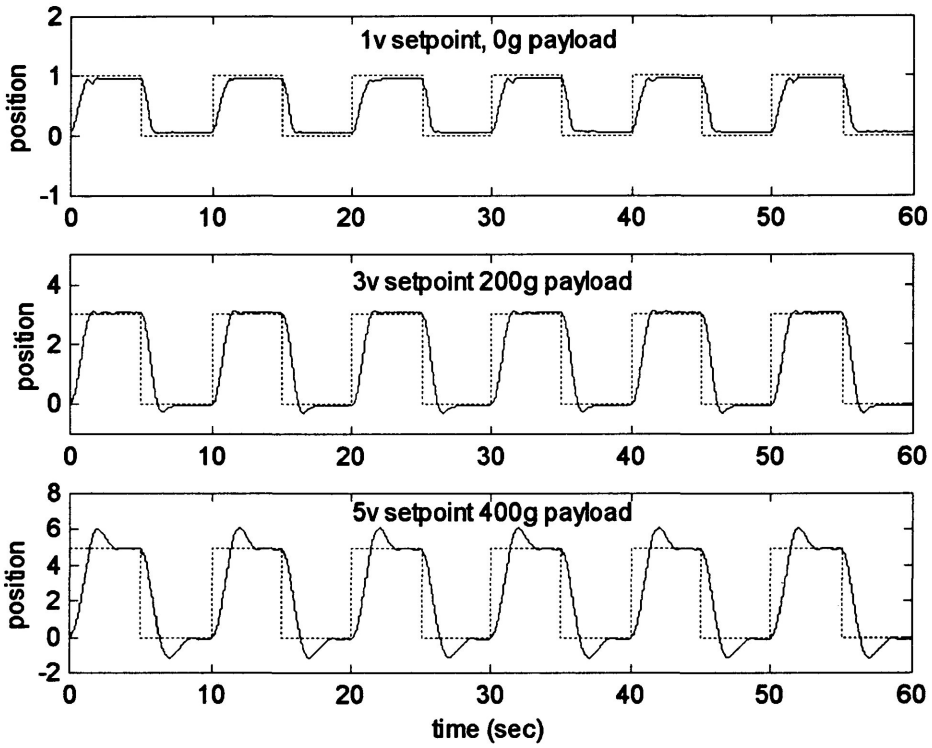

Figure 4-11. The comparison of the control results for different payloads and set-points.

Clearly, the results show that the controller is quite robust for the payload change, and also has a satisfactory tracking for the different set-points.

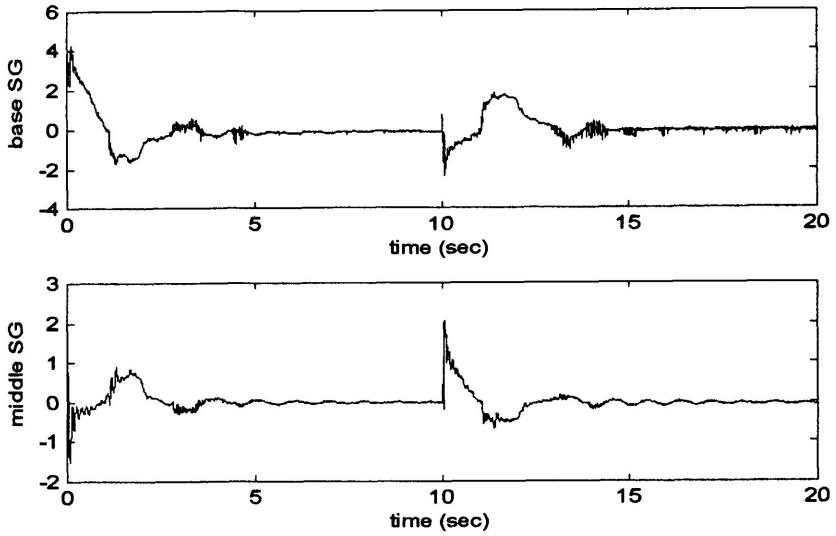

Figure 4-12. The strain gauge signals when the arm carried 400g payload and was commanded to follow a 5v square-waveform with a period of 20 seconds.

Figure 4-12 shows the suppression of the vibration for the worst case, in which the manipulator carried the 400g payload and commanded to a set-point of 5v square-waveform with 20 seconds period.

4.4 Preliminary Study of ILQR Control

Design techniques of control systems in state-space have been well developed. A state-space model is more suitable for controller design and implementation using state-space techniques. Linear Quadratic Regulator (LQR) technique is one of the most important results of modern control. It gives an optimal state feedback control gain K by minimizing the following performance index:

$$J = \frac{1}{2}\sum_{k=0}^{K}\left[x^T(k)Qx(k) + u^T(k)Ru(k)\right] \tag{4-9}$$

where Q and R are symmetric weighting matrices and nonnegative definite, which is most easily accomplished by picking the Q and R to be diagonal with all elements positive or zero. To im-

plement LQR control, a system observer is often needed as in most cases not all system states can be measured. In addition, to guarantee the zero steady-state error for the system with disturbance, an integral control must be added into control structure. The final control structure shown in Figure 4-13, named Integral Control plus LQR (ILQR) controller, is employed for controlling the flexible-link manipulator.

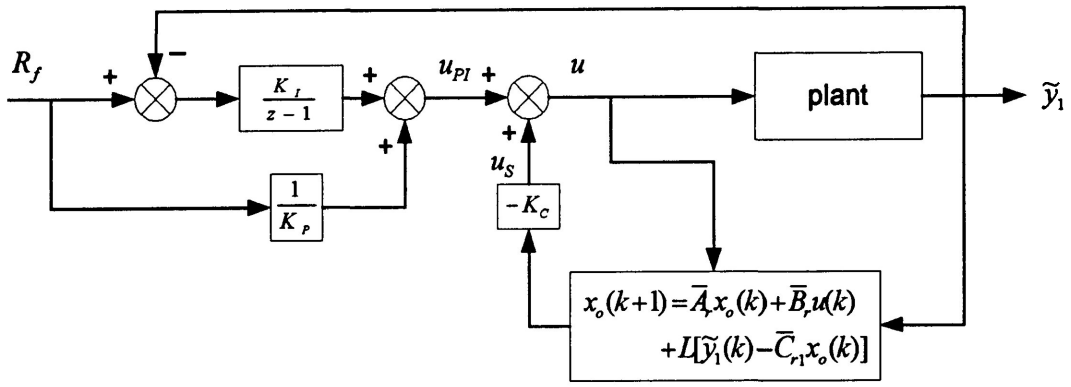

Figure 4-13. The control structure diagram of the ILQR controller.

In Figure 4-13, K_C is state feedback control gain, L is observer gain, K_P is steady-state plant gain from R_f to $\tilde{y}_1$ with the state feedback loop closed, K_I is integral gain, x_o is observed states, and $\bar{A}_r$, $\bar{B}_r$, and $\bar{C}_r$ are the updated reduced-order state-space realization where $\bar{C}_{r1}$ is the first row vector of $\bar{C}_r$, i.e., $\bar{C}_{r1} = [1\ 0\ 0\ 0]\ \bar{C}_r$. The reason to use the position signal only instead of using all measured signals is based on the fact that the system is observable with $\bar{A}_r$ and $\bar{C}_{r1}$. The model used in controller design was identified from the closed-loop experiments with 300g payload, and the model order is 8. The determination of the gains K_C, L, K_P, and K_I are explained below:

1. A proper selection of Q and R is critical in designing the state feedback control gain K_C by the LQR technique. Through computer simulation, it was noted that the first state corresponds to the position, the second and third states correspond to the strain gauge signals. Therefore, it is natural to put more weighting on the first three states as they are the control objectives, especially the first state. Another consideration is to keep the control effort u below 5A due to the system limit. By trial-and-error the values of the

diagonal elements of Q and the value of R were varied to ensure a satisfactory system performance with the LQR controller. Eventually the state feedback control gain K_C was found to be

$$K_C = \begin{bmatrix} 0.4229 & -0.1630 & -0.4117 & 0.4010 & 0.0061 & -0.1487 & -0.0164 & -0.1240 \end{bmatrix}$$

with

$$Q = \text{diag}\begin{bmatrix} 2 & 0.4 & 0.4 & 0.1 & 0.04 & 0.04 & 0.04 & 0.04 \end{bmatrix} \text{ and } R = 10.$$

2. The observer gain L was designed according to state-space dual property, i.e., L equals the transpose of the state feedback gain found by LQR algorithm using A^T and C_{r1}^T as system transition matrix and input matrix, respectively. The corresponding Q and R are selected to ensure observer responses at least 2 time faster than the state responses of full states feedback controlled plant. The final observer gain L was found to be

$$L = \begin{bmatrix} 0.8392 & 0.0688 & -0.6061 & 0.1406 & -0.0663 & 0.1148 & 0.0981 & -0.0099 \end{bmatrix}^T$$

with

$$Q = \text{diag}\begin{bmatrix} 1 & 1 & 1 & 1 & 1 & 1 & 1 & 1 \end{bmatrix} \text{ and } R = 1.$$

3. After K_C and L were found, K_P was determined by applying a 1v step input as R_f and recording the steady-state value of $\hat{y}_1$ with $K_P = 1$, $K_I = 0$, and $d = 0$ in Figure 4-14, hence,

$$K_P = \frac{R_f}{\hat{y}_1(\infty)} = \frac{1}{\hat{y}_1(\infty)} = 0.7746.$$

4. Finally, $K_I = 0.0015$ was determined by trial-and-error for a satisfactory system performance with respect to a disturbance d shown in Figure 4-14 as it simulates the Coulomb friction.

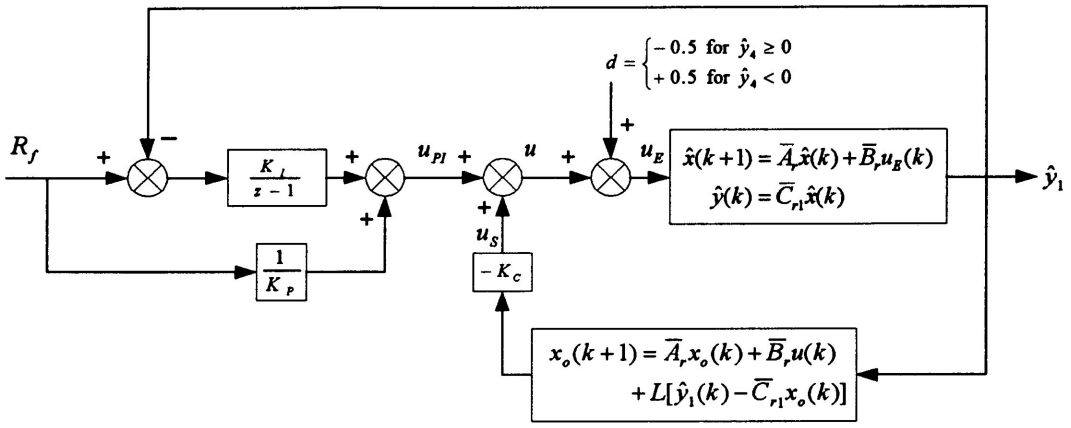

Figure 4-14. The schematic diagram of the computer simulation.

With the above gain settings, the simulations with set-points of 3v and 5v were first conducted according to the system schematic diagram in Figure 4-14. Then, the ILQR controller was implemented in real-time by a C code program. The comparisons of the system performances between the simulation and the implementation are shown in Figures 4-15 to 4-18.

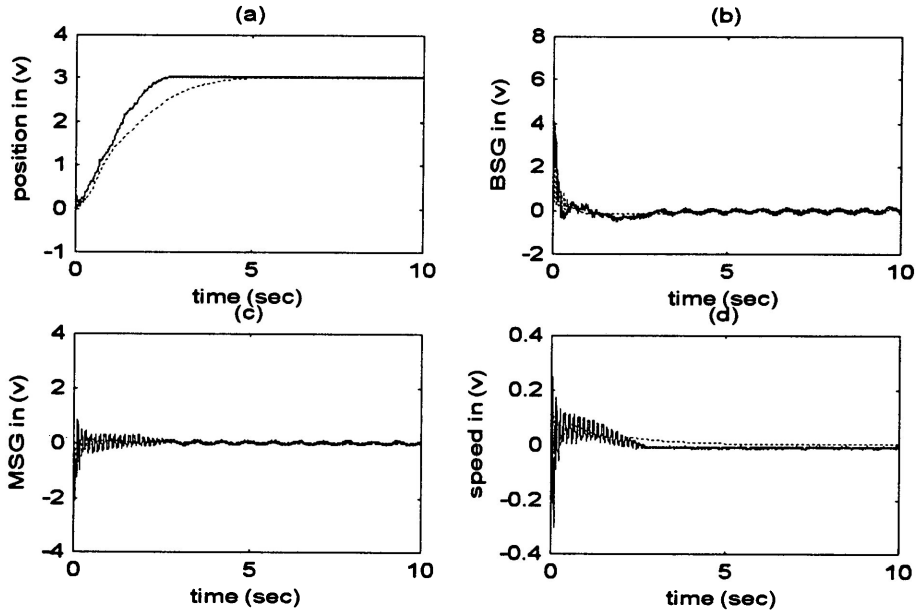

Figure 4-15. Comparison of system responses between the simulation and the implementation for the manipulator carrying 300g payload commanded to 3v position set-point.

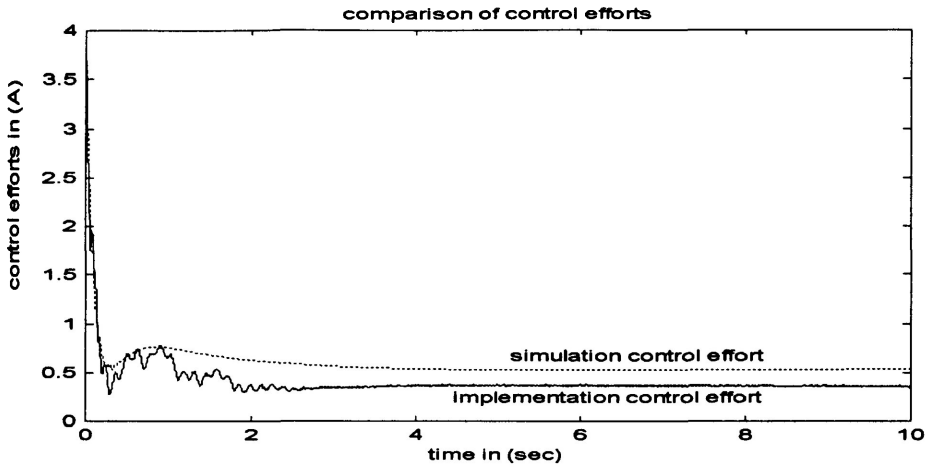

Figure 4-16. Comparison of control efforts between the simulation and the implementation corresponding to the system responses in Figure 4-15.

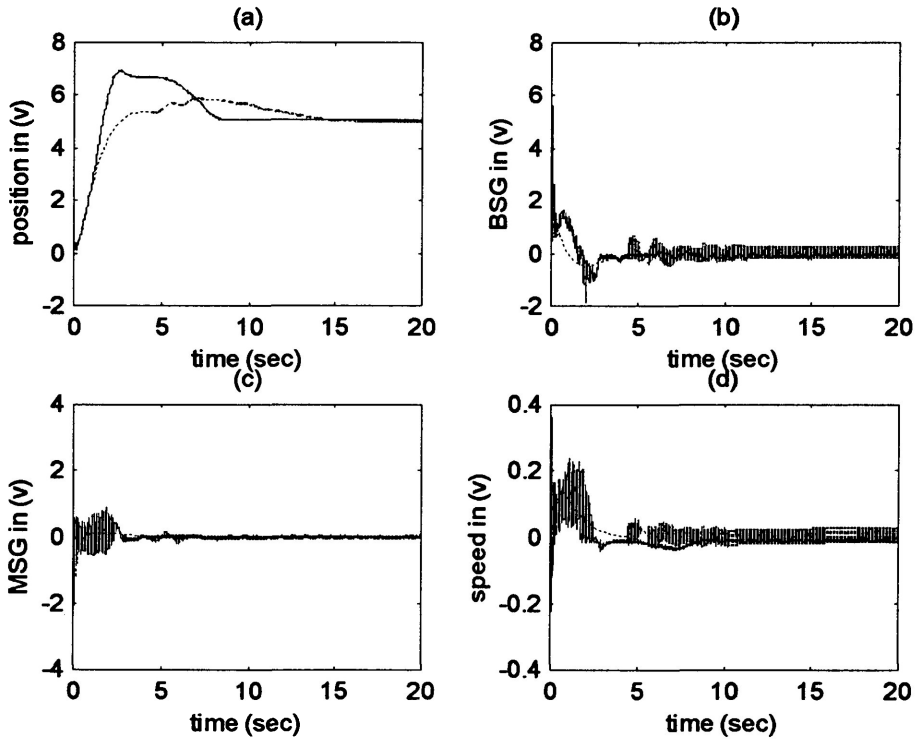

Figure 4-17. Comparison of system responses between the simulation and the implementation for the manipulator carrying 300g payload commanded to 5v position set-point.

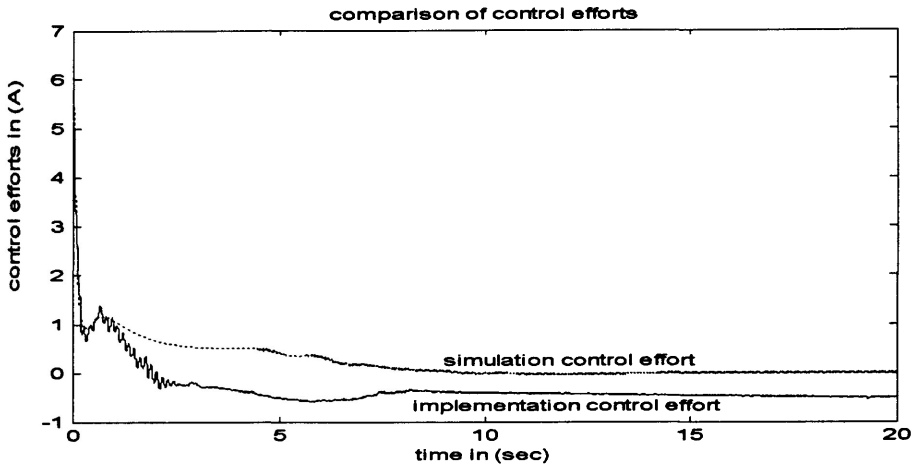

Figure 4-18. Comparison of control efforts between the simulation and the implementation corresponding to the system responses in Figure 4-17.

Following are the observations and analysis from the experimental results:

1. As shown in Figure 4-15, with the same ILQR controller, the real system and identified system model behave similarly in the case of 3v set-point. The performance is acceptable in term of the tracking accuracy and vibration. It is due to the Coulomb friction (the main disturbance in system) can be approximately modeled as a constant disturbance as the arm position did not overshoot and the speed did not change its direction. In such a case, the ILQR controller indeed has a capability of handling a constant disturbance.

2. For the case of 5v set-point, the implementation results differ from the simulation results. It is noted that an oscillation or limit cycle phenomenon existed. It can be seen that the position was overshot and speed reversed its direction. This fact indicated that the Coulomb friction was no longer a constant disturbance but varied its direction according to the speed. Although the integral control action eventually brought the arm close to the set-point, all signals oscillated continuously. This clearly shows that the ILQR controller is incapable of handling a varying disturbance.

4.5 Conclusions

Based on the study, the following conclusions can be drawn:

1. The models derived from the data of the closed-loop experiments with the removal of the Coulomb friction compensation are closer to the real system than the other models.

2. Under the assumption of the stable system, the use of the abundant gain and phase margins are an effective way to achieve a good robustness of the system stability.

3. The Coulomb friction compensation must be incorporated in order to have a zero tracking error. The compensation should be conditional to avoid the vibration caused by the gear hitting.

4. Although the system performances with the ILQR controller are not as good as those with the PDPC controller, the ILQR controller has its own advantages such as it needs only one position sensor and the feedback signal has a higher signal-to-noise ratio.

Chapter 5

Summary and Future Work

- The contributions of the study:

  1. The study has addressed several important issues such as the methods to excite the system, types of exciting signals, and model validation in the system identification. The experimental results show that the noises and nonlinearity could significantly reduce the accuracy of the identified model by the ORSE algorithm. To reduce the nonlinear influence for the system under study, the closed-loop experiment with the Coulomb friction compensation should be used for data acquisitions. The study has also successfully implemented several data preprocessing operations in order to effectively apply the ORSE algorithm to the system under study.

  2. A new model reduction procedure has been developed. This new procedure can be applied to either stable or unstable models. It also allows to incorporate any prior model information in decision making. A new index referred to as modal response magnitude (MRM) has been proposed to quantify the contribution of individual modes. The experimental study has shown that the MRM is more reliable in quantifying the contribution of individual modes than the mode singular value (MSV) for the system containing both rigid modes and flexible modes. A new model updating scheme has been proposed. The experimental study has indicated that if a reduced-order model preserves the main modal information, the proposed updating scheme can effectively improve the accuracy of the reduced-order model.

3. The experimental results show that the use of the abundant gain and phase margins is an effective way to achieve a good robustness of the system stability. In order to have a zero tracking error, the Coulomb friction compensation must be incorporated. Moreover, the compensation should be conditional to avoid the vibration caused by the gear hitting after the arm reaches its set-point.

- The study can be furthered in the following areas:

1. An adaptive control in the form of gain scheduling should be tried to obtain the best performance for each payload if an effective method can be found to detect the payload on-line fast and accuracy enough.
2. An effective control strategy to reduce the gear hitting deserves a further investigation.
3. Analytical proof of the MRM index is needed.

Bibliography

[1] T. J. Tarn, A. K. Bejczy, and X. Ding, " On the Modelling of Flexible Robot Arms ", *Technical Report SSM-RL-88-11* (1998), Washington University, (Robotics Laboratory Report), pp.1145-1150.

[2] A. P. Tzes and S. Yurkovich, " Application and Comparison of On-line Identification Methods for Flexible Manipulator Control ", *The International Journal of Robotics Research* (1991), 10(5), pp.515-527.

[3] R. H. Cannon and E. Schmitz, " Initial Experiments on the End-Point Control of a Flexible One-Link Robot ", *The International Journal of Robotics Research* (1984), 3(3), pp.62-75.

[4] J. Z. Sasiadek and R. Srinivasant, " Dynamic Modelling and Adaptive Control of a Single-link Flexible Manipulator ", *Proceedings of the AIAA Guidance, Navigation, and Control Conference* (1988), Minneapolis, MN., pp.848-844.

[5] A. Jnifene, " Active Vibration Control of a Single-link Flexible Manipulator : An Experimental Investigation ", *Proceedings of the 17th Canadian Congress of Applied Mechanics* (1999), Hamilton, ON., pp.357-358.

[6] P. T. Kotnlk, S. Yurkovich and Ü. Özgüner, " Acceleration Feedback for Control of a Flexible Manipulator Arm ", *Journal of Robotic Systems* (1988), 5(3), pp.181-196.

[7] H. Geniele, R. V. Patel, and K. Khorasani, " End-Point Control of a Flexible-link Manipulator : Theory and Experiments ", *IEEE Transactions on Control Systems Technology* (1997), 5(6), pp.556-570.

[8] S. Yurkovich and F. E. Pacheco, " On Controller Tuning for a Flexible-link Manipulator with Varying Payload ", *Journal of Robotic Systems* (1989), 6(3), pp. 233-254.

[9] W.T. Qian and C. C. H. Ma, " A New Controller Design for a Flexible One Link Manipulator ", *IEEE Transactions on Automatic Control* (1997), 42(3), pp.132-137.

[10] R. N. Banavar and P. Dominic, " An LQG/H_∞ Controller for a Flexible Manipulator ", *IEEE Transaction on Control Systems Technology* (1995), 3(4), pp.409-416.

[11] D. M. Rovner and R. H. Cannon, " Experiments toward On-line Identification and Control of a very Flexible One-link Manipulator ", *The International Journal of Robotics Research* (1987), 6(4), pp.3-19.

[12] S. Yurkovich, F. E. Pacheco, and A. P. Tzes, " On-line Frequency Domain Information for Control of a Flexible-link robot with Varying Payload ", *IEEE Transactions on Automatic Control* (1989), 34(12), pp.1300-1304.

[13] S. Yurkovich, A. P. Tzes, I. Lee, and K. L. Jillsley, " Control and System Identification of a Two-link Flexible Manipulator ", *Proceedings of the IEEE International Conference on Robotics and Automation* (1990), Cincinnati, OH., pp.1626-1631.

[14] K. L. Hillsley and S. Yurkovich, " Vibration Control of a Two-link Flexible robot arm ", *Dynamics and Control* (1993), 3, pp.261-280.

[15] A. Fujimori, P. N. Nikiforuk and E. Koda, " Modelling of a Flexible Arm Using System Identification and Model Reduction ", *Journal of System and Control Engineering* (1995), 209, pp.13-20.

[16] S. Yu, " Control of Flexible-link Manipulator ", *Master's Thesis* (1997), Lakehead University, Thunder Bay, Canada.

[17] J-N. Juang and R. S. Pappa, " An Eigensystem Realization Algorithm for Modal Parameter Identification and Modal Reduction ", *Journal of Guidance*, (1985), 8(5), pp.620-627.

[18] J-N. Juang, " Applied System Identification ", 1994, Prentice Hall, Englewood Cliffs, New Jersey.

[19] J-S. Lew, J-N. Juang, and R.W. Longman, " Comparison of Several System Identification methods for Flexible Structures", *Journal of Sound and Vibration* (1993), 167(3), pp.461-480.

[20] K. Liu and D. W. Miller, " Time Domain State Space Identification of Structural System ", *Journal of Dynamic System, Measurement, and Control* (1995), 117, pp.608-618.

[21] R. S. Pappa and J-N. Juang, " Some Experience with the Eigensystem Realization Algorithm ", *Sound and Vibration* (1988), pp.30-34.

[22] H. M. Kim and H. H. Doiron, " On-orbit Modal Identification of Large Space Structures ", *Sound and Vibration* (1992), pp.24-30.

[23] R. S. Pappa, " Identification Challenges for Large Space Structures ", *Sound and Vibration* (1990), pp.16-21.

[24] S. Bernard, " Control of a Flexible Robotic Link Using LQR Control Algorithm ", *Degree Project* (1998), Lakehead University, Thunder Bay, Canada.

[25] T. Hong, R. J. Bauer, P.C. Hughes, K. A. Carroll and Vukovich, " Laboratory Results on 'Augmented' System Identification of Flexible Spacecraft with Nonlinearities ", *Canadian Aeronautics and Space Journal* (1997), 43(3), pp.169-175.

[26] B. Moore, " Principal Component Analysis in Linear Systems: Controllability, Observability, and Model Reduction ", *IEEE Transactions on Automatic Control* (1981), 26(1), pp.17-31.

[27] R. J. Bauer and P. C. Hughes, " Three Approaches to Balanced Order Reduction of Unstable Models ", *Proceedings of the SEM Annual Conference on Theoretical, Experimental and Computational Mechanics* (1999), Cincinnati, OH., pp.304-307.

[28] K. Ogata, " Modern Control Engineering ", 2nd edition, 1990, Prentice Hall, Englewood Cliffs, New Jersey.

[29] K. Natarajan and A.F. Gilbert, " On Direct PID Controller Tuning based on Finite Number of Frequency Response Data ", *ISA Transactions* (1997), 36(2), pp.139-149.

[30] K. Natarajan, A. F. Gilbert and A. Yousef, " PID Controller Tuning based on Frequency Response Data ", *Pulp & Paper Canada* (1998), 99(4), pp.59-63.

[31] M. J. D. Powell, " The Convergence of Variable Metric Methods for Nonlinear Constrained Optimization Calculations ", Nonlinear Programming 3, (O.L. Mangasarian, R.R. Meyer, and S.M. Robinson, eds.) Academic Press, 1978.

[32] Matlab User Guides of Optimization Toolbox.

[33] G. F. Franklin, J. D. Powell, and M. Workman, " Digital Control of Dynamic Systems", 3rd Edition, 1998, Addison Wesley Longman, Inc.

[34] K. Liu, " Modal Parameter Estimation Using the State-space Method ", *Journal of Sound and Vibration* (1996), 197(4), pp.387-402.

[35] K. Liu, " Mathematical Model of a Single-link Flexible Manipulator ", *Study notes.*

[36] B-S. Chen and Y-M. Cheng, " A Structure-Specified H^{∞} Optimal Control Design for Practical Applications: A Genetic Approach ", *IEEE Transactions on Control Systems Technology* (1998), 6(6), pp.707-717.

[37] C. W. Canudas, H. Olsson, K. J. Astrom, and P. Lischinsky, " A New Model for Control of Systems with Friction ", *IEEE Transactions on Automatic Control* (1995), 40(3), pp.419-425.

Appendix

A: The Data Tables

Table A-1. The data list for the open-loop experiments

data code	datafile	length	sampling rate	current waveform	max. magnitude
O_dat1	So_sm1	3000	300 Hz	square	1v
O_dat2	So_sm2L	6000	300 Hz	square	2v
O_dat3	So_sh1	5000	500 Hz	square	1v
O_dat4	So_sh2	5000	500 Hz	square	2v
O_dat5	So_prm1	3000	300 Hz	periodic random	1v
O_dat6	So_prm2L	6000	300 Hz	periodic random	2v
O_dat7	So_prh1	5000	500 Hz	periodic random	1v
O_dat8	So_prh2	5000	500 Hz	periodic random	2v
O_dat9	So_pbm1	3000	300 Hz	varying square	1v
O_dat10	So_pbm2	3000	300 Hz	varying square	2v
O_dat11	So_pbh1	5000	500 Hz	varying square	1v
O_dat12	So_pbh2	5000	500 Hz	varying square	2v
O_dat13	So_rm2	3000	300 Hz	random	2v
O_dat14	So_rh2	5000	500 Hz	random	2v

Table A-2. The data list for the bounded open-loop experiments

data code	datafile	length	sampling rate	current magnitude	max. magnitude
B_dat1	Sb_rm2	12000	300 Hz	random	2v
B_dat2	Sb_rm3	12000	300 Hz	random	3v
B_dat3	Sb_rm4	12000	300 Hz	random	4v
B_dat4	Sb_rh2	12000	500 Hz	random	2v
B_dat5	Sb_rh3	12000	500 Hz	random	3v
B_dat6	Sb_rh4	12000	500 Hz	random	4v
B_dat7	Sb_sm1	12000	300 Hz	constant	1v
B_dat8	Sb_sm2	12000	300 Hz	constant	2v
B_dat9	Sb_sm3	12000	300 Hz	constant	3v
B_dat10	Sb_sh1	12000	500 Hz	constant	1v
B_dat11	Sb_sh2	12000	500 Hz	constant	2v
B_dat12	Sb_sh3	12000	500 Hz	constant	3v

Table A-3. The data list for the closed-loop experiments						
data code	datafile	gain setting	load	length	ref. & Coulomb compensation	
C_dat1	Srl0_pd1	p=1 d=2.8	0g	9600	R=2v/8s,	c=0.8v
C_dat2	Srl0_pd2	p=1 d=2.8	0g	12000	R=3v/10s,	c=0.9v
C_dat3	Srl0_vc2	P=1 d=2.8	0g	12000	R=3v/2.5-5s,	c=0.7v
C_dat4	Srl0_vc1	p=1 d=2.8	0g	12000	R=2v/2-4s,	c=0.9v
C_dat5	Srl1_pd1	p=1 d=2.8	200g	9600	R=2v/8s,	c=0.9v
C_dat6	Srl1_pd2	p=1 d=2.8	200g	12000	R=3v/10s,	c=0.9v
C_dat7	Srl2_pd	p=0.8 d=2.8	300g	12000	R=3v/10s,	c=1.0v
C_dat8	Srl2_pd1	p=0.6 d=2.8	300g	12000	R=2v/10s,	c=1.0v
C_dat9	Srl2_pd2	p=1 d=2.8	300g	12000	R=4v/10s,	c=1.0v
C_dat10	Srl2_pd3	p=1 d=2.8	300g	9600	R=3v/8s,	c=0.8v
C_dat11	Srl2_pd4	p=1 d=2.8	300g	12000	R=3v/10s,	c=0.8v
C_dat12	Srl2_pd5	p=1 d=2.8	300g	9600	R=2v/8s,	c=0.8v
C_dat13	Srl3_pd1	p=1 d=2.8	400g	12000	R=2v/10s,	c=0.9v
C_dat14	Srl3_pd2	p=1 d=2.8	400g	12000	R=3v/10s,	c=0.9v

Table A-4. The data list of the real-time control			
data code	datafile	purpose	Controller & setting
R_dat1	rc_pi1	Ac3r_10 evaluation	PI with optimal gains
R_dat2	rc_pi2	Ac3r_8 evaluation	PI with optimal gains
R_dat3	rc_pi5	Ao2r_9 evaluation	PI with optimal gains
R_dat4	rc_pi7	Ac3r_10c evaluation	PI with optimal gains
R_dat5	rc_pdpVs	400g/5v vibration control effect	PDPC with optimal gains
R_dat6	rc_pdpL0	0g/1v controller performance	PDPC with optimal gains
R_dat7	rc_pdpL1	200g/3v controller performance	PDPC with optimal gains
R_dat8	rc_pdpL3	400g/5v controller performance	PDPC with optimal gains
R_dat9	rc_ilqr1	300g/3v controller performance	ILQR control
R_dat10	rc_ilqr2	300g/5v controller performance	ILQR control

B: The Discrete-time State-space Realizations for the Selected Nominal Models

1. The nominal model with 0g payload

$$A = \begin{bmatrix}
1.0003 & 0.0049 & 0.0041 & 0.0018 & 0.0030 & -0.0008 & -0.0014 & -0.0017 & 0.0025 & -0.0034 \\
-0.0010 & 0.9942 & 0.0138 & 0.0231 & 0.0265 & 0.0117 & -0.0327 & -0.0115 & 0.0073 & -0.0247 \\
-0.0001 & -0.0058 & 0.9915 & 0.0115 & -0.0144 & 0.0390 & -0.0263 & 0.0090 & -0.0318 & 0.0105 \\
0.0000 & 0.0014 & 0.0056 & 0.9695 & 0.1777 & -0.0027 & -0.0349 & 0.0146 & -0.0213 & 0.0582 \\
0.0000 & -0.0004 & 0.0004 & -0.1644 & 0.9819 & -0.0919 & 0.0314 & 0.0015 & -0.0169 & 0.0063 \\
0.0000 & -0.0002 & -0.0026 & -0.0101 & 0.0651 & 0.9957 & 0.0704 & -0.0105 & 0.0410 & 0.0073 \\
0.0000 & -0.0014 & -0.0051 & 0.0353 & -0.0075 & -0.0221 & 0.8452 & 0.4478 & 0.0187 & -0.1600 \\
0.0000 & -0.0003 & -0.0014 & -0.0019 & 0.0034 & 0.0128 & -0.4361 & 0.8809 & 0.0883 & -0.0346 \\
0.0000 & -0.0009 & -0.0033 & 0.0229 & 0.0035 & -0.0030 & -0.0940 & -0.1141 & 0.5508 & -0.7785 \\
0.0000 & 0.0000 & 0.0002 & 0.0017 & 0.0002 & 0.0081 & 0.0469 & 0.0063 & 0.7968 & 0.5768
\end{bmatrix}$$

$$B = \begin{bmatrix} 0.0067 & 0.0616 & 0.1334 & -0.1289 & -0.1902 & -0.1357 & 0.2688 & 0.2048 & 0.3271 & -0.7559 \end{bmatrix}^T$$

$$C = \begin{bmatrix}
0.3219 & -0.0742 & 0.0103 & 0.0290 & 0.0066 & -0.0632 & -0.0168 & -0.0146 & -0.0068 & 0.0159 \\
-0.0221 & -0.0536 & 0.2458 & -0.0269 & 0.1161 & -0.1902 & 0.3498 & -0.2938 & 0.2144 & -0.2824 \\
0.0031 & 0.0214 & -0.0504 & 0.0756 & -0.0842 & 0.0084 & 0.0691 & -0.0724 & -0.0382 & -0.0081 \\
0.0023 & 0.0233 & 0.0013 & -0.0112 & -0.0111 & -0.0169 & 0.0218 & 0.0118 & 0.0001 & 0.0072
\end{bmatrix}$$

2. The nominal model with 200g payload

$$A = \begin{bmatrix} 1.0002 & 0.0035 & -0.0022 & 0.0086 & 0.0074 & 0.0002 & -0.0042 & 0.0033 & -0.0132 \\ -0.0007 & 0.9957 & 0.0035 & 0.0337 & 0.0455 & -0.0056 & -0.0385 & 0.0287 & -0.0693 \\ 0.0000 & 0.0015 & 0.9979 & 0.0338 & -0.0004 & 0.0453 & 0.0182 & -0.0276 & -0.0024 \\ -0.0001 & -0.0034 & -0.0070 & 0.9924 & -0.0555 & 0.0680 & -0.0034 & 0.0037 & -0.0076 \\ -0.0001 & -0.0034 & 0.0048 & 0.0069 & 0.9761 & 0.0574 & 0.0768 & -0.0310 & 0.0950 \\ 0.0000 & -0.0008 & -0.0008 & -0.0185 & -0.0391 & 0.9908 & -0.0062 & 0.0316 & -0.1538 \\ 0.0000 & -0.0012 & 0.0022 & -0.0080 & -0.0281 & -0.0179 & 0.8164 & -0.4358 & -0.0851 \\ 0.0000 & 0.0002 & -0.0002 & 0.0012 & 0.0026 & -0.0014 & 0.4752 & 0.8728 & 0.0331 \\ 0.0000 & -0.0006 & 0.0012 & -0.0037 & -0.0117 & -0.0031 & -0.0448 & 0.0284 & 0.9273 \end{bmatrix}$$

$$B = \begin{bmatrix} -0.0015 & 0.0153 & -0.1342 & 0.0651 & -0.1310 & 0.2089 & 0.1045 & -0.5222 & 0.1266 \end{bmatrix}^T$$

$$C = \begin{bmatrix} 0.3592 & -0.1167 & 0.0179 & 0.0239 & -0.0343 & -0.2054 & 0.0006 & 0.0672 & 0.6455 \\ -0.0202 & -0.0698 & -0.2385 & 0.1775 & 0.2325 & -0.0251 & 0.5379 & -0.0655 & -0.3755 \\ 0.0064 & 0.0367 & 0.0631 & -0.0489 & -0.0930 & -0.0616 & 0.1214 & 0.0439 & -0.2822 \\ 0.0023 & 0.0191 & -0.0077 & 0.0074 & -0.0357 & 0.0225 & 0.0581 & -0.0163 & -0.0675 \end{bmatrix}$$

3. The nominal model with 400g payload

$$A = \begin{bmatrix}
1.0003 & 0.0035 & -0.0052 & 0.0137 & 0.0029 & 0.0037 & -0.0023 & 0.0055 & -0.0049 & -0.0029 \\
-0.0006 & 0.9993 & -0.0075 & 0.0477 & 0.0252 & 0.0230 & -0.0174 & 0.0234 & -0.0291 & -0.0277 \\
0.0001 & 0.0026 & 0.9973 & 0.0471 & -0.0309 & -0.0061 & 0.0146 & -0.0065 & 0.0350 & 0.0424 \\
0.0000 & -0.0010 & 0.0008 & 0.9798 & -0.0912 & -0.0205 & -0.0006 & -0.0220 & -0.0001 & -0.1252 \\
0.0000 & -0.0006 & 0.0024 & 0.0368 & 0.9793 & -0.1815 & -0.0369 & -0.0663 & 0.0049 & -0.0071 \\
0.0000 & 0.0005 & -0.0023 & 0.0440 & 0.1221 & 0.8842 & 0.3663 & 0.0641 & 0.1494 & 0.0353 \\
0.0000 & 0.0002 & -0.0010 & 0.0077 & -0.0083 & -0.3277 & 0.9219 & 0.0448 & 0.0201 & -0.0043 \\
0.0000 & 0.0003 & -0.0014 & 0.0225 & 0.0261 & -0.0786 & -0.0930 & 0.9541 & 0.2042 & -0.0359 \\
0.0000 & 0.0002 & -0.0010 & 0.0079 & -0.0035 & -0.0629 & -0.0434 & -0.1625 & 0.9599 & 0.0243 \\
0.0000 & 0.0000 & -0.0001 & 0.0028 & 0.0004 & -0.0034 & -0.0023 & 0.0003 & -0.0056 & 0.9987
\end{bmatrix}$$

$$B = \begin{bmatrix} -0.0077 & -0.0553 & -0.0518 & 0.0413 & -0.3077 & 0.0349 & -0.4077 & -0.1403 & -0.2311 & -0.0119 \end{bmatrix}^T$$

$$C = \begin{bmatrix}
0.3692 & -0.1354 & -0.0295 & 0.0198 & -0.0396 & 0.0236 & 0.0044 & 0.0388 & 0.0390 & 1.2194 \\
-0.0333 & -0.0889 & -0.1454 & 0.2234 & 0.1885 & -0.3314 & -0.1951 & -0.0330 & -0.0900 & -1.8546 \\
0.0097 & 0.0400 & 0.0290 & -0.1357 & -0.0980 & -0.0930 & 0.0140 & 0.2532 & -0.0927 & 1.2120 \\
0.0026 & 0.0161 & -0.0124 & -0.0107 & -0.0266 & -0.0219 & -0.0136 & -0.0414 & 0.0037 & -0.0763
\end{bmatrix}$$